Passive Electromagnetic Damping Device for Motion Control of Building Structures

by

Rogelio Palomera-Arias

M. S. Electrical Engineering
Massachusetts Institute of Technology, 1998

B. S. Electrical Engineering
University of Puerto Rico, 1996

Submitted to the Department of Architecture in
Partial Fulfillment of the Requirements for the Degree of

Doctor of Philosophy in Architecture: Building Technology

at the

Massachusetts Institute of Technology

September 2005

Signature of Author .....
Department of Architecture
August 5, 2005

Certified by .....
John A. Ochsendorf, PhD
Assistant Professor of Building Technology
Thesis Supervisor

Accepted by .....
Yung Ho Chang
Chairman, Department Committee on Graduate Students
Department of Architecture

DISSERTATION COMMITTEE:

John A Ochsendorf, PhD, Assistant Professor of Building Technology (Chair)

Jerome J. Connor, Jr., ScD, Professor of Civil and Environmental Engineering

Gerald L. Wilson, ScD, Vannevar Bush Professor, Professor of Electrical and Mechanical Engineering

Passive Electromagnetic Damping Device for Motion Control of Building Structures

by

Rogelio Palomera-Arias

Submitted to the Department of Architecture on August 5th, 2005
in Partial Fulfillment of the Requirements for the Degree of
Doctor of Philosophy in Architecture: Building Technology

ABSTRACT

The research presented in this thesis develops a new device for the passive control of motion in building structures: an electromagnetic damper. The electromagnetic damper is a self-excited device that provides a reaction force to an applied motion. We chose a tubular permanent-magnet linear machine as this new structural damper, and we derive its mathematical model using quasi-static electromagnetic theory. Computer simulations and experimental characterization of a small-scale prototype electromagnetic damper validated the mathematical model of the device. The behavior of the electromagnetic damper approximates that of an ideal damper.

We conducted a feasibility study for the application of electromagnetic dampers to full-scale buildings. We used two performance measures: the damping density and the damping cost of the device. Comparing the performance of the electromagnetic damper to that of viscous fluid dampers, the maximum damping density of electromagnetic dampers is, at best, equal to that of hydraulic dampers, but with a price at least five times higher. The permanent magnet's current technology and cost are the limiting factors for the electromagnetic damper. However, the electromagnetic damper provides flexibility not available previously to building designers as it can be used as a semi-active damper, as an actuator or as an energy regenerator without physical modifications to the device.

Finally, we developed a design methodology for the electromagnetic damper to achieve a specified damping performance and introduced two techniques for the dynamic response analysis of buildings with electromagnetic dampers: One based on frequency domain approximations and one based on state-space models.

Thesis Supervisor: John A. Ochsendorf, PhD
Title: Assistant Professor of Building Technology

Para Pamen, Coco, Pamela y Netza…

Acknowledgments

I would like to express my gratitude to my family for their love and support, and to all the people at MIT and outside MIT that helped me in this endeavor:

The members of my thesis committee. My thesis advisors, Prof. John A. Ochsendorf for his support and confidence on this project; and Prof. Jerome J. Connor for his support and guidance, and for providing the seed idea for this research. Prof. Gerald L. Wilson for his support and help with the electromagnetic part of it.

Dean Ike Colbert, Associate Dean Blanche Staton and the staff of the Graduate Students Office for their encouragement, financial and moral support, and invaluable help and advice.

Prof. Derek Rowell and course 2 for their financial support by appointing me as "The Lab TA" for 2.010, later renamed 2.14, for so many years. Mike Maier for his support with and lending me equipment.

My colleagues, past and present, in the Building Technology Lab for their support and friendship, especially Christine Walker for listening to my "ideas" and stories, and for her help and insights while working on this and other projects. Harn Wei Kua for his insight and support.

The staff and faculty of Building Technology and the Architecture Department.

The Edgerton Center staff, in particular Fred Cote from the machine shop, Anthony J. Caloggero, and Dr. James W. Bale for their help and equipment while performing some of this thesis experimental work.

Joe Reily at the Wentworth Institute of Technology, and Prof. Lorna Gibson (course 3) at MIT for letting me to use their Instron machines and laboratories to perform some of the experiments.

My friends at MIT, way too many to mention all here, for their encouragement and moral support. And last, but not least, Susan J. Brown for her advice and help reviewing this thesis.

Table of Content

List of Figures

List of Tables

Chapter 1

Introduction

This research creates a new method for damping buildings and structures using electromagnetic devices. We demonstrate that the same equation governing an ideal damper can describe a linear electrical machine force-velocity relationship when this machine operates as a passive damper, effectively developing a new application for electric devices as passive structural dampers

In the following chapters, we derive a mathematical model of the electromagnetic damper, and from that model, we perform a feasibility study of its application to full-scale structures. We also develop the design and analytical tools for working with such electromagnetic dampers in the design phase of a building.

1.1 Framework of Research

Recent trends in structural design favor passive motion control with the introduction of supplemental energy dissipation devices to mitigate the impact of earthquake and wind loads (Soong and Dargush 1997). Energy dissipation in current systems and devices is achieved by either transferring energy between different vibration modes, or by converting the kinetic energy to heat or to inelastic deformations of materials (Housner et al. 1997). The electromagnetic damper is a new device for passive motion control that converts the kinetic energy into electrical energy, rather than solely into heat or material deformations.

Using an electromagnetic damper instead of current structural damping systems provides flexibility not available previously to building designers. The electromagnetic damper is an electric machine, and as such, it can be used as an actuator or a generator. However, visualizing the electromagnetic damper as a passive device simplifies its application in structures since design methods and rules for using manufactured damping are readily available to building and structure designers.

Various strategies exist to control the structural motion and vibrations induced by earthquake and

wind disturbances. These control strategies are classified based on the external energy requirement and type of devices used to counteract the disturbance. Two general types are mainly in use: passive and active control. Passive systems require no external energy to mitigate the effects of disturbances, while active systems use external energy to power actuators that cancel out the dynamic loads. Hybrid systems are also used that combine active and passive strategies, either using the active system to improve the performance of the passive system, or by using the passive system to decrease the energy requirement of the active system (Housner et al. 1997).

In a passive system, motion disturbances are minimized by either modifying the physical and geometrical properties of the structures to reduce their susceptibility to a given disturbance (Housner et al. 1997), or by increasing the energy dissipation capability of the structure; the greater the energy dissipation, the smaller the amplitude of the motion generated by the external excitation. The inherent energy dissipation of the structure is supplemented using materials and devices (structural dampers) that dissipate the kinetic energy imparted into the building by the disturbance. Passive control systems are relatively simple and stable systems that have fixed properties and are designed or tuned for a particular disturbance. Once installed, a typical passive system cannot be adjusted to compensate for a change in the nature of the disturbance (Connor 2003). In recent years however, semi-active devices have been proposed to allow adaptive passive control of structural motion. Semi-active devices are passive devices, whose parameters can be actively changed, with minimal energy input, to adapt to changes in the nature of the disturbance (Jalili 2002 171).

Active strategies, in the other hand, involve the use of sensors and actuators. Sensors monitor the state of the structure and the nature of the excitation, while actuators provide the necessary forces to cancel out the dynamic loads (Connor 2003). These systems might provide better, and broader, disturbance rejection than passive systems; however, they are complex and expensive systems highly vulnerable to power failures, which could occur during a seismic event or strong winds. Also, their performance is highly dependent on the control algorithms used and are susceptible to control-induced instability (Housner et al. 1997). Full scale applications of structural active control systems have been limited mostly to civil structures in Japan, largely due to implementation issues, such as the uncertainty in the modeling of both the physical properties of the structures and the disturbances such as earthquakes and wind (Soong 1996).

1.2 Research Contributions

The first contribution of this research is the development of a new type of structural passive damper for buildings. We develop a mathematical model based on quasi-static electromagnetic theory, and demonstrate that the force-velocity relation of the electromagnetic damper is similar to that of an idealized damper. The damping coefficient of the electromagnetic damper is described in terms of the geometric, magnetic and electric properties of the device. The electromagnetic damper model is validated experimentally using a small-scale prototype.

The second contribution is a feasibility study of the electromagnetic damper in full-scale buildings. Two performance measures, damping cost and damping density, are used to asses the practicality of electromagnetic dampers. Based on these performance measures, the device is compared to viscous fluid dampers and the practical limitations of the damper are discussed.

The third contribution of this work is the development of a design methodology for electromagnetic dampers. The dimensions and physical parameters of the damper are obtained from the required building damping performance and available space.

As a fourth contribution, this work introduces techniques for the dynamic response analysis of structures with electromagnetic dampers. These techniques follow two approaches to incorporate the damper model into the structure model, and presume that the structure is modeled as a lumped-mass system. The first approach is a frequency domain characterization of the electromagnetic damper that allows its incorporation as an ideal damper in traditional modal analysis methods. The second approach is based on a state-space representation of multiple degree-of-freedom structures, and facilitates transient analysis incorporating the non-ideal characteristics of the electromagnetic damper.

Finally, this work provides an initial basis for further research in the field of electromagnetic dampers applied to buildings and the control of structural motion. To the author's best knowledge, this is the first study in which these devices are systematically analyzed and their practical viability to the application of buildings and civil structures investigated.

1.3 Organization

Chapter 2 presents a literature review of previous work where electrical machines are proposed as dampers, in both structures and other engineering domains. Chapter 3 chooses the machine type for the electromagnetic damper and derives its mathematical model based on quasi-static electromagnetic theory. Chapter 4 presents the feasibility study of the structural electromagnetic damper. Chapter 5 develops the design methodology for the electromagnetic damper, and Chapter 6 presents the mathematical methods to analyze the dynamic response of building structures incorporating electromagnetic dampers. Chapter 7 presents the experimental characterization of a scale model electromagnetic damper. The chapter gives the descriptions of the experiments and their corresponding mathematical models, follower by the results and discussion of the results from computer simulation and the physical experiments. Finally, Chapter 8 presents the conclusions and future work recommendations.

Chapter 2
Electromagnetic Damping Literature Review

2.1 Introduction

Electromagnetic (electromechanical) devices, other than eddy current dampers, have been used and studied mainly as either force actuators or generators of electrical energy. Their study as passive dampers has been limited to educational systems (Podrzaj et al. 2005) or to regenerative braking or regenerative damping systems. The term "regenerative damper" (Fodor and Redfield 1992) refers to devices that extract usable energy while providing considerable damping, similar to regenerative braking that extracts usable energy from the braking process.

Regenerative dampers are typically (force) actuators in a control system serving a dual purpose depending on their operational state: they counteract the disturbance using energy from an energy source or energy storage device, or they transfer energy from the disturbance to an energy storage device. Regenerative damping has been studied mostly for vehicle applications, but some studies have been made of their possible application to civil structures (Nagem et al. 1995; Nerves 1996; Scruggs 1999; Sodano and Bae 2004).

2.2 Electromagnetic Damping in Structures

Electromechanical machines in civil structures have traditionally been used as force actuators. Recently, electric machines have been proposed as regenerative devices in order to reduce the energy requirement of the active control system used to mitigate the effects of disturbances such as wind and earthquake. A review of these proposals is presented in the following paragraphs.

Studies of structural eddy current dampers are limited to small scale structures, such as beams and thin membranes (Sodano and Bae 2004). Eddy current dampers are electromagnetic devices that dissipate energy as heat on a conductor moving inside a magnetic field. Eddy current damping has not been applied to large scale civil structure, and is used primary as a braking mechanism in magnetic levitation applications and high-speed vehicles (Jang and Lee 2003)

Henry and Abdullah (2002) and Jang (2002) proposed a structural electromagnetic damper similar to a mechanical tuned mass damper (TMD). In this device, permanent magnets are attached to a big moving mass, while coils attached to the building structure move inside the magnetic flux created by the magnets, inducing the damping force.

Nagem (1995) proposed an electromechanical vibration absorber as a way of avoiding the large amplitude mechanical oscillations of conventional mechanical vibration absorbers. In the proposed realization, he replaced the secondary mechanical oscillator in the absorber by an electromechanical transducer (voice-coil) and a resonant electrical circuit (Series RLC circuit). The system was tested experimentally using a model vibrating cantilever beam and was shown to dramatically reduce the vibration amplitude near the beam resonance frequency.

Nerves (1996; Nerves and Krishnan 1996) studied the feasibility of using electric actuators as regenerative devices to provide active control of civil structures. He proposed a rotational brushless DC machine as a regenerative actuator coupled to a hybrid mass damper attached to the structure. The system behavior was simulated in a single-degree-of-freedom structure, a fixed-base multistory structure and a base-isolated multistory structure. The simulations were performed using various active control strategies and showed that the use of regenerative electric actuators reduces the power and energy requirements of the control system, making it a viable alternative for active control. The simulated energy reduction varied from approximately 20% to 70% depending on the control method and disturbance signal, with sliding-mode control often showing the lowest power and energy requirements.

Scruggs (1999) analyzed the use of proof-mass actuator as a regenerative actuator for mitigation of earthquake disturbances in civil structures. He stated that with the proper control system design, it is possible to mitigate a disturbance using mostly energy extracted from it. A performance measure of the energy capacity required of the electric power source to implement closed-loop control of the structure was also developed.

Vujic (2002) studied feedback control strategies that would improve the energy efficiency of an active isolation system by providing electrical energy regeneration. To model the isolation system, he used piezoelectric stack and linear electromagnetic (voice-coil) actuators. Energy regeneration was approached as a closed-loop control problem, which was then solved to optimize

regeneration.

2.3 Regenerative Electromagnetic Damping

Fodor and Redfield (1992) studied regenerative damping in the context of vehicle suspension systems. A lever with a movable fulcrum, called the Variable Linear Transmission, was proposed as the mechanical device to transfer vibration energy from the wheels to an energy storage device, in this particular case a hydro-pneumatic accumulator. Simulations of the system using the quarter car model showed that the operation of the regenerative damper closely approximates the operation of a passive viscous damper.

Beard (1993) presented the concept of regenerative isolation as a way to provide active vibration control without its external energy requirements. In a regenerative isolation system (RIS), the energy from dissipative portions of the control cycle is stored rather than dissipated, and used to complete the active portions of the control cycle. The general system proposed by Beard consists of three fundamental components: an actuator to absorb and deliver energy to the controlled system, an energy-storing device, and a power management device to direct the flow of energy from and to the actuator and storage device. He also suggests that "the designer of a vibratory isolator should consider a RIS after passive and semi-active methods have failed, and before considering active approaches." The regenerative isolation system was studied and simulated using a hydraulic realization of the regenerative system. However, experimental verification was performed using an electrical system analogous (same bond graph) to the studied hydraulic system. Since the regenerative system was proposed as an alternative to active control, the author ties the usefulness of the regenerative system to its tracking behavior and control power requirements.

Jolly (1993; Jolly and Margolis 1997) explored the diagnosis, design and utility of power conserving subsystems, that is, subsystems that are either passive or regenerative. A mathematical analysis of multi-node linear time invariant (LTI) subsystems imbedded within a host LTI system using impedance matrices was performed. Tools for computing bounds on the average power absorption by the subsystem assuming lossless regeneration were presented. An example was developed in his thesis for the control of wind response of multi-story structures from a

mathematical point of view. Jolly also showed that the average power absorption of a subsystem is essentially the maximum surplus power available for accumulation by the subsystem assuming ideal regeneration. Ideal regeneration could be approximated by constructing the subsystem using energy storage components and force actuators that utilize a pulse-width modulation type of control.

Practical implementations of regenerative subsystems were investigated by Jolly and Margolis (1997). Regenerative force actuators were studied in practical applications of base-excited systems and compound mount systems. Simulation results of the base-excited suspension systems exhibit positive average energy absorption regardless of the nature of the excitation, while the compound-mount application energy absorption was dependent upon the nature of the input spectrum. Furthermore, experimental results of the suspension system showed that the device could create forces under conditions that passive and semi-active systems cannot.

Okada and Harada (Okada and Harada 1995; Okada and Harada 1996; Okada et al. 1996) proposed the use of an electro-dynamic actuator as a regenerative damper. A linear DC motor was used as the regenerative actuator, and two batteries, connected to form a bipolar power supply, were used as the energy storage element in the system. During high-speed motion, the motor voltage is greater than the battery voltage and the system generates electric power, which is stored in the batteries. During low speed motion, the voltage generated at the motor is smaller than the battery voltage and the system was operated either as a passive damper, where the power was dissipated by resistor; or as an active damper, where the motor operates as the force actuator in closed loop control system. The authors also proposed the use of the system as a regenerative vehicle suspension system with active control used during low speed motion. The system was simulated and tested experimentally on a single degree-of-freedom system, using the mass of the motor stator as the system mass. Experimental and simulation results showed a regeneration ratio of up to 25% around the resonant frequency when regenerative and passive damping was used.

Okada et al. (1998) presented the application of an electro-dynamic actuator for the regenerative control of a moving mass vibration damper. The actuator was installed between the main mass and the auxiliary mass. The mass, stiffness and damping coefficients of the auxiliary system

were designed using the Den Hartog optimum tuning condition. Simulation results showed that the regenerated energy was bigger when the equivalent-damping coefficient of the actuator is smaller than the optimal damping ratio. Simulation and experimental results also showed that energy was regenerated when big excitation was applied and damping was added to the system. No energy was regenerated for small excitations.

Suda, Nakano et al. (Suda et al. 1998; Nakano et al. 1999; Nakano et al. 2000) proposed a method of vibration control using separate actuator and regenerative damping devices. In this scheme, the electric energy regenerated in a primary system is stored in a capacitor and then used by the actuator to control vibrations in a secondary system. The method was applied to the active vibration control of a truck's cab. The energy used for the active control of the cab suspension of a truck was obtained from another subsystem in the truck, the chassis suspension. A generator was installed in the chassis suspension to provide damping and regenerate vibration energy. The regenerated energy was stored in a condenser to be utilized by the cab suspension actuator. The simulations showed that the self-powered active cab suspension had better isolation performance than the one achieved by semi-active and passive isolation systems alone.

Graves (2000) also studied energy regeneration in vehicle suspension using electromagnetic devices. He proposed a generalized electromagnetic topology to assist in the design of optimized regenerative dampers. Linear and rotational damping devices as well as the electric and magnetic circuits of regeneration devices were studied and compared. He found that both rotational and linear devices were suitable to as regenerative devices. Rotational devices were better suited to provide mechanical amplification of damping and regeneration was easier to achieve using rotational devices, but with a negative effect on vehicle high frequency dynamics.

Kim (2002) improved the damping capability and efficiency of the electro-dynamic regenerative damper presented by Okada et al. by introducing a pulse-width modulated step-up chopper circuit between the actuator and charging circuit. This circuit improved the low frequency (low speed) regenerative capabilities of the device by decreasing the regeneration dead zone caused when the generated voltage is lower than storing device potential. The proposed damper was applied to an active mass damper system, and validated experimentally using a moving coil linear motor and springs.

2.4 Electromagnetic Damper Modeling

Analysis of electric machines as dampers is limited to simplified equations relating the damping coefficient to the machine constants and the circuit resistance when the damper is connected to a energy storage capacitor (Okada and Harada 1995; Podrzaj et al. 2005). This description makes no attempt to describe the damping coefficient in terms of the physical parameters of the machine, such as size and magnetic properties. Detailed analyses of linear machines presented previously in the literature are tailored to the machine operating either as a motor or as a generator. Therefore, the goal of the majority of the analyses was to calculate the output (maximum and average) of the machine, namely the thrust force for motors, and electrical power output and efficiency for generators, not the equivalent damping coefficient that will result when the machine operates as a damper.

Various analytical methods have been pursued in the literature to analyze tubular linear permanent magnet machines. Analytical methods provide insight into the relationship between design parameters and the machine performance that is not normally gained using more accurate numerical techniques (Wang et al. 2001), such as finite element or finite difference methods. The first analytical studies generalized rotational machine equations to linear machines (Boldea and Nasar 1987; Boldea and Nasar 1987; Deng et al. 1987) and assumed sinusoidal excitation as well as sinusoidal distribution of the magnetic fields. More recent analyses have been based on different approaches to solve Maxwell's equations.

Analyses based on magnetic vector potentials have been performed and found to be in good agreement with finite element analyses. However, the field solutions in cylindrical machines involve Bessel functions and the solution of multiple linear equations to determine the coefficients of the solution functions (Zagirnyak and Nasar 1985; Kim et al. 1996; Wang et al. 1999; Wang et al. 2001; Amara et al. 2004).

Another approach has used integral equations methods to convert the device components into equivalent electrical networks. These methods have been shown to be well suited to moving conductor devices and the modeling of electromechanical devices coupled to external electric circuits, but have the disadvantage of being characterized by full matrices that might require extensive computations (Barmada et al. 2000). The complexity of these equations takes away the

practical insight that would be expected from an analytical model.

Finally, lumped parameter magnetic network (magnetic circuit) methods have also been used to model tubular machines. These methods are based on the magneto-static field equations and provide simplified equations that show the dependence of the machine performance on the main geometrical parameters, under the limitations stemming from modeling idealized machines. In order to account for non-ideal aspects of the modeled machines, parameter derived from experimentation or numerical calculations are introduced into the model equations (Coutel et al. 1999; Bianchi et al. 2001; Canova et al. 2001)

2.5 Summary

Electromagnetic machines used for motion control purposes are mostly used as actuators or as regenerative devices, the most common being the braking systems used in electric vehicles. When the regenerative device is not used in a braking system, it is used as a dual purpose device that provides actuation and reduces the external power requirement of the active control system.

The majority of regenerative dampers proposed in the literature are for vehicle applications. Current literature shows that regenerative damping systems have been simulated and experimentally validated using small scale systems. Application of regenerative dampers to structures is currently limited to theoretical studies, numerical simulations, and small scale models. No large scale experiments or tests have been conducted.

While each of the studies proposed new possibilities for regenerative damping, researchers have not focused on the application of electromechanical machines as passive structural dampers, which is the primary contribution of the current work.

Chapter 3
Electromagnetic Damper Modeling

3.1 Introduction

This research develops a new kind of structural damper, the passive electromagnetic damper. A passive electromagnetic damper is an electromechanical device that provides an opposing force to the imparted movement without requiring external electrical energy, unlike typical electric machines operating as motors or actuators. Similar to an electric generator, the electromagnetic damper converts kinetic energy into electric energy. However, there is an important difference: the purpose of the damper is to reduce significantly, if not completely, the motion of the mover, while the purpose of the generator is to provide electrical energy to the devices in the electric circuit to which the generator is connected without detaining the mover.

This chapter presents the analysis of the electromagnetic damper as a discrete device. Sections §3.2 and §3.3 provide the background for this analysis. The first section introduces the topology of the machine and the selection of a linear tubular permanent-magnet machine as the electromagnetic damper, while the later section introduces the quasi-static electromagnetic theory used to develop the mathematical model in section §3.4. In this latter section we also show that the force-velocity relationship of the tubular electromagnetic damper is similar to that of an ideal mechanical damper where the force F_d is directly proportional to the applied velocity v

$$F_d = c_d v \tag{3.1}$$

where c_d, the damping coefficient, will be determined by the geometric, magnetic and electric properties of the device, and is characterized by the electric machine constant and the impedance of the electric circuit connected to the device. Finally, section §3.5 examines the behavior of the electromagnetic damper using this mathematical model.

3.2 Electromagnetic Damper Machine Topology

Electric machines are classified in two main groups based on the type of motion provided by the mover: rotational motion machines and linear motion machines. The underlying principles are the same for both groups; they differ only in the construction and operation details. The type of motions encountered in a structure, namely lateral deflections and inter-story drifts, are linear in nature. Therefore, we have chosen a linear motion machine for the electromagnetic structural damper. The use of a linear machine simplifies the mechanical interface between the damper and the structure since it requires no mechanisms to convert the linear motion of the structure into rotational motion, as would be the case with a more common rotational machine.

3.2.1 Linear Machine Types

There are two main components in a linear machine: a moving element known as the *mover* or *translator*, and a static element known as the *stator* or *armature*. Various geometric arrangements are available for linear electric machines, the two basic ones being the planar and the tubular configurations. The two geometric configurations are shown in Figure 3.1. A short internal mover is shown for the tubular machine, but external movers can also be used. The movers can also be longer than the stator (Bianchi et al. 2003).

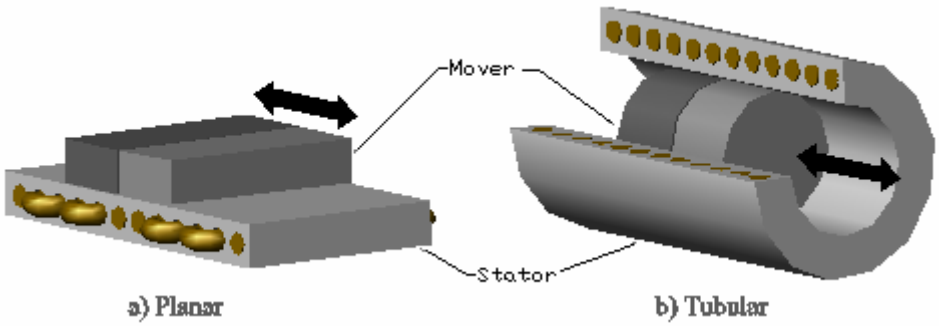

Figure 3.1 Basic Geometric Arrangements of Linear Electric Machines.

For a structural damper application, a short mover tubular arrangement is favored over a planar one because the former is mechanically more rugged, since all the components are enclosed inside a piston-like structure. Also, stray magnetic fields and parasitic forces normal to the direction of travel of the mover are minimized, if not eliminated, in tubular arrangements due to the longitudinal axial symmetry of the device. Finally, for similar sizes and weights, the force den-

sity attainable by the tubular machines is greater than that of planar machines (Eastham et al. 1990; van Zyl et al. 1999).

Direct (dc) and alternating current (ac) machines are available. However, the ac ones are the appropriate type of electric machine for structural damping applications due to the oscillatory nature (back-and-forth movements) of structural motion. Linear ac machines are classified based on how the energy conversion process takes place: synchronous, induction, and permanent magnet machines (Boldea and Nasar 1997). In the following paragraphs, the different types are presented briefly, and their suitability as passive dampers discussed.

The synchronous machine

In a synchronous machine, the energy conversion process occurs at a single fixed speed, the synchronous speed (DelToro 1990). The working magnetic field needed to transfer the kinetic energy into electric energy as the translator is driven at the synchronous speed is typically produced by field windings in the translator powered by dc current. Permanent magnets can substitute the field windings. When using magnets, the machine will also induce current asynchronously in the armature, much like an induction machine. A synchronous machine is not convenient for structural damping application because building movement is never at a constant speed (especially under earthquake excitation!).

The induction machine

The induction machine, similar to most synchronous machines, has windings in both the mover and the stator. However, the mover windings are short-circuited and not connected to a voltage external source as in the synchronous generator. The induction generator can only operate in parallel with an electric power system or independently with a load supplemented with capacitors (Beaty and Kirtley 1998). To generate a moving magnetic field, the armature winding needs an excitation ac current. This excitation current induces a working emf in the translator winding by transformer action. When this excitation current is initially applied, the generator operates as a motor at a speed lower than the synchronous speed of the machine. If the mover is forced to travel at a speed higher than the synchronous speed, power is transferred from the mover to the stator and converted into electrical energy (DelToro 1990).

The permanent magnet machine

In a permanent magnet machine, the working magnetic field is created using permanent magnets mounted on either the translator or the stator of the generator. The magnetic flux is changed by varying the magnetic field across the coils, by changing the magnetic permeability of the flux path for the magnetic field, or by moving the magnet relative to the coil.

From the different types of linear machines presented, a tubular permanent magnet device is favored as an electromagnetic damper for building structures. Both the synchronous and induction machines need some sort of external excitation to convert the kinetic energy imposed to the mover into electrical energy, whether the permanent magnet machines are self-excited. This is particularly important for our purposes, given the intended applications of the machine: to mitigate the effects of wind and earthquakes on buildings.

3.2.2 Machine Topology

There are three general configurations of permanent magnet machines, as depicted in Figure 3.2: (a) moving coil, (b) moving iron, and (c) moving magnet. Though Figure 3.2 shows short internal mover tubular machines, the configurations are operational and independent of the machine geometric arrangement.

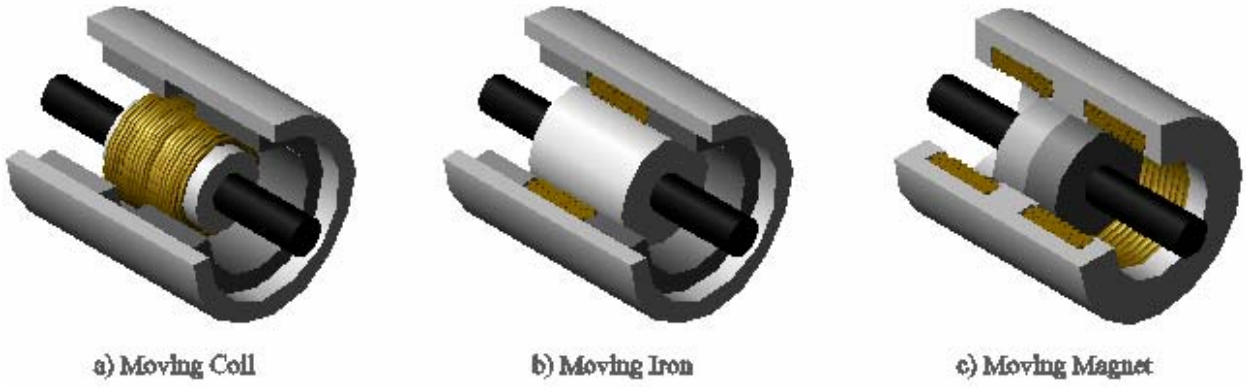

Figure 3.2 Permanent-Magnet Linear Machine Configurations.

In the moving coil configuration, the magnets are stationary in the armatures and the coils are placed on the mover, similar to a typical loudspeaker. Brushes or flexible coils are needed in order to extract the electric energy induced in the coils as they move through the magnetic field.

The moving iron configuration has both the coils and magnets placed in the armature. Moving an iron piece changes the magnetic flux linkage by changing the permeability of the space in the magnetic field. This configuration is rugged and easy to fabricate, but has a higher mover mass than the other two configurations presented. Also, the attainable force per unit volume is lower than that of the moving coil or magnet machines (Arshad et al. 2002).

The last configuration is the moving magnet machine. In this configuration, the mover contains the permanent magnets while the armature houses the coils. Its operation is similar to that of the moving coil but with the roles of the stator and mover reversed. No electrical connection to the mover is required. As a structural damper, the moving magnet configuration seems the more suitable of the three configurations presented in Figure 3.2. The stator of the electromagnetic damper contains the windings, which are cylindrical coils, while the translator contains the machine's permanent magnets.

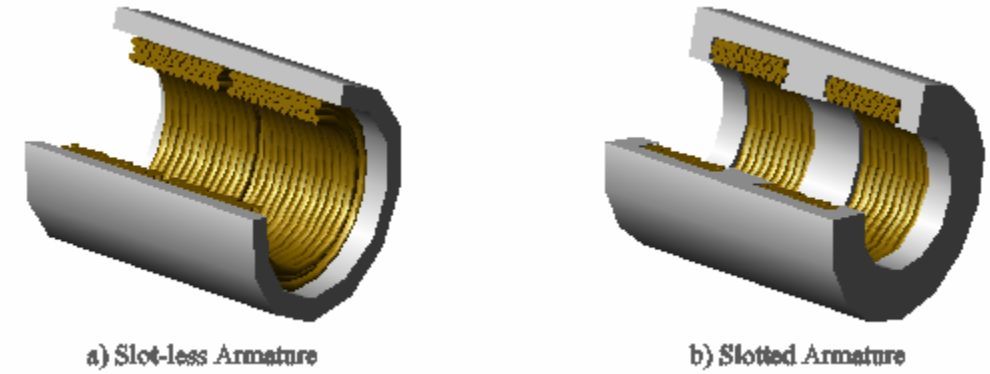

Figure 3.3 Tubular Machine Slot-less and Slotted Stator Illustrations

The armature can be slot-less or slotted, as illustrated in Figure 3.3. Slotted armatures usually have higher force density than slot-less ones, but may present tooth ripple cogging force (Wang et al. 1999) as well as a variation of the coil inductance as a function of the relative position of the armature and the mover (Wang and Howe 2004).

The translator typically has permanent magnets with axial or radial magnetization (Figure 3.4). The radial magnetization uses ring magnets polarized in the radial direction or slightly curved surface mounted rectangular magnets with no pole shoes.

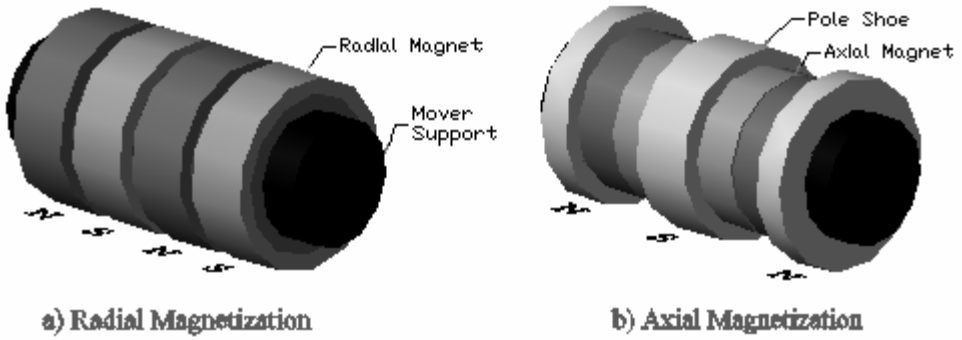

Figure 3.4 Tubular Machine Mover Permanent Magnets Configurations.

Axial magnetization uses cylindrical magnets polarized lengthwise, which are placed between ferromagnetic cylindrical pole shoes that are used to guide the magnetic flux over the air gap into the stator. In both cases, the magnets are placed on the mover support in such a way to make the magnetic polarities on the surface of the mover alternate in the axial direction. It has been shown (Wang et al. 2001) that both magnetization schemes result in similar machine performance. In this project, an axial magnetization machine is used as the electromagnetic damper prototype.

Table 3.1 summarizes the selections for the machine that becomes the electromagnetic damper, and that is analyzed and modeled in this research.

Table 3.1 Electromagnetic Damper Configuration

Machine Type	Linear Displacement
Working Field	Permanent Magnet
Configuration	Short Internal Mover
Geometry	Tubular
Stator Type	Slot-less
Mover Type	Axial Magnet

3.3 Electromagnetic Theory Background

The mathematical description of any electromechanical system can be divided in two parts: a set of electrically based equations generalized to include the effects of electromechanical coupling, and a set of mechanical based equations, which include forces of electromechanical origin. The electrical equations are based on electromagnetic theory and Maxwell's equations, while the mechanical equations are based on Newton's laws (Woodson and Melcher 1968).

The electromagnetic damper is a quasi-static magnetic field system and therefore is governed by quasi-static electromagnetic theory. The relevant equations used while deriving the damper mathematical model are presented in the following paragraphs.

Lorentz's law quantifies the force $\vec{F}$ experienced by a current i moving at a given velocity in the presence of a magnetic field $\vec{B}$. When the current moves along a direction $\vec{l}$ the Lorentz's equation is

$$\vec{F} = \oint i d\vec{l} \times \vec{B} \tag{3.2}$$

Ampère's Law states that the line integral of a magnetic field intensity $\vec{H}$ around a closed contour *C* equals the net current ($\vec{J}$ being a current density) passing through the surface *S* enclosed by said contour (Haus and Melcher 1989). Under quasi-static conditions, the integral form of Ampère's law is

$$\oint_C \vec{H} \cdot d\vec{l} = \int_S \vec{J} \cdot d\vec{s} \tag{3.3}$$

Faraday's Law states that electric fields $\vec{E}$ can be generated by time-varying magnetic fields $\vec{B}$ (Woodson and Melcher 1968). The derivation of the damper equation uses the integral form of this relationship

$$\oint_C \vec{E} \cdot d\vec{l} = -\int_S \frac{\partial \vec{B}}{\partial t} \cdot d\vec{s} \tag{3.4}$$

In both Ampère's law and Faraday's law equations, the surface *S* is enclosed by the contour *C,* with vector $d\vec{l}$ parallel to the contour and the vector $d\vec{s}$ perpendicular to the surface.

Moreover, the magnetic flux continuity condition has to be satisfied. This condition states that there is no net magnetic flux emanating from a given space. Mathematically, this is expressed as

$$\oint_S \vec{B} \cdot d\vec{s} = 0 \tag{3.5}$$

where the vector $d\vec{s}$ is perpendicular to the surface *S* enclosing an arbitrary volume *V*.

Finally, two constitutive relations are required to fully describe quasi-static magnetic systems: an electrical and magnetic relation. The electric relation is Ohm's law which relates the induced free current density $\vec{J}$ in a material to the applied electric field $\vec{E}$ and the electric conductivity σ of the material

$$\vec{J} = \sigma\vec{E} \tag{3.6}$$

The magnetic constituent relation between the flux density $\vec{B}$ and the magnetic field intensity $\vec{H}$ is commonly expressed as,

$$\vec{B} = \mu_0(\vec{H} + \vec{M}) \tag{3.7}$$

where $\mu_0 = 4\pi \times 10^{-7}$ H/m is the permeability of free space and $\vec{M}$ is the magnetization density that accounts for the effects of magnetizable materials. Normally the magnetization density is proportional to the field intensity, and the magnetic constituent relation can be written as

$$\vec{B} = \mu\vec{H} \tag{3.8}$$

where μ is the permeability of the material.

For non-magnetic materials, $\mu = \mu_0$ for all practical purposes, while for soft ferromagnetic materials, the permeability is approximated by $\mu = \mu_0\mu_r$,where μ_r is the relative permeability of the material (El-Hawary 2002) and is typically much greater than unity. For hard ferromagnetic materials (permanent magnets) the permeability is not constant, but is a function of the magnetic field intensity $\vec{H}$.

The permanent magnet relationship between the flux density and the field intensity is typically represented by a hysteresis loop like the one shown in Figure 3.5. The first quadrant represents the initial magnetization of the magnet, while the second quadrant, known as the demagnetization curve of the magnet, represents the region in which the magnet typically operates. That is, it is the region where the magnet performs work against an applied reverse field.

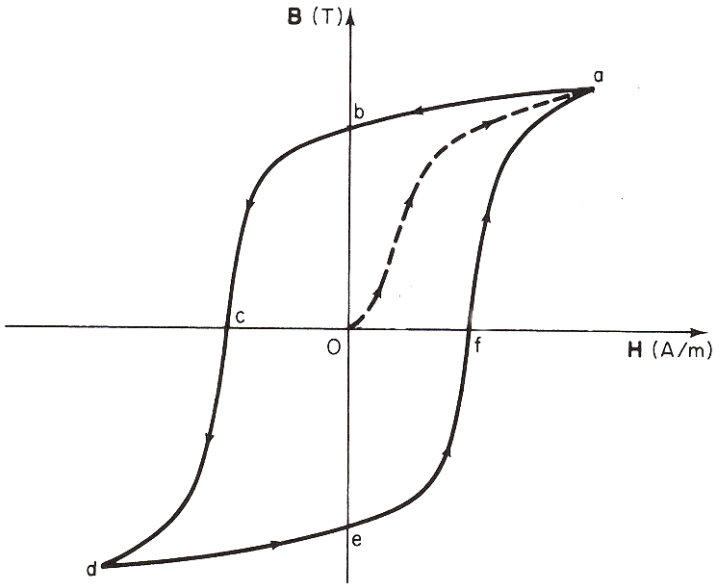

Figure 3.5 Typical B-H Hysteresis Loop for Permanent Magnet Materials.

Two points in the demagnetization curve are of interest when characterizing the performance of a magnet: the remanence or residual flux density B_{rem} (point b); and the coercivity force H_c (point c). To simplify analytical estimations, a straight line passing through those two points usually approximates the demagnetization curve

$$B_m = B_{rem} + \mu_{rec} H_m \tag{3.9}$$

where $\mu_{rec} = B_{rem} / H_c$ is known as the recoil permeability.

The point (H_m, B_m) of values of field intensity H_m and flux density B_m at which a magnet is biased when used as a source of magnetic flux is known as the operating point of the magnet. This point moves along the demagnetization curve and is usually not known a priori, and is determined by the system in which the magnet operates. The system is described by a load line, an equation that relates the magnet's field intensity to its flux density in terms of the material and geometric properties of the system. The intersection of the load line and the demagnetization curve locates the operating point of the magnet.

3.4 Electromagnetic Damper Model Derivation

The mathematical model derived in this section quantifies the damping coefficient of the electromagnetic damper given the geometric, magnetic and electric characteristics of the device. The electromagnetic equations presented previously are applied to a linear moving magnet tubular machine like the one shown in Figure 3.6 in order to derive its analytical model. This machine is similar in construction to the scale prototype used for the experimental characterization of the device (Chapter 6 and 7) and has the following characteristics:

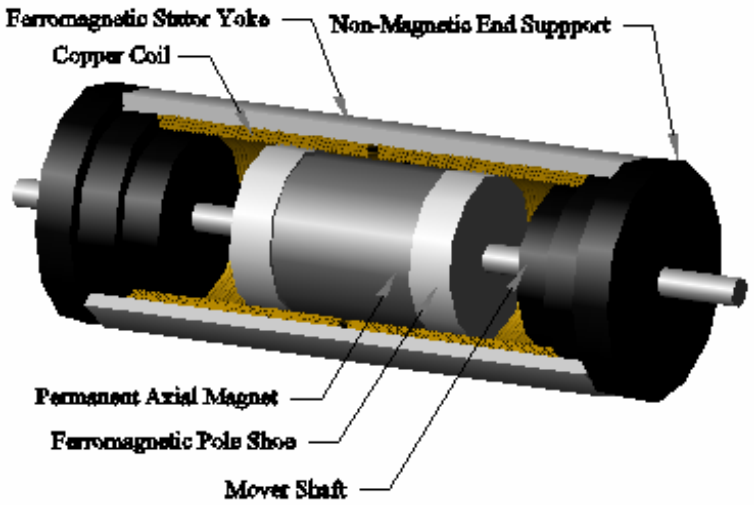

Figure 3.6 The Prototype Electromagnetic Damper.

1. It has a short translator moving inside the stator.
2. The translator has a single cylindrical permanent magnet with axial magnetization. The magnet is located between two ferromagnetic pole shoes.
3. The armature is slot-less with a single phase winding over its length. The winding is made of two coils wound in opposite directions and connected in series.
4. The end supports are made of non-magnetic material.
5. The length of each coil equals the length of the translator.
6. The length of the magnet equals the stroke of the machine, and is smaller than the translator length.

The analysis performed in this section is different to previous studies in that it describes the electric machine when used as a passive damper. The purpose of this analysis is to express the ma-

chine reaction force to an applied velocity. Analyses of linear machines presented previously in the literature are tailored to machines operating either as motors or as generators. Therefore, their goal is to calculate the output (maximum and average) of the machine, namely the thrust force for motors, and electrical power output for generators.

Table 3.2 Electromagnetic Damper Parameters.

Name	Symbol	Description
Pole pitch	τ_p	It's the distance between changes in polarity. The distance between adjacent pole shoes or radial magnets.
Magnet Length	τ_m	The actual length of the magnets. It is smaller or equal than the pole pitch.
Pole Shoe Width	τ_f	The width of the pole shoes. $\tau_f = \tau_p - \tau_m$
Air gap thickness	g	The distance between the mover and the armature windings.
Number of poles	p	Even number of poles in the machine. Also, number of coils per phase.
Coil height	h_w	Height of the coils in the armature or depth of armature slots.
Coil width	τ_w	Width of each coil in the armature.
Winding pitch	τ_{wp}	The distance between coils on the same electrical phase.
Wire radius	r_w	Radius of the coil wire.
Coil turns	N_w	Number of turns on each coil.
Active coil turns	N_a	Number of turns on each coil intercepted by the pole shoe flux.
Mover radius	r_m	Radius to the outside surface of the magnets or the pole pieces.
Armature radius	r_i	Radius to the inside surface of the armature.
Stator yoke radius	r_s	Radius to the inside surface of the stator yoke or ferromagnetic shell.
Machine radius	r_e	Radius to the outer surface of the motor (armature shell or stator yoke)
Yoke thickness	h_y	The thickness of the armature shell.

A half-section (not to scale) of the device is presented in Figure 3.7. This figure shows the dimensions and integration paths used in the analysis presented below. Table 3.2 describes the geometric parameters of the damper including two coil parameters that not shown in the picture.

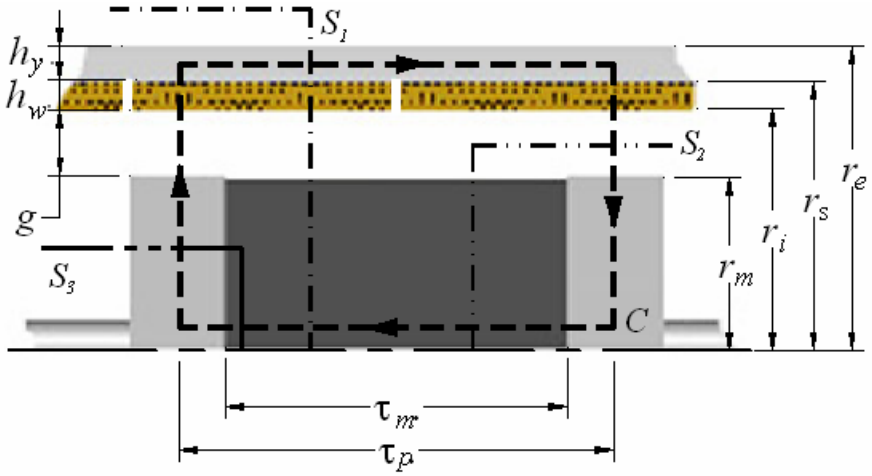

Figure 3.7 Damper Half-Section Diagram showing Dimensions and Analysis Integration Paths.

3.4.1 Permanent Magnet Operating Point

Applying Ampère's law equation to the contour *C* shown in Figure 3.7 gives

$$\oint_C \vec{H} \cdot d\vec{l} = \int_{Magnet} \vec{H}_m \cdot d\vec{l} + 2\int_{Poles} \vec{H}_p \cdot d\vec{l} + 2\int_{Gap} \vec{H}_g \cdot d\vec{l} + 2\int_{Coil} \vec{H}_c \cdot d\vec{l} + \int_{Shell} \vec{H}_s \cdot d\vec{l} = 0 \qquad (3.10)$$

The above equation is solved under the following assumptions:

1. The magnetic field $\vec{H}$ is parallel to $d\vec{l}$, which follows the direction of contour *C*.
2. The magnetic field in the air gap is purely radial.
3. The permeability of copper is similar to that of air; therefore the effective air gap is the thickness of both the actual air-gap and coil.
4. A radial field approximates the magnetic field in the pole shoes.
5. The magnetic field in the stator yoke (shell) and the magnet are purely axial.
6. Magnetic leakages in the system are neglected.
7. There is not magnetic saturation in the materials. The magnetic field and the magnetic flux density outside the magnet are related by $H = B/\mu_0\mu_r$.

Based on the above assumptions, equation (3.10) can be written as

$$\oint_C \vec{H} \cdot d\vec{l} = H_m \tau_m + 2\int_0^{r_m} \frac{B_p}{\mu_0 \mu_{Fe}} dr + 2\int_{r_m}^{r_s} \frac{B_g}{\mu_0} dr + \frac{B_s}{\mu_0 \mu_{Fe}} \tau_p = 0 \qquad (3.11)$$

where μ_0 is the permeability of free space and μ_{Fe} is the relative permeability of iron (or steel) used for the stator shell and pole shoes.

When the various magnetic flux densities in the machine are expressed in terms of the magnet's flux density B_m, the above equation becomes the machine load line, which determines the permanent magnet operation point.

The magnetic flux density B_s in the stator yoke is determined by applying the continuity condition to an enclosing surface S_1 that intercepts the yoke and the magnet, creating the cross sectional areas A_s and A_m perpendicular to fields B_s and B_m, respectively.

$$\oint_{S_1} \vec{B} \cdot d\vec{s} = B_m A_m - B_s A_s = 0 \Rightarrow B_s = \frac{B_m A_m}{A_s} = \frac{r_m^2 B_m}{h_y (r_s + r_e)} \tag{3.12}$$

Similarly, the air-gap flux density is found using the cylindrical surface S_2 of radius r partially enclosing the magnet. This surface intercepts the magnet and gap fields perpendicularly; therefore the gap flux density is given by

$$B_g = \frac{B_m A_m}{A_g} = \frac{r_m^2 B_m}{2\tau_f r},\ r_m \le r \le r_s \tag{3.13}$$

Finally, using the cylindrical surface S_3, which creates intercept surfaces A_p and A_m that vary with the radius r of S_3, the pole shoes flux density is found as

$$B_p = \frac{B_m A_m}{A_p} = \frac{\pi r^2 B_m}{2\pi r \tau_f} = \frac{r B_m}{2\tau_f},\ 0 \le r \le r_m \tag{3.14}$$

Substituting the results from (3.12) thru (3.14) into (3.11) yields the following load line,

$$H_m = -\frac{r_m^2 B_m}{\mu_0 \tau_f \tau_m} \left(\ln\left(\frac{r_s}{r_m}\right) + \frac{1}{2\mu_{Fe}} + \frac{\tau_p \tau_f}{\mu_{Fe} h_y (r_s + r_e)} \right) \tag{3.15}$$

The intercept of the load line equation and the demagnetization curve determines the operating point. Approximating the demagnetization curve with (3.9) produces the magnet's flux density

$$B_m = \frac{B_{rem} \tau_m \tau_f}{\tau_m \tau_f + r_m^2 \frac{\mu_{rec}}{\mu_0} \left(\ln\left(\frac{r_s}{r_m}\right) + \frac{1}{2\mu_{Fe}} + \frac{\tau_p \tau_f}{\mu_{Fe} h_y (r_s + r_e)} \right)} \tag{3.16}$$

Equations (3.15) and (3.16) define the operating point of the magnet in the slot-less electromagnetic damper. The flux densities in the various part of the device are then obtained by substituting the result from the above equation into the corresponding equation.

3.4.2 Machine Force

We use Lorentz law (3.2) to calculate the force exerted on the mover due to a current i_{circ} flowing through the coils. This current induces a magnetic flux inside the coil in the axial direction, perpendicular to the air-gap flux produced by the permanent magnet. The effect of this current induced field on the air-gap field is neglected.

Let pN_a the number of active coil turns, that is the number of turns crossing the magnetic flux at any given time, then the force is given by

$$F_d = pN_a \oint i_{circ} d\vec{l} \times \vec{B}_g \tag{3.17}$$

where $d\vec{l}$ is the direction tangential to the coil and $\vec{B}_g$ is magnetic flux density through the coil in the radial direction, thus perpendicular to the coil. Substituting the value (3.13) for B_g into the above equation gives the damper force in terms of the circuit current and device parameters

$$F_d = pN_a \left(2\pi r\, i_{circ}\right) \frac{r_m^2}{2\tau_f r} B_m = \pi\, pN_a \frac{r_m^2}{\tau_f} B_m i_{circ} = K_{t,f}\, i_{circ} \tag{3.18}$$

The term $K_{t,f} = \pi\, pN_a B_m\, r_m^2 / \tau_f$ is known as the force constant of the machine and has, in the SI system, units of [N/A]. In a passive damper the circuit current, and therefore the force, is determined by the electric circuit connected to the damper and the voltage induced by the translation of the mover.

3.4.3 Open Circuit Induced Voltage

To facilitate the derivation of the induced voltage or electromotive force on the coil due to the mover translation, let us "flatten" the machine as shown in Figure 3.8 so that the coils are open conductors perpendicular to both the air gap magnetic flux and the mover translation.

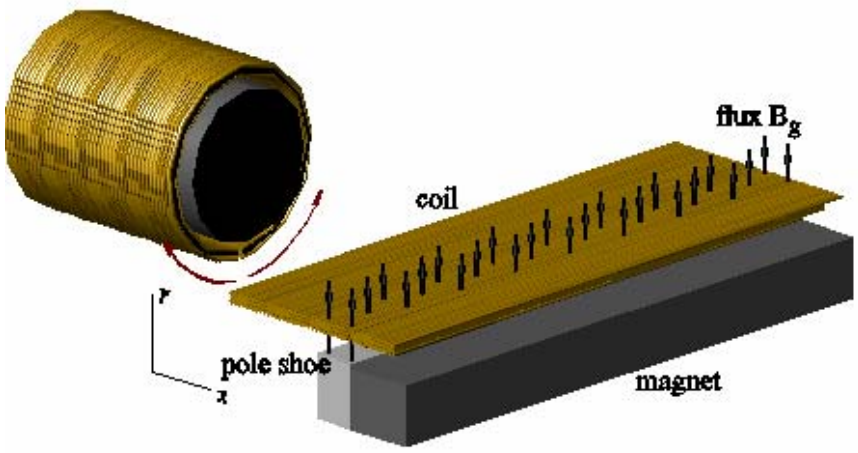

Figure 3.8 Conceptual Flattening of the Tubular Electromagnetic Damper.

Consider a contour *C* on the flattened damper, as shown in Figure 3.9, such that one side coincides with a single coil turn under open circuit condition (i.e. $i_{circ} = 0$) and its enclosed surface *S* overlaps the translator pole shoe, and therefore the working air gap flux, by a distance x in the axial direction. The right side of Faraday's equation (3.4) becomes

$$-\int_S \frac{\partial}{\partial t}\vec{B}\cdot d\vec{s} = -\frac{d}{dt}\left(B_g\, 2\pi\, r\, x\right) = -2\pi B_g r v \tag{3.19}$$

where v is the relative velocity between the translator and the coil. The gap flux density is assumed time invariant and is given by equation (3.13).

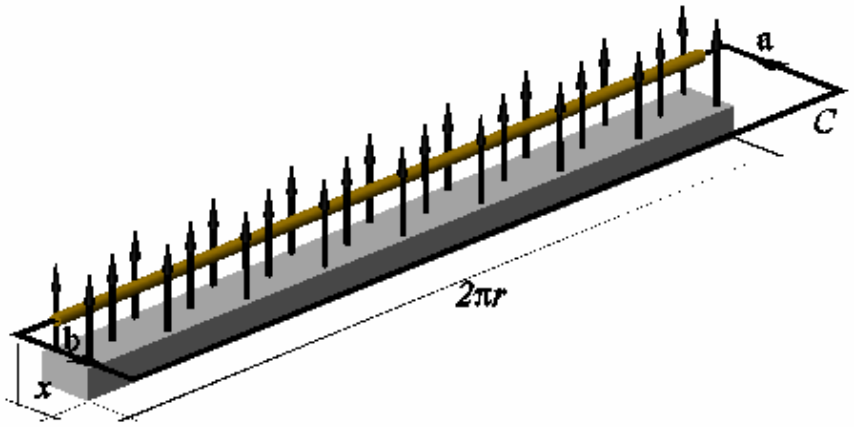

Figure 3.9 Flat Damper with Single Turn Coil and Integration Contour.

The left side of Faraday equation is just the potential difference, or voltage, between the open ends of the coils,

$$\oint_C \vec{E}\cdot d\vec{l} = \int_b^a \vec{E}\cdot d\vec{l} + \int_a^b \vec{E}\cdot d\vec{l} = -V_{ab} + R_{turn} i_{circ} = -V_{ab} = -2\pi B_g r v \tag{3.20}$$

Equating the two sides gives the induced or back emf voltage on a single turn of the coil. Since there are pN_a turns connected in series that are being linked by the air gap magnetic flux, the total open circuit voltage induced in the damper is

$$V_{emf} = \pi\, pN_a B_m \frac{r_m^2}{\tau_f} v = K_{t,e} v \tag{3.21}$$

The term $K_{t,e} = \pi\, pN_a B_m\, r_m^2 / \tau_f$ is known as the voltage or electromotive-force (emf) constant of the machine and has the same numerical value as the force constant, but with units expressed now as [Vs/m]. Notice that dimensionally[1], N/A and Vs/m are equivalent since the unit of Newton is equivalent to CV/m.

The damper machine constant is thus naturally defined as $K_t = K_{t,e} = K_{t,f}$. This machine constant is expressed below in terms of the geometric and magnetic properties of the device as

$$K_t = \frac{\pi r_m^2 pN_a B_{rem} \tau_m}{\tau_m \tau_f + r_m^2 \dfrac{\mu_{rec}}{\mu_0}\left(\ln\left(\dfrac{r_s}{r_m}\right) + \dfrac{1}{2\mu_{Fe}} + \dfrac{\tau_p \tau_f}{\mu_{Fe} h_y (r_s + r_e)}\right)} \tag{3.22}$$

This constant determines, together with the electrical circuit parameters, the force-velocity constitutive relation of the electromagnetic damper.

3.4.4 Non-Ideal Winding Parameters

When current flows through the coils (circuit is closed) the non-ideal properties of the windings become evident and need to be considered. First, the finite conductivity of the winding causes a voltage drop in the coils, following Ohm's law, dissipating energy and making the terminal voltage of the device lower than the voltage induced by the translator motion. Second, an axial magnetic flux inside the coil develops as a result of the current, and it manifests itself as a circuit

inductance. This inductance introduces a delay between the induced emf and the current which translates in a delay between the applied movement and the reaction force.

The resistance of each coil is computed by adding the total number of turns in the coil N_w and the average radius of the coil $(r_i + r_s)/2$. Since all the coils are connected in series, the total winding resistance is given by

$$R_{coil} = p \frac{r_i + r_s}{r_w^2 \sigma} N_w \tag{3.23}$$

where σ is the conductivity of the coil material (copper), r_w is the radius of the coil wire cross-section, and p is the number of poles or coils.

In general, the inductance varies with the relative position of the mover inside the winding, since the material inside the winding and hence the flux produced by the current changes. However, when the length of the translator equals the length of the coil ($\tau_w = \tau_m + 2\tau_f$) and its movement is constrained as to avoid the edges of the winding, the coil inductance is independent of position and can be approximated as,

$$L_{coil} = \frac{\mu_0 \mu_{Fe} \pi r_i^2 p N_w^2}{2\tau_f + 2\mu_{Fe}(\tau_w - \tau_f)} \tag{3.24}$$

where the geometric variables are as defined beforehand in Table 3.2 and $\mu_0 \mu_{Fe}$ is the permeability of iron. For the sake of continuity in the presentation, the derivation of (3.24) is presented in appendix A together with assumptions and approximations used.

3.4.5 Two-Port Model

Based on the relationships derived in the preceding subsections, the electromagnetic damper can be represented as a two-port device (Figure 3.10) coupling the mechanical and electrical domains via an ideal transformer relationship

---

[1] Albeit the same, in practice the values measured for the back-emf and force constants might be slightly different due to losses not accounted for in their model.

$$\begin{cases} e = K_t v \\ F_d = K_t i \end{cases} \tag{3.25}$$

where K_t is the damper machine constant defined by equation (3.22).

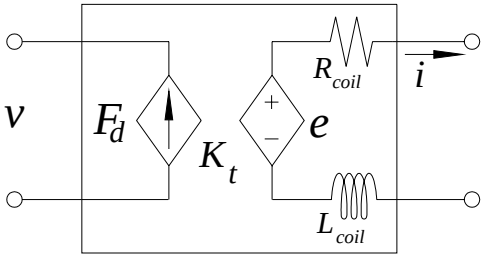

Figure 3.10 Representation of the Electromagnetic Damper Two-Port Device.

The coil resistance and inductance model the non-ideal characteristics of the device in the electric side. Losses of mechanical origin, such as friction, are neglected as these losses can be modeled as part of the mechanical network attached to the damper.

3.4.6 Force-Velocity Relationship

When a velocity is prescribed to the damper, the electrical load connected to the damper determines the relationship between the circuit current i and the induced emf e. If the load is a resistor R_{load} then the circuit equation is

$$e = (R_{coil} + R_{load})i + L_{coil}\frac{di}{dt} \tag{3.26}$$

Substituting the transformer relationships into the above equation and rearranging terms results in the force-velocity constitutive relation for the passive electromagnetic damper

$$L_{coil}\frac{dF_d}{dt} + (R_{coil} + R_{load})F_d = K_t^2 v \tag{3.27}$$

From the mechanical (structural) point of view, the electromagnetic damper behaves as a linear mechanical damper, with a time delay component, whose properties are set by the damper machine constant and the electrical circuit components. The solution to the damper equation, and therefore the value of the reaction force, depends on the form of the velocity function, *v*.

3.5 Electromagnetic Damper Model Behavior

3.5.1 Sinusoidal Response

If the applied velocity profile has a sinusoidal form $v = \hat{v}\cos(\omega t)$ then the force response is composed of a transient term and a sinusoidal term,

$$F_d = \Im K_t e^{-\frac{R_{circ}}{L_{coil}}t} + \frac{K_t^2}{\sqrt{(R_{circ})^2 + (\omega L_{coil})^2}}\hat{v}\cos(\omega t + \phi_d) \tag{3.28}$$

where $R_{circ} = R_{coil} + R_{load}$ and the coefficient $\Im$ depends on initial conditions.

After the transient term fades away, the steady-state damper force is also sinusoidal with a time shift in relation to the applied velocity signal. The form of the force-velocity relationship is similar to that of an ideal damper (3.1), with the exception of the phase shift, where the damping coefficient and phase shift (time delay) are given by

$$c_d = \frac{K_t^2}{\sqrt{(R_{circ})^2 + (\omega L_{coil})^2}} = \frac{K_t^2}{R_{circ}\sqrt{1 + (\tau_d \omega)^2}} \tag{3.29}$$

$$\phi_d = \tan^{-1}\left(-\frac{\omega L_{coil}}{R_{circ}}\right) = \tan^{-1}(-\tau_d \omega) \tag{3.30}$$

Here, $\tau_d = L_{coil}/R_{circ}$ is defined as the damper time constant.

The equations above show that for sinusoidal excitation, the magnitude of the damping coefficient and the phase shift angle depend not only on the systems components, but also on the frequency of the excitation signal.

A decrease in frequency minimizes the inductance effect, so the damping coefficient approximates K_t^2/R_{circ} while the phase shift vanishes. For a sinusoidal excitation, an ideal damper approximates the electromagnetic damper under two cases: when the coil inductance is much smaller than the circuit resistance; or the frequency of excitation is small compared to the device time constant.

3.5.2 Damper Force-Velocity Relationship

The relationship between the force and the velocity presents a time delay, or phase shift, caused by the inductance of the coil. This phase shifts causes the force-velocity curve to deviate from the straight line expected from an ideal damper. For a given frequency of excitation, the force velocity curve is elliptical in shape, and a general example is presented in the following two figures. The ellipse orientation and shape vary according to the relative values of inductance and resistance in the network.

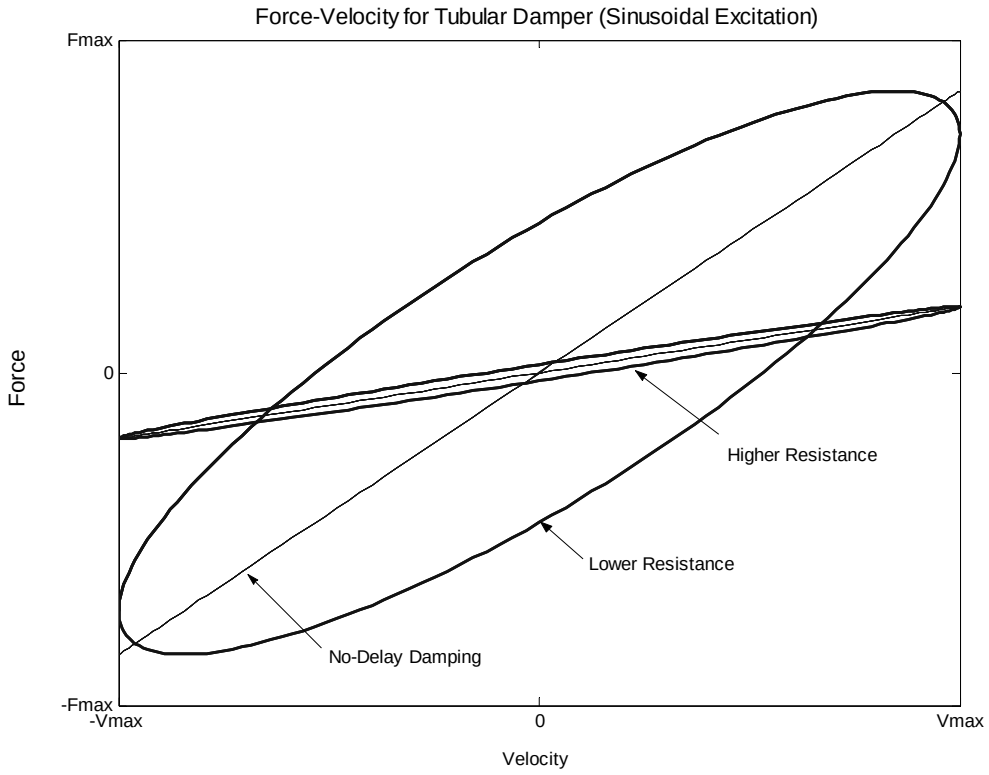

Figure 3.11 Force-Velocity Response with Varying Resistance and Fixed Inductance.

Figure 3.11 shows the effect of changing the circuit resistance while keeping the inductance constant. In Figure 3.12, the inductance varies while the resistance is kept constant. Both figures show that as the circuit impedance becomes more resistive the ellipse becomes flatter, approximating the ideal damper curve (a straight line). In addition, as the total impedance increases, the slope of the ellipse's major axis decreases, i.e. the damping coefficient decreases with increasing impedance.

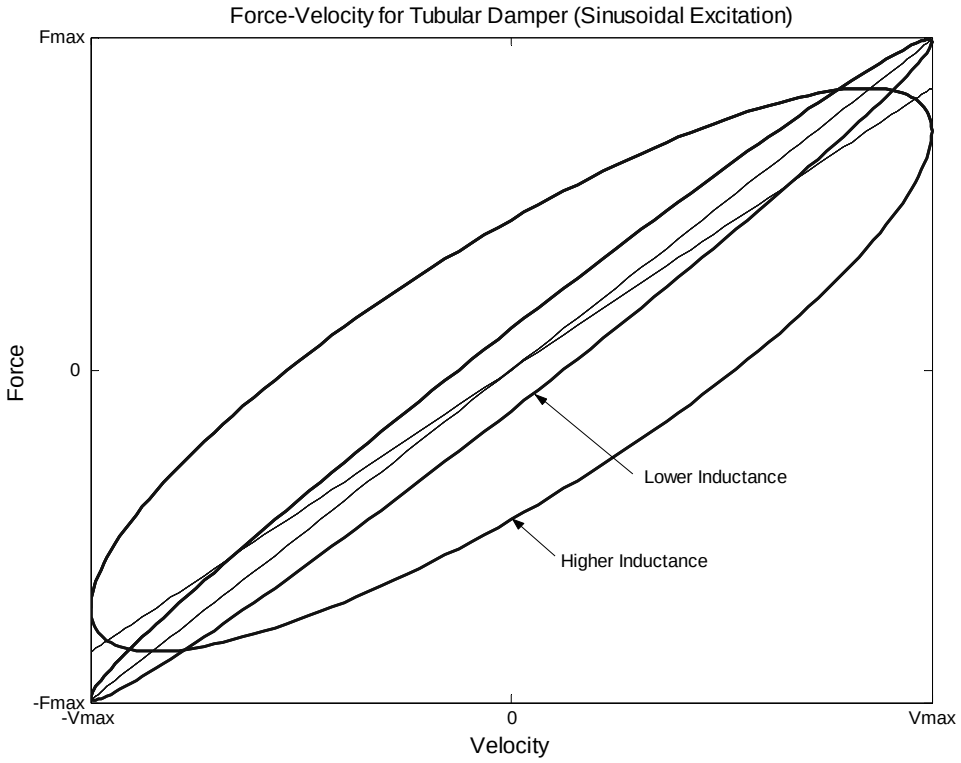

Figure 3.12 Force-Velocity Response with Varying Inductance and Fixed Resistance.

3.5.3 Damper Energy Dissipation

The energy (power) dissipation capability of the electromagnetic damper depends on the total circuit resistance. Energy imparted to the device will dissipate as heat both internally on the coil, and externally on the load resistance.

For a given instantaneous damper speed *v*, the current in the circuit is given by $i_{circ} = V/R_{circ} = K_t v/R_{circ}$. Expressing the load resistance in terms of the coil resistance as $R_{load} = \alpha R_{coil}$ so that the total circuit resistance is $R_{circ} = R_{coil}(1+\alpha)$, then the power dissipation in the resistances in terms of the damper coefficient and velocity is given by

$$P_{coil} = R_{coil} i_{circ}^2 = \frac{K_t^2 v^2}{R_{coil}(1+\alpha)^2} = \frac{c_{d,\max}}{(1+\alpha)^2} v^2 \tag{3.31}$$

$$P_{load} = R_{load} i_{circ}^2 = \frac{\alpha}{(1+\alpha)^2} \frac{K_t^2 v^2}{R_{coil}} = \frac{c_{d,\max} \alpha}{(1+\alpha)^2} v^2 \tag{3.32}$$

where $c_{d,\max}$ is the damping coefficient obtained at short-circuit condition.

Figure 3.13 shows the normalized variation in internal and external power dissipation in the damper as a function of the ratio of load resistance to coil (internal) resistance.

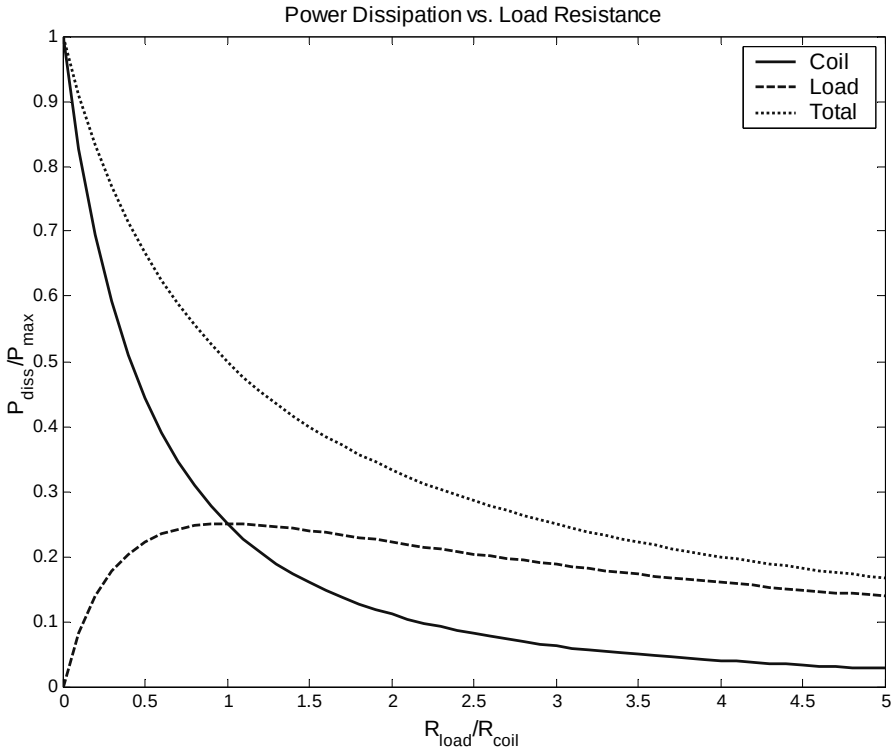

Figure 3.13 Damper Power Dissipation as a Function of Load Resistance.

The above equations and figure show that as the load resistance increases, the total energy dissipation decreases, but the proportion of energy dissipated externally increases while the internal dissipation decreases. Maximum energy dissipation and damping occurs when the coil is short circuited (no load resistance). Under this condition all the energy is dissipated internally, similar to an eddy current damper. When the load and coil resistances are matched, that is both resistances are equal, the power dissipated on the external load is at a maximum and equals the power dissipated on the coil. At this condition, the damping coefficient and the total energy dissipated are half the maximum values obtained with no load resistance.

The operating temperature of the machine relates directly to the power dissipated internally in the device. To find an estimate of the operating temperature, we assume that under steady-state

operation, the temperature is constant throughout the device and the heat generated in the coil dissipates to the outside of the machine by convection with the surrounding air. Therefore, the temperature difference between the machine and the ambient is given by the convective energy balance equation

$$P_{coil} = h_o A_s \left(T_s - T_{amb}\right) \tag{3.33}$$

where h_o is the convective heat transfer coefficient around the machine stator, A_s is the exposed machine surface area for heat dissipation, T_s is the stator surface temperature, and T_{amb} is the ambient temperature.

Substituting (3.31) into (3.33) and assuming that only the external cylindrical surface of the damper acts as the dissipation surface, the temperature difference between the machine and the ambient under sinusoidal steady state is

$$\Delta T = \frac{c_{d,\max}}{4\pi r_e \tau_w h_o \left(1+\alpha\right)^2} \hat{v}^2 \tag{3.34}$$

where $\hat{v}$ is the sinusoidal velocity amplitude driving the damper. Note that this temperature difference is an upper bound temperature, since the heat transfer analysis performed in this section is neglecting radiation and heat transfer through the other machine surfaces.

We can see from the above equation that for a given machine topology, the operating temperature can be reduced by transferring the dissipation to the external load resistance ($\alpha > 0$), by increasing the convective heat transfer coefficient, or by limiting the amplitude of the driving velocity.

3.6 Summary

This chapter proposed and analyzed a moving magnet, tubular linear machine as a structural electromagnetic damper. This configuration presents several advantages over other linear machine configurations, among those the enclosure of all its components in a piston-like assembly and the ability to convert the kinetic energy into electric energy without requiring an external excitation.

This chapter also derived the mathematical model for the tubular permanent magnet damper using quasi-static electromagnetic theory and demonstrated that the permanent magnet linear electric machine behaves as a mechanical damper. The force-velocity constitutive relationship (3.27) of the machine is a first-order differential equation with coefficients that depend on the geometric, magnetic and electric properties of the device. The damper machine constant, given by (3.22), the coil resistance (3.23) and the coil inductance (3.24), together with the load resistance connected to the electrical side of the damper make up the coefficients of the damper equation.

The feasibility of applying this device to full-scale buildings is presented in the next chapter from the physical and economical points of view, followed by the design tools needed to apply the electromagnetic damper to buildings and to analyze the buildings with this new type of dampers.

Chapter 4
Feasibility of the Structural Electromagnetic Damper

4.1 Introduction

The mathematical model equations of the electromagnetic damper derived in the previous chapter (§3.4) determine the effective damping coefficient of the machine given its dimensional and physical parameters, and are the basis for the feasibility study performed in the current chapter. To the best of the author's knowledge, this is the first study of the applicability of the electromagnetic damper to full-scale buildings.

Two performance measures (§4.3) are used to asses the feasibility of the prototype tubular electromagnetic damper (§4.2) in a building structure: the damping density and the cost. The first value is a measure of the machine volume required to achieve a given damping performance, while the second value is a measure of the economic viability of the machine. The physical limitations of the device (§4.4), and its cost (§4.6) are investigated based on these measures, and its theoretical performance compared to that of viscous fluid dampers (§4.7). The benefits from using electromagnetic dampers instead of current damping technologies are also discussed (§4.8).

4.2 Prototype Machine Description

The feasibility study is based on a tubular damper with *p* poles, like the one depicted in Figure 4.1. This machine has the following characteristics:

- The permanent magnets have axial magnetization.
- The stator is slot-less with a single-phase winding.
- There is no change in the polarity through the machine stroke, thus the machine stroke equals the magnet length, $\tau_m = l_{Stroke}$.

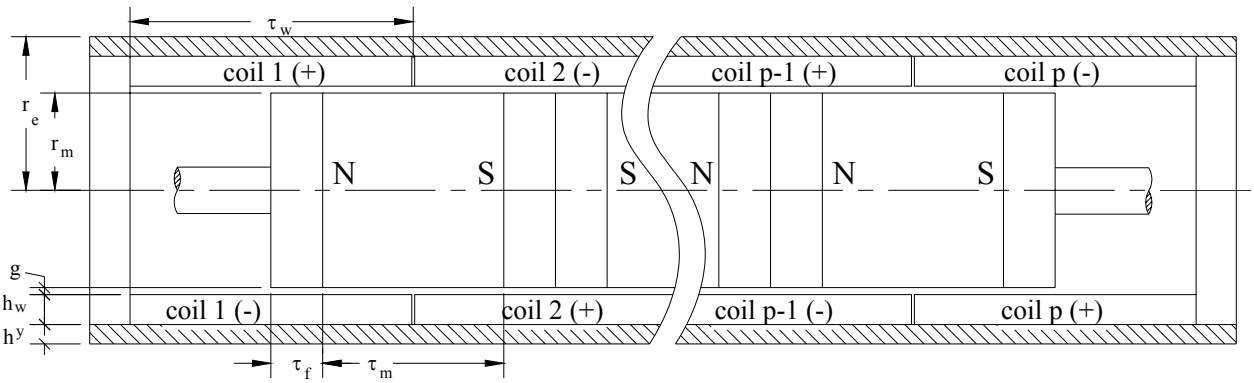

Figure 4.1 Tubular Electromagnetic Damper with *p* poles.

- The length of a coil equals the mover length of a two-pole machine, i.e. $\tau_w = \tau_m + 2\tau_f$.

4.3 Performance and Feasibility Measures

4.3.1 Damping Density

The maximum damping coefficient attained by a machine like the one shown in Figure 4.1 is proportional to the number of poles *p* and occurs when the device terminals are short-circuited (zero load resistance). Neglecting frequency and coil inductance effects, the maximum damping coefficient is

$$c_{d,\max} = \frac{K_t^2}{R_{coil}} = \frac{\left(p\pi B_m r_m^2 N_w / \tau_w\right)^2}{pN_w\left(r_i + r_s\right)/\left(\sigma_{Cu} r_w^2\right)} = \tilde{c}_{d,\max} p \tag{4.1}$$

where $\tilde{c}_{d,\max}$, the maximum damping coefficient per pole, depends on the geometric and physical properties of the machine pole. Using a non-zero load resistance causes a reduction in the maximum damping coefficient and the energy dissipation (see Figure 3.13), but also shifts the dissipation to the external load resistor.

The volume for the same machine is

$$V_d = p\pi\tau_w r_e^2 = \tilde{V}_d p \tag{4.2}$$

where r_e is the external radius of the machine, τ_w is the length of a single coil, and $\tilde{V}_d = \pi\tau_w r_e^2$ is the volume per machine pole. From the above two equations, it can be seen that by varying the

number of poles in the machine, the damping coefficient can be changed, but with a corresponding change in the machine volume.

Although the damping coefficient is a good measure of a damper performance, a better comparison measure between different types of damping devices is the damping density, defined as the damping capacity per unit volume,

$$\gamma_d = \frac{c_d}{V_d} = \frac{\widetilde{c}_d\, p}{\widetilde{V}_d\, p} = \frac{\widetilde{c}_d}{\widetilde{V}_d} \tag{4.3}$$

This measure is independent of the number of poles used in the machine, and depends only on the geometric and physical properties of the material in a single pole of the machine. In addition, this measure permits the comparison of the electromagnetic damper with other types of dampers, like fluid viscous dampers, as it is a measure of the volume efficiency of dampers. This comparison will be made in section §4.7.

4.3.2 Damping Cost

The cost estimation of the machine uses the price of commercially available neodymium (NdFeB) magnets, and the wholesale price of copper and steel. Table 4.1 shows the material costs used. Development and manufacturing costs are not taken into consideration.

The following formula gives the price per pole $\widetilde{\$}_d$ of the machine,

$$\widetilde{\$}_d = \widetilde{V}_{Fe}\rho_{Fe}\$_{Fe} + \widetilde{V}_{Cu}\rho_{Cu}\$_{Cu} + \widetilde{V}_m\rho_{NedFeB}\$_{NdFeB} \tag{4.4}$$

where $\widetilde{V}_i$, ρ_i and $\$_i$ are the volume per pole, density and price, respectively, of the i^{th} material.

Table 4.1 Sample Prices of EM Damper Materials

Material	Typical Density (kg/m^3)	Typical Price (per kg)
Steel	8.0×10^3	\$0.50
Copper	8.9×10^3	\$3.00
NdFeB Magnet	7.5×10^3	\$66.00

Another comparison measure used to evaluate a particular electromagnetic damper design is the

damping cost, defined as the price per damping unit,

$$\tilde{\chi}_d = \frac{\tilde{\$}_d}{\tilde{c}_d} \tag{4.5}$$

4.4 Damping Capacity Analysis

This study determines numerically (scripts in Appendix E) the maximum damping density achievable by the electromagnetic damper using the equations developed in the previous chapter. Table 4.1 lists the properties of the materials used in the electromagnetic damper.

Table 4.2 Electromagnetic Damper Material Properties

Material	Type	Properties
Permanent Magnets	NdFeB N35	$B_{rem}=1.2T$, $H_c=900kA/m$ $T_{oper}=200°C$
	NdFeB N55	$B_{rem}=1.5T$, $H_c=1080kA/m$ $T_{oper}=80°C$
Copper	Magnet Wire	$\rho_{cu}=1.77x10^{-8}\ \Omega$-$m$ $\mu_r=1$
Iron	Magnetic Steel	$\mu_r=2000$ $B_{sat}=2.0T$

Table 4.3 shows the principal dimensions and range of values considered for this analysis. The external radius and coil length of the machine are computed such that the permanent magnet operation point is approximately at the maximum energy product location and the iron's magnetic flux density in the machine is below the iron's saturation value.

Table 4.3 Damper Independent Dimensions and Values.

Parameter	Symbol	Min. Value	Max. Value
Magnet Length (Machine Stroke)	τ_m	5mm	250mm
Magnet Radius	r_m	20mm	150mm
Air Gap	g	0.25mm	5.0mm
Coil Wire Radius	r_w	AWG40 (0.04mm)	AWG0 (4.1mm)
Coil Layers (Coil Height)	N_r (h_w)	1 Layer	30 Layers

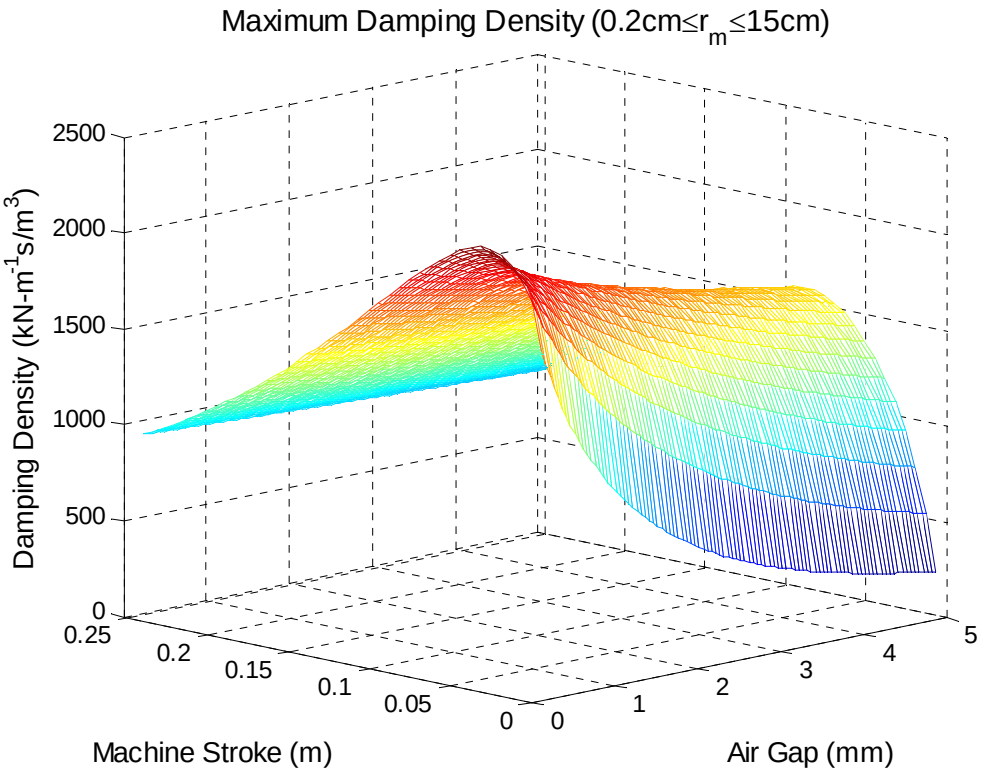

Figure 4.2 Maximum Damping Density as a Function of Air-Gap and Magnet Length (N35 Magnet).

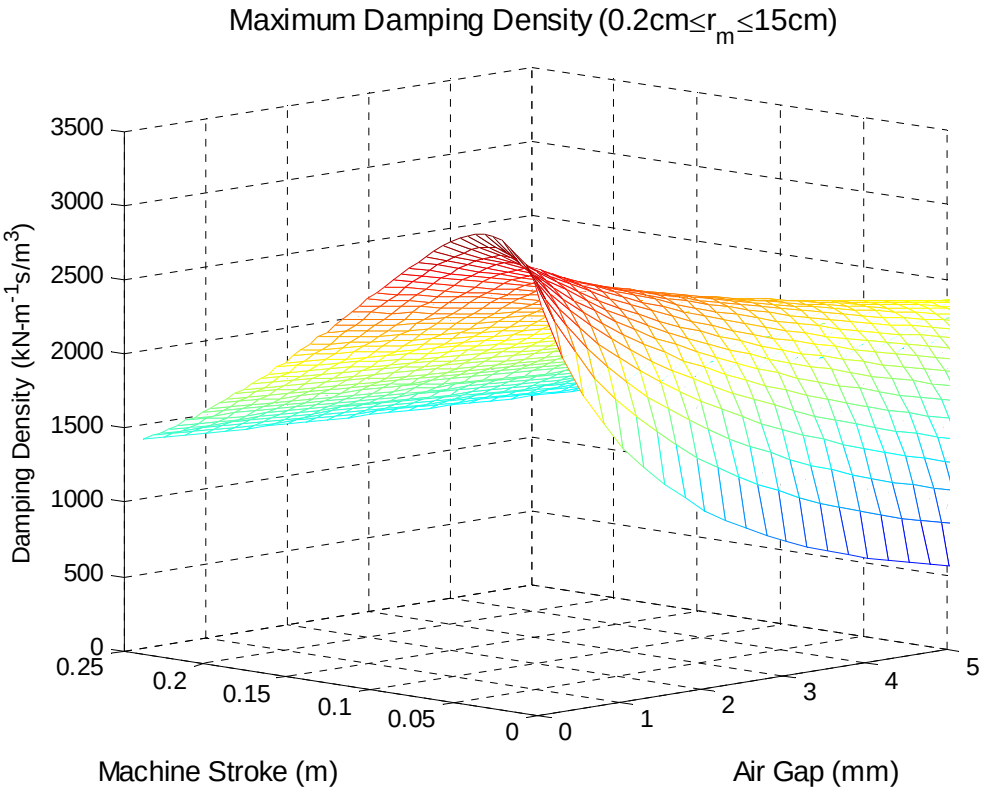

Figure 4.3 Maximum Damping Density as a Function of Air-Gap and Magnet Lenght (N55 Magnet).

Figure 4.2 and Figure 4.3 show the variation on the maximum damping density as a function of air-gap and machine stroke length. The first figure corresponds to the grade N35 sintered neodymium magnet, while the second figure corresponds to grade N55 neodymium magnet.

The figures show that the electromagnetic damper is capable of achieving a damping density of approximately 2000kN-m^{-1}s/m^3 using grade N35 magnets and approximately 3000kN-m^{-1}s/m^3 when using grade N55 magnets. These limits are for a damper with no-load resistance, that is, a short-circuit coil condition. An increase of the load resistance decreases the damping density and energy dissipation capability of the machine.

N55 grade neodymium magnets have better damping density performance than N35 magnets, however they have a lower limit for the operation temperature: 80°C instead of 120°C. This lower operating temperature limits the amount of energy than can be dissipated internally by the machine with N55 magnets, and therefore would require special ventilation considerations or higher load resistances to shift the energy dissipation outside the device, with the corresponding penalty on the damping density value.

Table 4.4 shows the achievable damping densities when using the N35 magnet for three different air gap thicknesses and various magnet lengths. These damping density values are for two load resistance conditions: zero load resistance and matched load resistance. The table also shows the corresponding machine dimensions, coil length and external radius.

Table 4.4 Achievable Damping Density for Sample Air Gaps and Load Resistances.

Magnet	**Air Gap (mm)**	**Magnet (mm)**		**Machine (mm)**		**Damping Density (kN-m^{-1}s/m^3)**	
		Length	**Radius**	**Length**	**Radius**	***0***	***R_{coil}***
N35	0.5	50	60	78	80	1683	842
	0.5	50	150	100	180	2191	1095
	1.0	25	60	52.7	74.3	1803	902
	1.0	60	150	117	183	2064	1032
	5.0	90	150	164	193	1836	918

Figure 4.4 and Figure 4.5 show the maximum damping density as a function of magnet radius and coil wire radius (AWG) for a fixed air gap and magnet length (machine stroke). Again, all the sample figures presented are for the short-circuited machine condition.

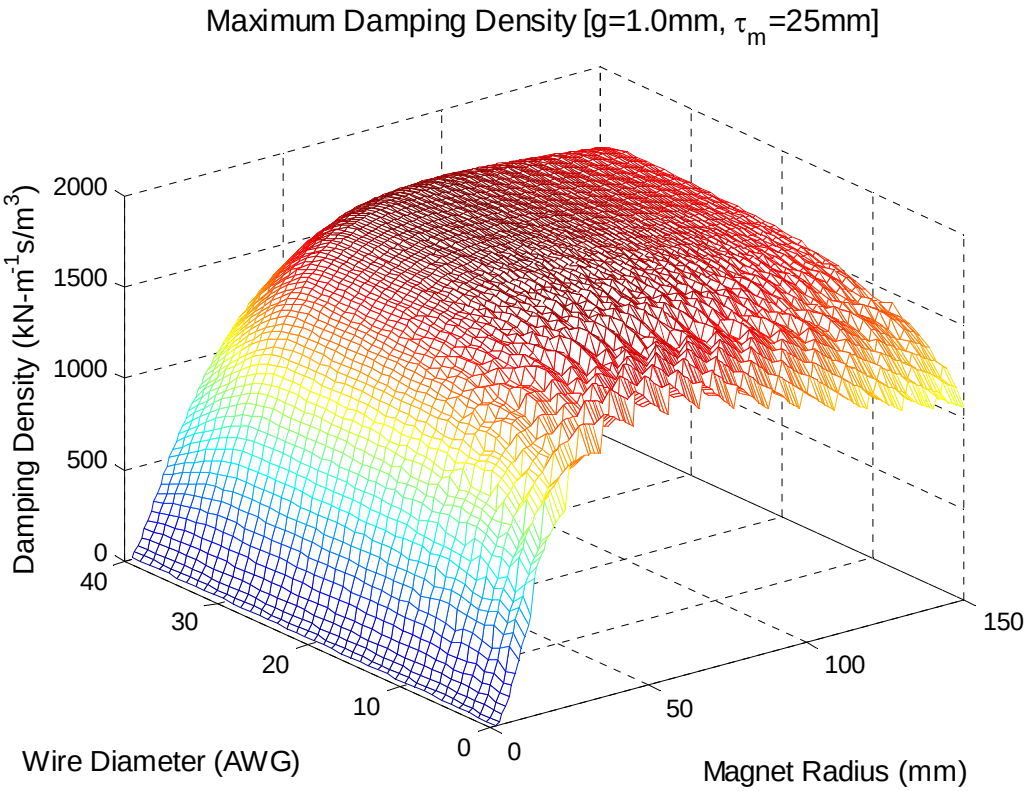

Figure 4.4 Maximum Damping Density as a Function of Magnet Radius and Wire Gauge (N35 Magnet).

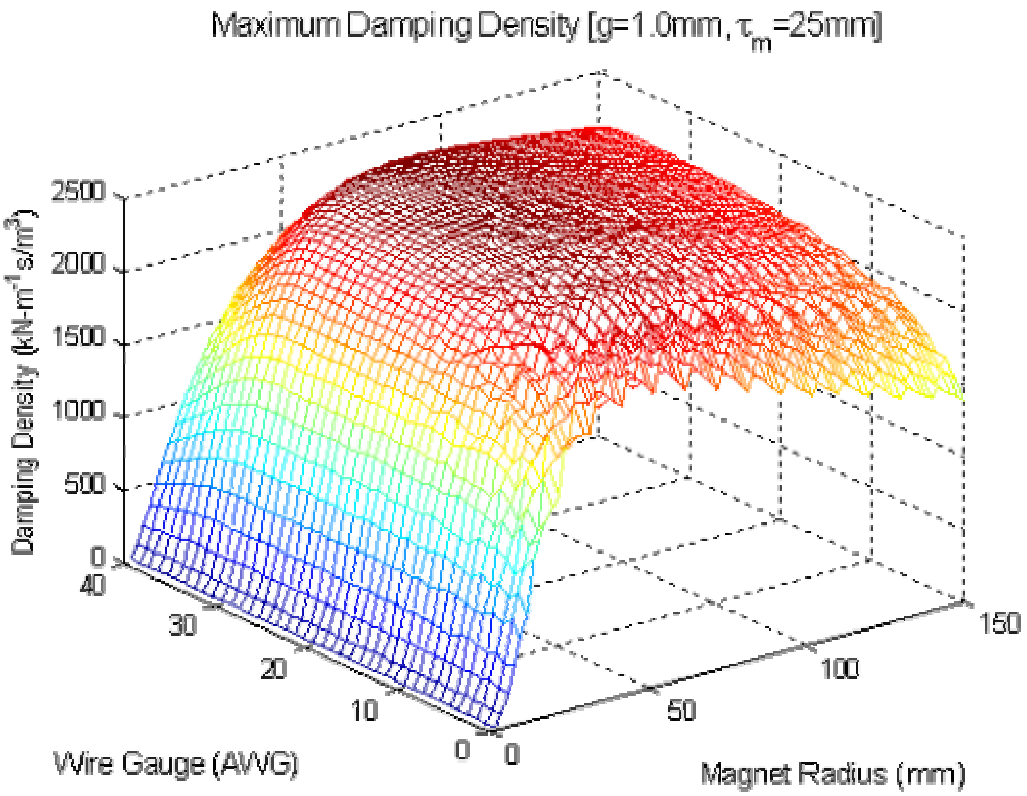

Figure 4.5 Maximum Damping Density as a Function of Magnet Radius and Wire Gauge (N55 Magnet).

The last two figures show that the damping density reaches maximum values for magnet radii greater than approximately 50mm and coil wire diameters between 10 and 30AWG. The above analysis computed the damping density using the hypothetical values presented in Table 4.3. Current manufacturing technology limits the size of neodymium permanent magnets to a radius of approximately 50mm and a length of approximately 100mm, therefore the limiting factor for the practical damping densities is the permanent magnet used in the machine. Bigger monolithic magnets are available in other materials, such as Anilco or ceramics; however, these materials have a substantially smaller energy product than the NdFeB magnets, and therefore result in a lower damping performance. Table 4.5 shows the maximum damping density achievable with various permanent magnet materials and the corresponding damping cost, together with their basic properties values.

Table 4.5 Performance Comparison with Various Permanent Magnet Materials.

Material	Grade	B_{rem} (T)	H_c (kA/m)	BH_{max} (kJ/m^3)	T_{oper} (°C)	Max Density (kN-m^{-1}s/m^3)	Damping Cost ($/kN-m^{-1}s)
Anilco	A902	1.07	119.4	71.6	550	272	$201
Ceramic	C4029	0.41	222.8	32.6	310	227	$72
Sintered NdFeB	N3578	1.21	950	278	200	2296	$77
	N5563	1.5	1080	438	80	3143	$54

From the table, we can see that ceramic magnets result in a damping cost similar to NdFeB magnets, but require approximately ten times the machine volume for the same damping performance. Anilco magnet machines have a damping density similar to that of ceramic magnets and the highest operating temperature, but their damping cost is greater than both ceramic and neodymium based machines. Neodymium magnets provide the best performance, both in damping and in cost, of the various magnetic materials available currently, albeit with the lowest operating temperature limit. In the following section, we determine the limitations imposed on the machine operation because of operating temperature considerations.

4.5 Thermal Analysis

The dependency of the machine temperature on the power dissipated by the tubular electromagnetic damper was described previously by equation (3.34). That equation can be rewritten in terms of the damping density introduced previously in this chapter as

$$\Delta T = \frac{\gamma_{d,\max} r_e}{4h_o(1+\alpha)^2}\hat{v}^2 = \kappa_T \hat{v}^2 \tag{4.6}$$

where κ_T is defined as the speed temperature coefficient of the damper.

The above equation, together with the permanent magnet's maximum operation temperature, effectively introduces a lower bound to the maximum velocity at which the electromagnetic damper can operate. Table 4.6 shows the maximum operation velocities for the short-circuited electromagnetic dampers considered previously in Table 4.5.

Table 4.6 Maximum Damper Velocity due to Temperature Limits (h_o=5W/m^2°C, □=0).

Material	**Grade**	**T_{oper} (°C)**	**External Radius (m)**	**Damping Density (kN-m^{-1}s/m^3)**	**Speed Temperature Coefficient (°C s^2/m^2)**	**Max. Velocity at 25°C (m/s)**
Anilco	A902	550	0.175	272	2380	0.5
Ceramic	C4029	310	0.163	227	1850	0.4
Sintered	N3578	200	0.178	2296	20.4x10^3	0.1
NdFeB	N5563	80	0.184	3143	28.9x10^3	0.045

These velocities are worst-case limits for the EM dampers. By increasing the load resistance, the velocity limits also increase as shown in Figure 4.6. This figure shows the velocity limits for the electromagnetic damper using N35 magnets at various load resistance conditions at 25°C.

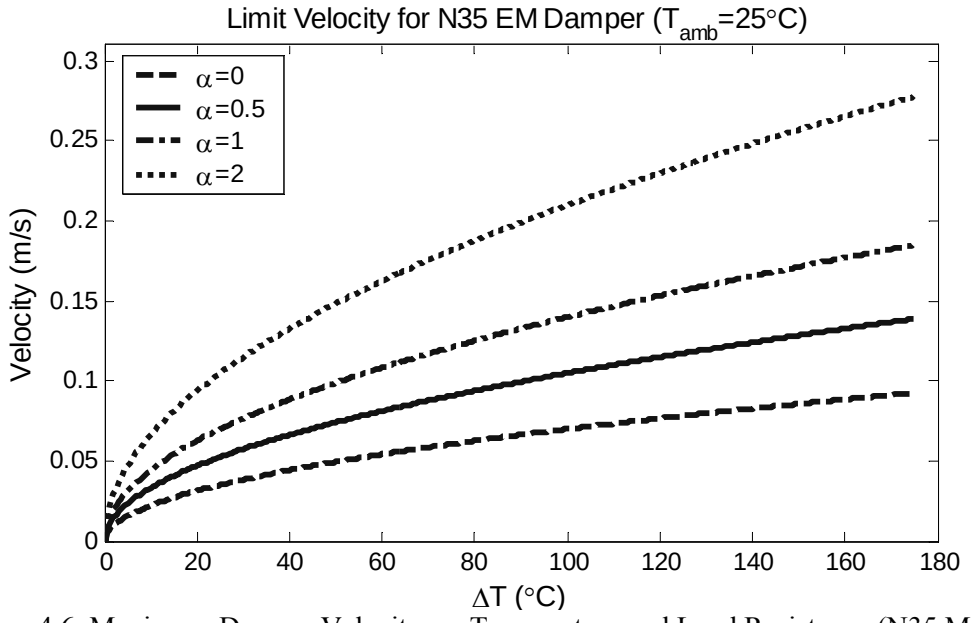

Figure 4.6 Maximum Damper Velocity vs. Temperature and Load Resistance (N35 Magnet).

The maximum temperature difference shown in the figure (175°C) corresponds to the maximum operating temperature of N35 magnets. It is interesting to note that this temperature is below the ignition temperature of most construction materials, thus electromagnetic dampers operating under steady-state conditions below the maximum allowable velocities should not be a fire hazard.

4.6 Economic Analysis

Table 4.7 shows the estimated costs of the machines presented in Table 4.4, while Figure 4.7 and Figure 4.8 show sample plots depicting the variation of the machine cost and the damping cost per pole, respectively, as a function of magnet radius and coil wire diameter. The estimated costs measures correspond to the machines that exhibit the maximum damping density (see Figure 4.4 previously) achievable a given magnet and air gap dimensions.

Table 4.7 Sample Machine Cost per Pole at Maximum Damping Density.

Magnet	Air Gap (mm)	Magnet (mm)		Max. Damping Density ($kN\text{-}m^{-1}s/m^3$)	Cost per pole	Damping Cost
		Length	Radius			
N35	0.5	50	60	1683	$285	$108.98
	0.5	50	150	2191	$1779	$79.77
	1.0	25	60	1803	$143	$86.78
	1.0	60	150	2064	$2136	$84.07
	5.0	90	150	1836	$3212	$91.16

Both the table and Figure 4.7 show that as the radius of the magnet increases, the cost of the machine also increases. Figure 4.8 shows that as the magnet radius increases, the damping cost tends to decrease asymptotically to about approximately $80/($kN\text{-}sm^{-1}$) independently of wire diameter.

The cost estimate is based solely on the cost of the main damper materials: copper for the winding, iron for the stator and pole shoes, and sintered neodymium permanent magnets for the mover. The cost of supplemental hardware that would be required to build a damper was not considered. In addition, this estimate does not account for R&D and manufacturing costs. The biggest contributor to the price in the machine is the magnet material, both in terms of raw material price and quantity required.

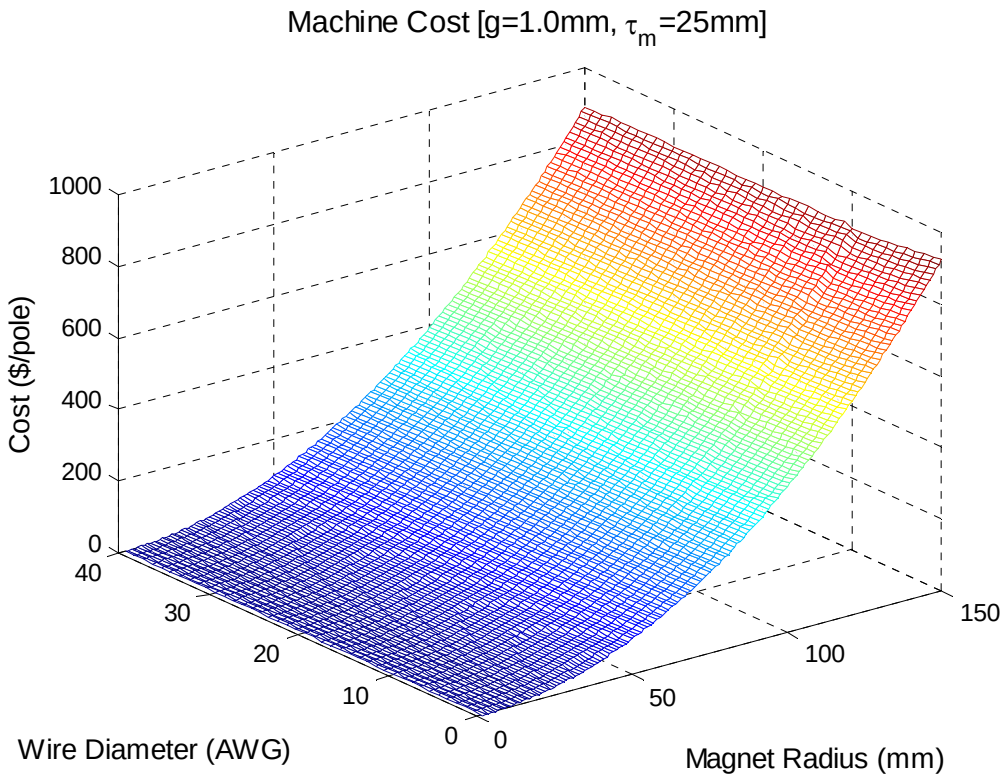

Figure 4.7 Machine Cost per Pole as a Function of Magnet Radius and Wire Gauge (N35 Magnet).

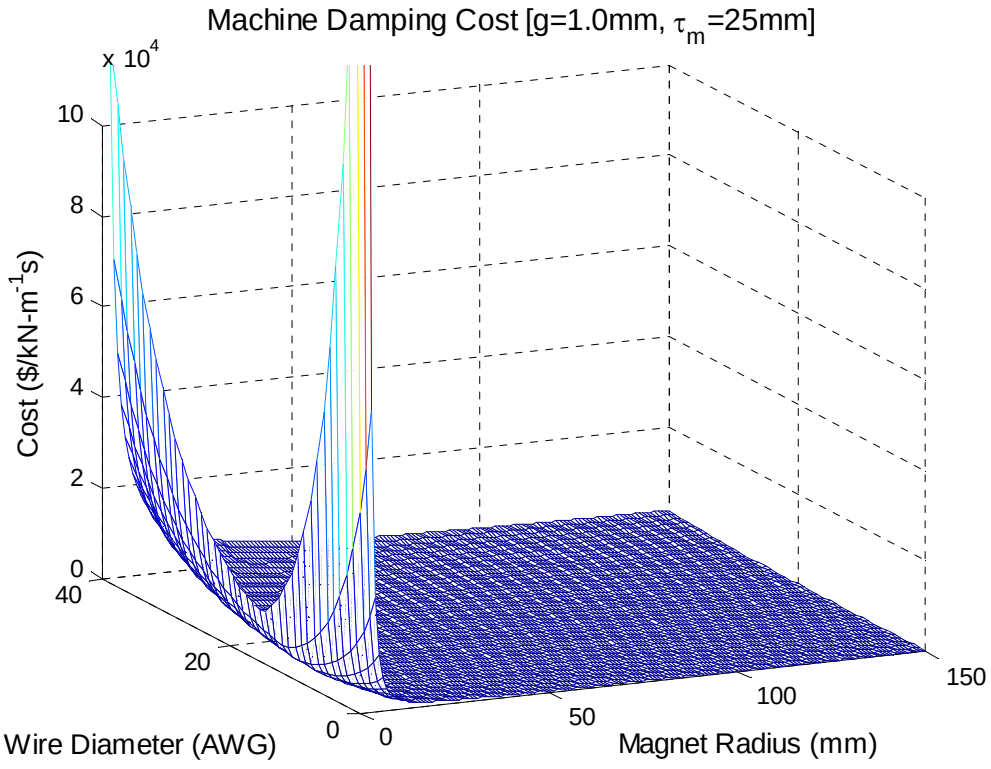

Figure 4.8 Damping Density Cost as a Function of Magnet Radius and Wire Gauge (N35 Magnet).

Two main reasons account for the high price of the electromagnetic damper at the time of this research. First, neodymium permanent magnet composition and manufacturing processes are currently under patent protection and their production and distribution closely regulated. Price should decrease once these patents expire.

Second, the damper being still a research device at this time, its price does not reflect the benefits of mass production. The cost estimates were for commercially available magnets quoted at relatively small quantities (about 20,000 units). Cost should diminish as the damper production reaches big enough quantities to take advantage from large-scale reductions in the price of materials and manufacturing costs.

4.7 Comparison to Viscous Fluid Dampers

The comparison of electromagnetic dampers to viscous fluid dampers uses the feasibility measures presented previously, namely damping density and damping cost. Two damper designs with N35 neodymium magnets and an air gap of only 0.25mm are used for the comparison study.

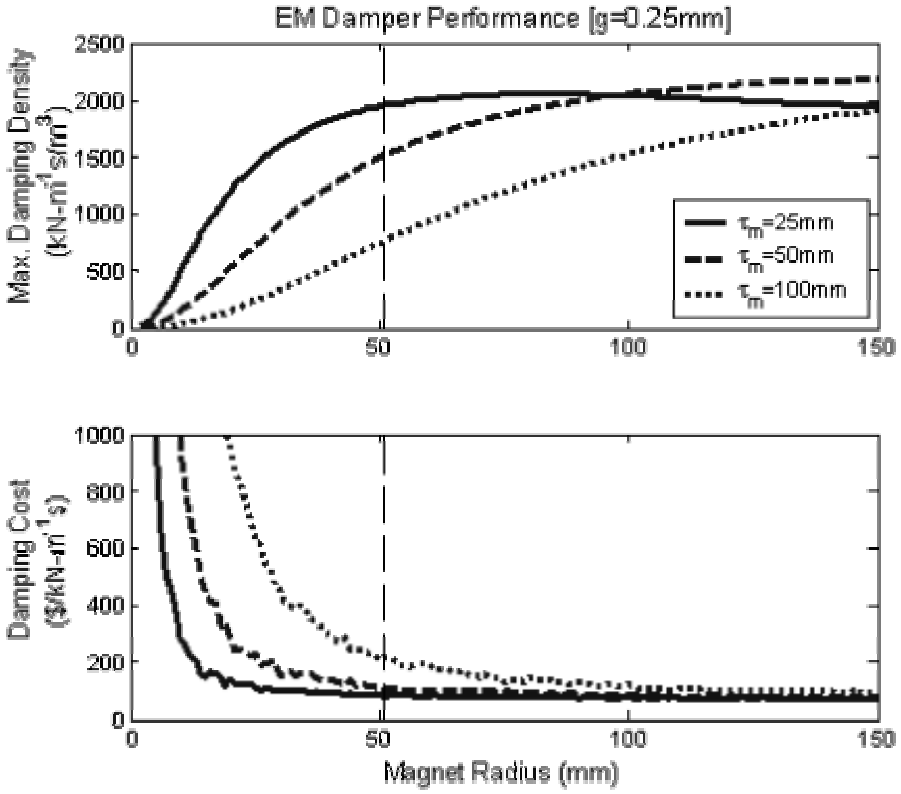

Figure 4.9 Electromagnetic Damper Performance per Magnet Length and Radius (Fixed Air-Gap).

The first damper design uses a magnet with dimensions that can be manufactured using current technology, while the second design uses the maximum magnet radius considered previously and beyond current manufacturing limits. The magnet lengths were chosen to maximize the comparison measures while minimizing the magnet material. The selection was based on Figure 4.9, which shows a graph of the performance measures in terms of other magnet radii and lengths.

Table 4.8 shows the design and performance values for the test electromagnetic dampers with no load resistance.

Table 4.8 Sample Electromagnetic Damper Performance Values. (N35 Magnet, Air-gap=0.25mm)

Magnet (mm)		Diameter (mm)	Coefficient (kN-s/m)	Damping Density ($kN\text{-}m^{-1}\ s/m^3$)	Cost/Pole	Damping Cost ($\$/kN\text{-}sm^{-1}$)
Radius	Length					
51	25	128	1.22	1958	$103	$84.15
150	50	360	22.3	2190	$1779	$79.62

The fluid dampers are actual devices manufactured by Taylor Devices Inc. and installed in the San Bernardino County Medical Center, circa 1994, and in Los Angeles City Hall seismic retrofit project, circa 2001 (Rasmussen 1997; Taylor 2003). Table 4.9 summarizes the manufacturer specifications for these dampers while Table 4.10 shows their estimated performance values form the manufacturer specifications assuming a linear force-velocity relationship.

Table 4.9 Taylor Devices Viscous-Fluid Damper Specifications.

Damper	Rated Force (kN)	Velocity (m/s)	Length (mm)	Diameter (mm)	Volume (m^3)	Stroke (mm)
San Bernardino	1423	1.52	3300	336	0.29	1200
L. A. Isolation	1334	1.27	3378	305	0.25	533
L. A. Frame	1000	0.254	1168	305	0.09	102

Table 4.10 Taylor Devices Dampers Performance Values.

Damper	Damping Coefficient (kN-s/m)	Damping Density ($kN\text{-}m^{-1}\ s/m^3$)	Device Cost	Damping Cost ($\$/kN\text{-}sm^{-1}$)
San Bernardino	934	3192	$14000	$15.00
L. A. Isolation	1051	4263	$13000	$12.37
L. A. Frame	3940	46217	$10000	$2.54

From the above tables and Figure 4.10 below we can see that the electromagnetic dampers using N35 magnets would require at least 1.6 times the volume of the fluid damper to achieve the same damping capacity as the dampers used in the San Bernardino County Medical Center or in the L.A. City Hall base isolation system. Their cost would be slightly over five times higher than fluid dampers. Compared to the dampers used in the frame of L.A. City Hall building, electromagnetic dampers require over 20 times the volume at about 32 times the cost.

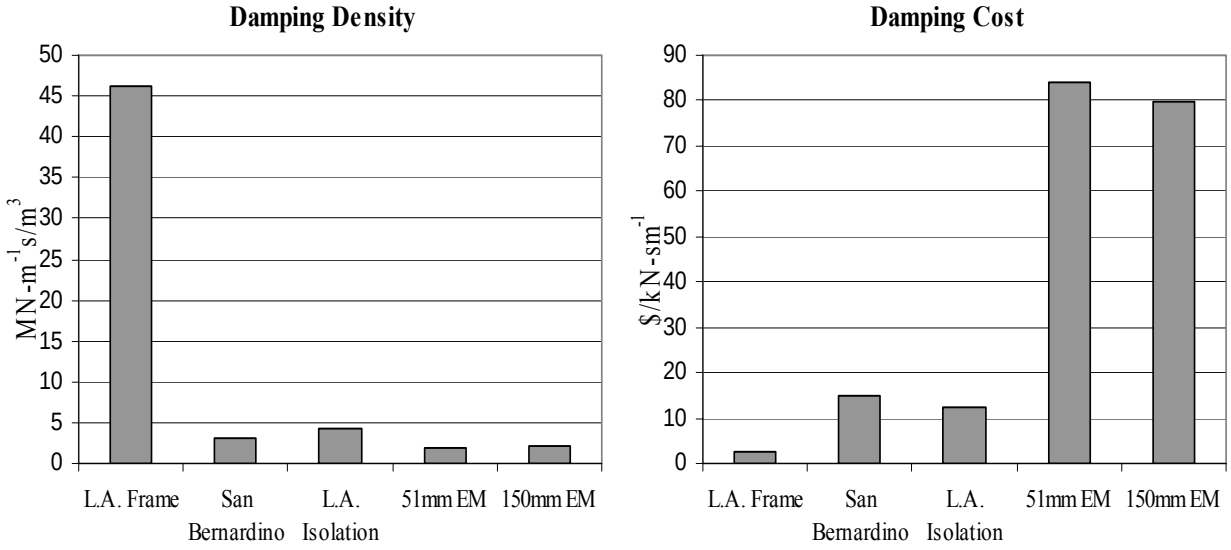

Figure 4.10 Performance Comparison between Electromagnetic and Viscous Fluid Dampers.

4.8 Advantages of the EM Damper in Buildings

The electromagnetic damper in a building provides flexibility not available with current passive structural dampers. First, the dissipation is performed electrically; therefore some of the disturbance energy can be dumped away from the device. Dissipating the energy remotely reduces the problems associated with self heating, such as parameter variations and even damage to the device, a current problem with fluid dampers, particularly under prolonged cyclic operation (Makris 1998).

Second, the force-velocity characteristic of the electromagnetic damper can be adjusted by changing the electric circuit parameters, particularly the electric load connected to the device. In contrast, adjustable fluid based dampers require specialized electro- or magneto-rheological fluids that change properties by the application of electrical or magnetic fields; solid based dampers

require mechanical adjustments in order to change their properties (Spencer et al. 1996).

Furthermore, the electromagnetic damper could be used as an actuator in an active control system by reversing the direction of energy flow. Operation of the damper as an actuator would require the use of electric drives (power supplies), which are not uncommon equipment in industrial environments, with no physical modifications to the device. Changing between the different operational modes (fully passive, semi-active and active) of the electromagnetic damper can be accomplished by means of simple switching operations, as depicted in Figure 4.11. In addition, the form of the force-velocity relationship can be adjusted by changing the type of electric load (i.e. non-linear loads) connected to the device.

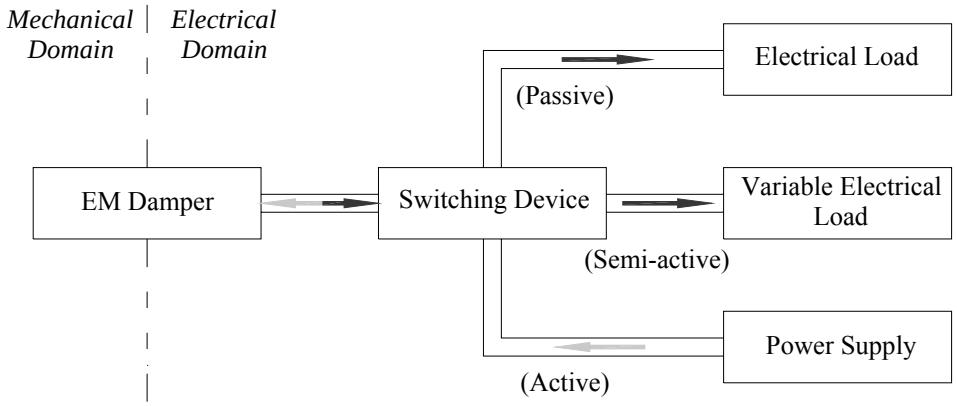

Figure 4.11 Operation Modes of the Electromagnetic Damper.

Table 4.11 compares the electromagnetic damper to current structural dampers in terms of the types of control systems application. Soon and Dargush (1997) provide a unified treatment of these devices, including application examples and case studies.

Table 4.11 Control Type Application Comparison of Passive Damping Mechanisms.

Damping Device	**Control Type Application**			
	Active	**Passive**	**Semi-Active**	**Hybrid**
Electromagnetic	✓	✓	✓	✓
Viscous Fluid		✓	✓	
Tuned Mass Damper		✓		✓
Tuned Liquid Damper		✓	✓	
Friction		✓	✓	
Metallic Yield		✓		
Hysteretic		✓		
Visco-elastic		✓		

4.9 Summary and Discussion

The current chapter is a feasibility study of the structural electromagnetic damper. Two performance measures determine the applicability of the electromagnetic damper to full-scale structures: the damping density and the damping cost. The first value is a measure of the space required to achieve a given damping performance, while the second value is a measure of the cost to achieve said damping.

The damping density limit for the electromagnetic damper is approximately 3000kN-m^{-1}s/m^3 when using N55 grade neodymium magnets, and approximately 2000kN-m^{-1}s/m^3 when using grade N35 neodymium magnets. These limits are with zero-load resistance connected to the device and all the energy dissipated internally. As the load resistance increases, the damping decreases but the amount of energy dissipated externally increases. These values of damping density are in the lower range of the sample viscous fluid dampers used for comparison. To achieve the same damping capacity, electromagnetic dampers using N35 magnets require at least 1.6 times the volume of the fluid dampers.

The price of the electromagnetic damper is over five times the price of lower-end viscous fluid dampers. This price estimate is based solely on material costs of copper, iron and neodymium permanent magnets and does not account for R&D and manufacturing costs. The machine price should decrease once the patents covering the composition and manufacturing of NdFeB magnets expire in the coming years. Further reductions should occur as the damper production reaches big enough quantities to benefit from economies of scale.

Based on the current study, the electromagnetic damper, from the physical point of view, is a feasible alternative for structural dampers, even more due to the flexibility it provides that is not available with other types of structural dampers. On the other hand, as is the case with many new technologies, the device might not be economically competitive with current technologies. However, as the technology is adopted and further developed, it should become a cost-effective solution for structural motion control.

Chapter 5
Method for Electromagnetic Damper Design

5.1 Introduction

The precedent chapters introduced the electromagnetic damper for buildings. The damper mathematical model was developed and its feasibility to full-scale building applications shown. Yet, in order to use the damper in a building or civil structure, two tools are needed: a design tool to determine the parameters of an electromagnetic damper that would achieve a specified damping; and an analysis tool to verify that using the designed damper results in the desired building dynamic response. This chapter introduces the first tool, whereas the next chapter introduces the latter tool.

5.2 The Design Method

The design methodology presented is a hybrid method that combines graphical and analytical equations to design the damper. The geometric and electric parameters of the machine are chosen based on the desired damping coefficient and space constraints imposed on the device. The following paragraphs describe and explain the design sequence, while the next section works out a design example to demonstrate this method.

1. Determine the required damping C_d per floor and available volume V_d available in each floor for the damper installation. The procedure of determining the damping requirement of a building is covered elsewhere in the literature, for example in (Connor 2003) and is thus beyond the scope of this work.

2. Compute the required damping density

$$\hat{\gamma}_d = C_d / kV_d \tag{5.1}$$

where k is the ratio of total energy dissipation desired inside the machine. For instance, $k = 1$ correspond to whole internal dissipation (zero-load resistance), while $k = 0.5$ corre-

sponds to equal internal and external dissipation (matched load resistance).

3. Based on damping density, choose the magnet length (machine stroke) and biggest air gap thickness meeting the requirement (Figure 5.1). Increasing the air gap has the possible advantage of reducing production cost, since smaller fabrication tolerances are needed.

4. Given the air gap and magnet length, choose a magnet radius, and a range of coil wire diameters (wire gauge) that meet the required damping density (Figure 5.2).

   Select the number of coil layers and the wire diameter to maximize damping density (Figure 5.3) or to meet the machine diameter constraints (Figure 5.4). The remaining dimensional parameters are then determined. The pole shoe width is found using an approximation of the magnet flux density equation (3.16) and setting the magnet's flux density to half the remanent flux density

$$B_m = \frac{B_{rem}}{2} = \frac{B_{rem}\tau_m\tau_f}{\tau_m\tau_f + r_m^2\frac{\mu_{rec}}{\mu_0}\ln\left(\frac{r_s}{r_m}\right)} \Rightarrow \tau_f \approx \frac{r_m^2}{\tau_m}\frac{\mu_{rec}}{\mu_0}\ln\left(\frac{r_s}{r_m}\right) \tag{5.2}$$

   and the stator iron thickness by applying the no-saturation condition by solving the magnetic flux density equation (3.12) at the stator yoke

$$h_y = -r_s + \sqrt{r_s^2 + \frac{r_m^2 B_m}{0.9B_{satFe}}} \tag{5.3}$$

5. Analyze the single pole machine resulting from the above steps to verify that the desired performance was achieved. The number of machine poles needed is found using

$$p = \frac{C_d}{\widetilde{c}_d}. \tag{5.4}$$

   where $\widetilde{c}_d$ is the damping coefficient of the single pole machine. The number of poles can then be divided into various physical units such that each unit has at least 2 poles, or a single unit depending on the space constraints in the building.

5.3 A Design Example

For this example, we want to design a prototype electromagnetic damper for a hypothetical five-story building. The required damping is uniform throughout the building and equals 210 kN-s/m per floor. Table 5.1 shows the remaining damper design constraints for the sample building.

Table 5.1 Building Example Damping Design Parameters per Floor.

Parameter	Symbol (units)	Value
Required Damping	C_d (kN-s/m)	210
Available Damper Volume	V_d (m^3)	0.5
Maximum Damper Diameter	$D_e=2r_e$ (m)	0.25

If we assume an energy dissipation coefficient of $k = 0.5$, then the required damping density would be $\hat{\gamma}_d = 840\,\text{kN-m}^{-1}\text{s/m}^3$.

We use Figure 5.1 to choose a magnet length and air-gap thickness. This figure is a sample contour plot of the maximum damping density achievable as a function of magnet length (machine stroke) and air gap with no load resistance. Choosing a magnet length of $\tau_m = 25\,\text{mm}$ and an air gap of $g = 1\,\text{mm}$ sets the maximum possible damping density of the machine at 1770kN-m^{-1}s/m^3 when $k = 1$ and to 885kN-m^{-1}s/m^3 when $k = 0.5$.

Once the machine air gap and magnet length are selected, we use Figure 5.2 to find suitable values of magnet radius and coil wire diameter. This figure shows a contour plot that represents the achievable damping density for various combinations of magnet radius and coil wire for a given air-gap and magnet length. In our particular case, any magnet radius above 20mm seems to meet our requirement. Since a radius of 51mm is the practical limit on NdFeB magnets, we choose this value as our magnet radius. Choosing a magnet that provides a higher damping density than what we require allows more leeway when choosing the load resistance to increase the energy dissipation outside the device.

Finally, we use Figure 5.3 and Figure 5.4 to determine the remaining two machine parameters, coil wire diameter and number of layers. These two figures show the damping density and outside diameter, respectively, as a function the wire gauge number (wire diameter) and the number of layers in the coil under fixed magnet and air-gap dimensions.

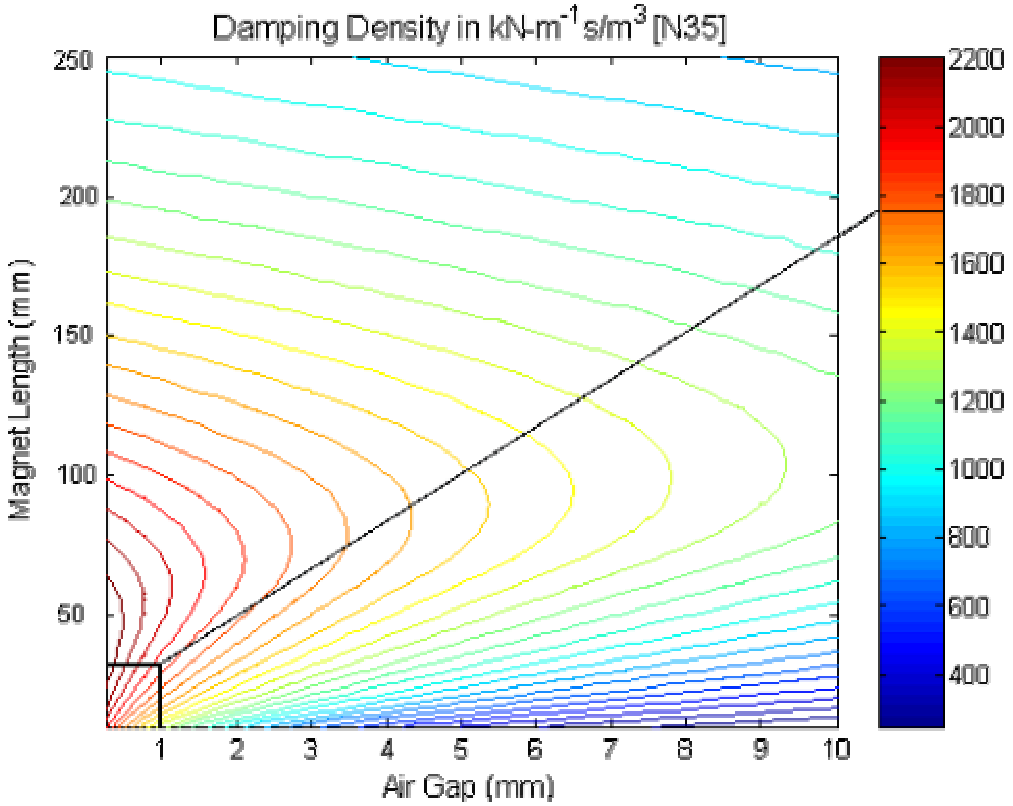

Figure 5.1 Contour Plot of Achievable Damping Density as Function of Air Gap and Magnet Length.

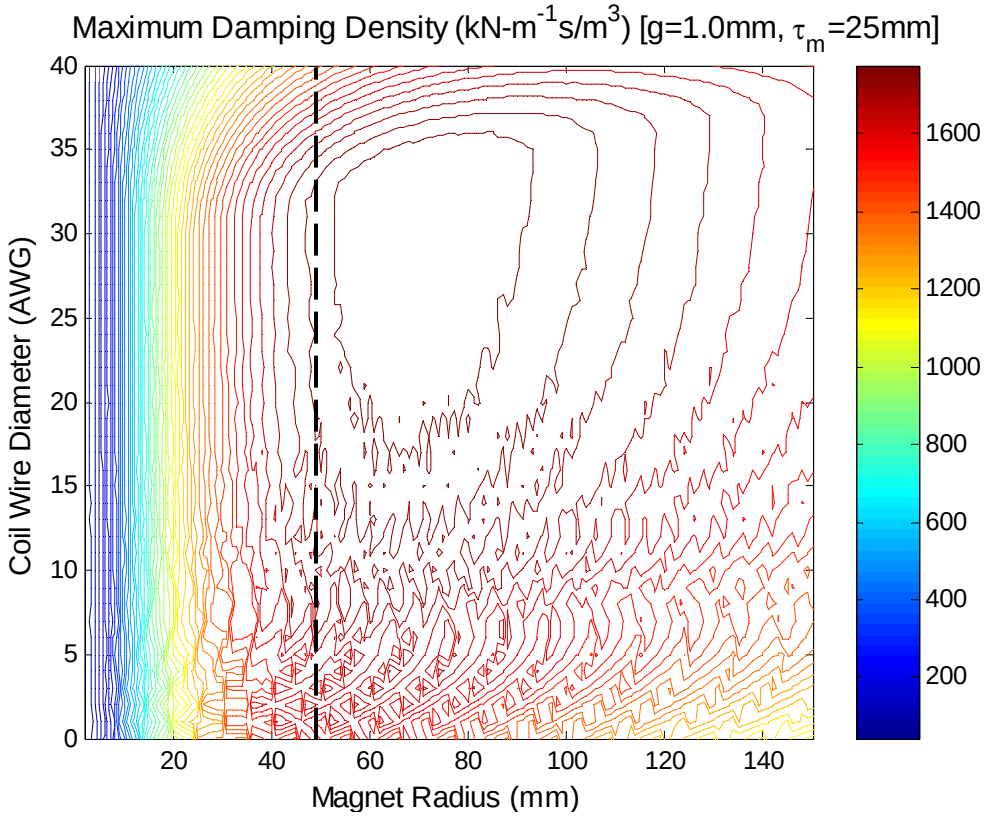

Figure 5.2 Contour Plot of Achievable Damping Density vs. Magnet Radius and Wire Diameter.

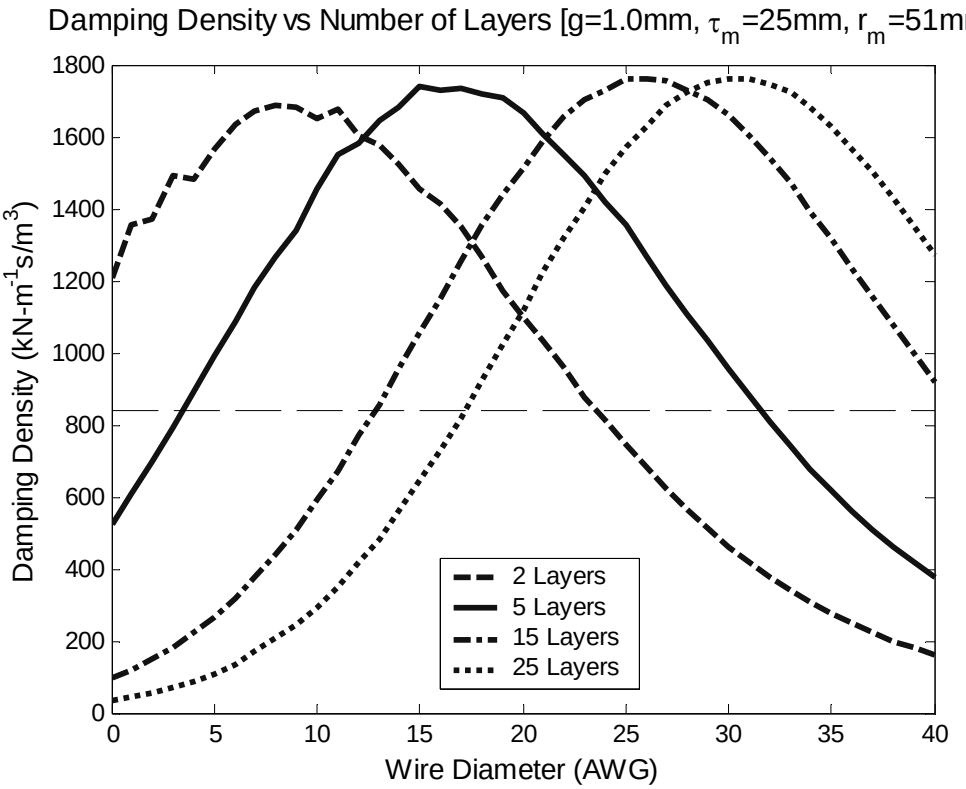

Figure 5.3 Damping Density Variation with Wire Diameter and Number of Coil Layers

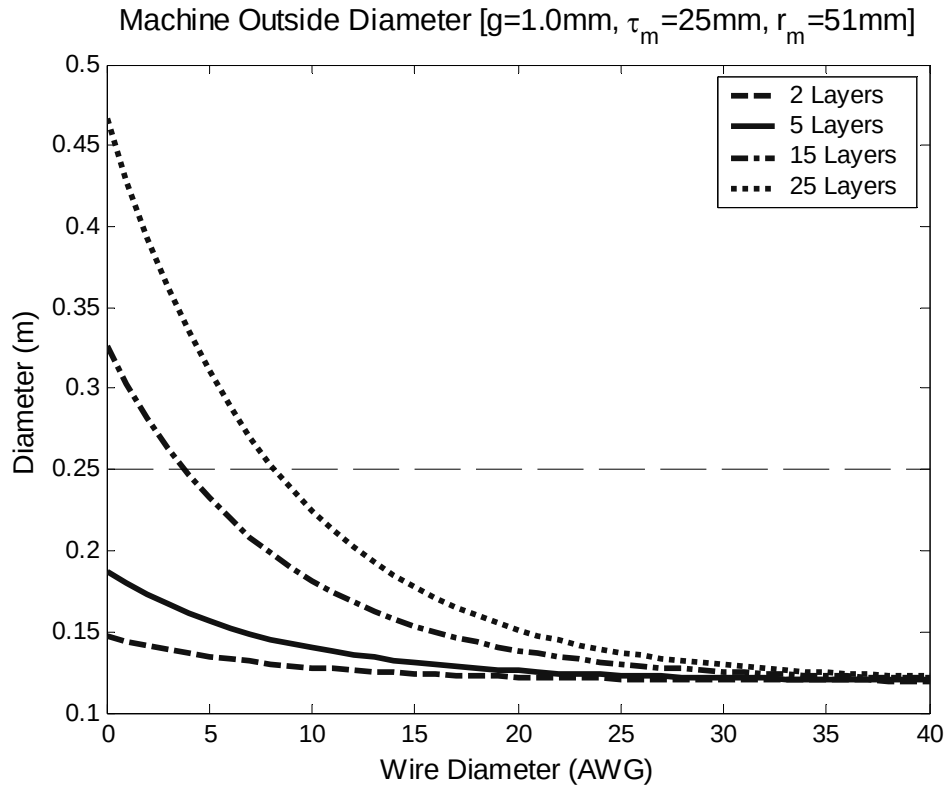

Figure 5.4 Machine Outside Diameter Variation with Wire Diameter and Number of Coil Layers.

Since we have constraints both on the outside diameter of the device (<0.25 m) and on the damping density (>840 kN-m^{-1}s/m^3), the two figures set boundaries for the values of wire gauge given a number of coil layers, or vice-versa. Because the combination of wire gauge and number of layers that satisfies the constraints is not unique, other coil parameters are considered, namely the coil inductance and resistance.

Table 5.2 shows the upper bound for wire diameter (lower AWG) given the number of layers in the coil and the corresponding coil parameters, including coil inductance and resistance. Similarly, Table 5.3 shows the same information for the lower bound wire diameter.

Table 5.2 Maximum Wire Diameter Bounds and Corresponding Parameters

Number of Layers	AWG	Diameter (mm)	Damping Density	Turns	Inductance (mH)	Resistance (Ω)
2	0	147	1209	22	4.63×10^{-2}	0.009
5	4	162	892	110	10	0.012
15	13	163	855	930	67	0.803
25	18	160	921	2650	563	7.20

Table 5.3 Minimum Wire Diameter Bounds and Corresponding Parameters.

Number of Layers	AWG	Diameter (mm)	Damping Density	Turns	Inductance (H)	Resistance (Ω)
2	23	121	875	118	0.0025	0.85
5	31	121	879	740	0.100	34.6
15	40	121	919	6330	7.287	2.35×10^3
25	40	123	1270	11450	22.734	4.28×10^3

Based on the figures and the information in the tables we select 5 coil layers with a 15 wire gauge. We choose these values because we want to have a coil inductance that is smaller than the coil resistance, and this happens with a lower number of turns.

Once we have the five governing parameters chosen, we determine the remaining machine parameters using the analysis equations presented previously. Table 5.4 shows the resulting parameters for the sample electromagnetic damper designed using the method presented in this chapter. The highlighted rows correspond to the five governing design parameters. Also, the damping and cost values are presented for the design case of $k=0.5$ (matched load) and for the limit case of $k=1$. for the sake of comparison.

Table 5.4 Sample Design Electromagnetic Damper Parameters and Results.

Group	Parameter (unit)	Value	
		k=0.5	***k=1***
Overall Dimensions per Pole	Diameter (mm)	131	
	Length (mm)	55.2	
	Volume (m^3)	$7.43x10^{-4}$	
Air-Gap	Thickness (mm)	1.0	
Coil Parameters	Layers	5	
	Wire Diameter (AWG)	15	
	Turns	195	
	Coil Height (mm)	6.5	
Magnet	Length (mm)	25	
	Radius (mm)	51	
Stator Pole Shoes	Thickness (mm)	7	
	Width (mm)	15.1	
Electrical	Circuit Resistance (Ω)	0.422	0.231
	Inductance (mH)	5.1	
	Machine Constant (N/A)	17.35	
Damping per Pole	(kN-s/m)	0.652	1.30
Damping Density	($kN\text{-}m^{-1}s/m^3$)	871.5	1743
Cost	Per Pole	$103.66	
	Damping	$159.10	$79.55
Resulting Machine	Required Poles	322	161
	Required Volume (m^3)	0.24	0.12
	Effective Damping (kN-s/m)	0.242	209.8
	Machine Cost	$33,382	$16,691

5.4 Summary

The current chapter developed the first of two tools needed to apply the electromagnetic damper to a building system design. The method presented produces the damper geometric parameters based on the desired damping density for the device using graphs and analytical equations.

The method works by selecting five governing parameters such that the device achieves the desired damping performance. These parameters are the magnet radius and length, the air-gap thickness, the coil wire diameter, and the number of layer in the coil. The selection is performed sequentially using graphs that plot the maximum achievable damping density as a function of these parameters. Once the initial parameters are chosen, the remaining damper parameters are then found using the analytical damper equations derived in previous chapters.

The next chapter presents how to incorporate the electromagnetic damper model into the building analysis methods. This provides the designer with the ability to analyze the dynamic response of a building outfitted with electromagnetic dampers.

Chapter 6
Analysis of Buildings with Electromagnetic Dampers

6.1 Introduction

The previous chapter introduced the method to design an electromagnetic damper given a desired damping, whereas the mathematical framework introduced in the following sections allows the designer to analyze the dynamic response of a building with the given electromagnetic damper design. This analysis framework and the design methodology are two basic tools that allow a designer to incorporate electromagnetic dampers into the conceptual design of a building structure.

Section §6.2 introduces the basic differential equations that describe the motional behavior of a building using electromagnetic dampers. These equations are obtained by combining the building force equilibrium equations and the damper constitutive differential equation when the building is modeled as a multi-degree-of-freedom lumped mass system. The solution to this differential equations is performed following to approaches: modal analysis and a state-space system models. Section §6.3 develops the system solution for low-frequency sinusoidal steady-state excitation by incorporating the damper low-frequency model into the modal analysis equations of the building, while, section §6.4 merges the damper two-port model representation with the state-space model of the building for time-domain transient analysis of the response.

6.2 Modeling of Buildings with EM Dampers

In a lumped parameter model, a structure is conceived as a discrete system composed of a finite number of masses interconnected by mass-less springs and dampers (Cheng 2001). Figure 6.1 shows an n-story building frame with forces at each floor and ground movement, and its corresponding lumped parameter model. The following assumptions are made (Connor 2003)

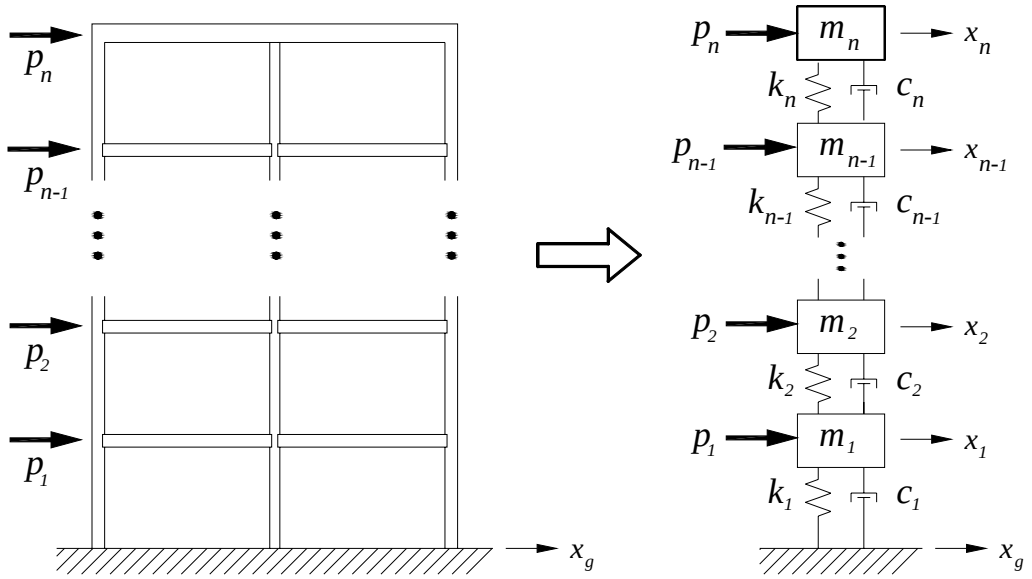

Figure 6.1 Modeling an N-Story Building as an N-Degree-of-Freedom Lumped Parameter System.

- The masses of the floors and columns are lumped at the floor levels
- The columns are regarded as mass-less springs
- The axial deformation of the columns is small.
- There is no rotation of the members.
- The floors experience only lateral displacement.
- Dampers represent the only energy dissipation mechanisms in the structure.

Real structures possess an infinite number of degrees of freedom, each with its own dynamic response characteristic. The analysis of a structure as a continuum system usually results in complex and computationally expensive mathematic models based on coupled partial differential equations. It is preferred to simplify the model by describing the structure using lumped parameters that reduce the number of degrees of freedom, and result in coupled ordinary differential equations of motion. This representation is a compromise between the accuracy required and the complexity of the mathematical model (Beards 1996).

Each lumped mass is governed by the following force equilibrium equation

$$m_i \ddot{x}_i = p_i - m_i \ddot{x}_g - F_{d,i} + F_{d,i+1} - F_{s,i} + F_{s,i+1} \tag{6.1}$$

where $F_{d,i}$ and $F_{s,i}$ are the damping and spring forces of the i^{th} mass, respectively.

Restricting the system to idealized linear dampers and springs, with force equations of the form

$$\begin{aligned} F_{d,i} &= c_i\left(\dot{x}_i - \dot{x}_{i-1}\right) \\ F_{s,i} &= k_i\left(x_i - x_{i-1}\right) \end{aligned} \tag{6.2}$$

then the *n* system equilibrium equations can be expressed in terms of the displacement variables and component coefficients as

$$m_i\ddot{x}_i + (c_i + c_{i+1})\dot{x}_i - c_i\dot{x}_{i-1} - c_{i+1}\dot{x}_{i+1} + (k_i + k_{i+1})x_i - k_i x_{i-1} - k_{i+1}x_{i+1} = p_i \tag{6.3}$$

where the ground acceleration term $-m_i\ddot{x}_g$ is bundled into the driving force p_i.

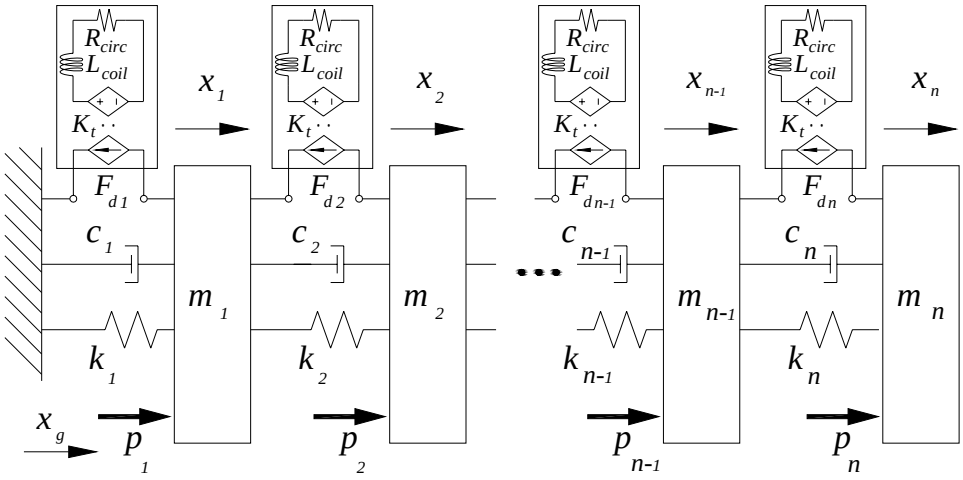

Figure 6.2 N-Degree-of-Freedom Model of Structure with EM Dampers between each Floor.

The introduction of electromagnetic dampers between floors in the structure, as shown in Figure 6.2, produces the following equilibrium equations for each mass

$$m_i\ddot{x}_i + (c_i + c_{i+1})\dot{x}_i - c_i\dot{x}_{i-1} - c_{i+1}\dot{x}_{i+1} + (k_i + k_{i+1})x_i - k_i x_{i-1} - k_{i+1}x_{i+1} + F_{d,i} - F_{d,i+1} = p_i \tag{6.4}$$

Here the forces $F_{d,i}$ of the i^{th} electromagnetic dampers are governed by the first-order differential force-velocity relationship presented below

$$L_{coil}\frac{dF_{d,i}}{dt} + R_{circ,i}F_{d,i} = K_{t,i}^2\left(\dot{x}_i - \dot{x}_{i-1}\right) \tag{6.5}$$

Combining the damper's electrical equation (6.5) with equation (6.4) increments the order of the equations of motion for each mass to which the damper is attached to a fourth-order differential

equation. For the particular case where all the electromagnetic dampers used in the structure have the same device parameters, the equation of motion for each mass simplifies to a third order equation

$$\begin{aligned} & m_i\dddot{x}_i + \left(c_i + c_{i+1} + \frac{m_i}{\tau_d}\right)\ddot{x}_i - c_i\ddot{x}_{i-1} - c_{i+1}\ddot{x}_{i+1} + \left(k_i + k_{i+1} + \frac{c_i + c_{i+1}}{\tau_d}\right)\dot{x}_i - \left(k_i + \frac{c_i}{\tau_d}\right)\dot{x}_{i-1} \\ & - \left(k_{i+1} + \frac{c_{i+1}}{\tau_d}\right)\dot{x}_{i+1} + \left(\frac{2K_t^2}{L_{coil}} + \frac{k_i + k_{i+1}}{\tau_d}\right)x_i - \left(\frac{K_t^2}{L_{coil}} + \frac{k_i}{\tau_d}\right)x_{i-1} - \left(\frac{K_t^2}{L_{coil}} + \frac{k_{i+1}}{\tau_d}\right)x_{i+1} = \frac{p_i}{\tau_d} + \dot{p}_i \end{aligned} \tag{6.6}$$

where $\tau_d = L_{coil}/R_{circ}$ is the damper electrical time constant.

In practice, the direct solution of equation (6.6) is avoided because of its complexity and its requirement of knowledge of both the excitation signal p_i and its time derivative $\dot{p}_i$. The system equations can be simplified following the type of analysis performed, and using approximations based on the period of the excitation signal relative to the damper's time constant.

Two methods for solving the structural system equations resulting from the utilization of electromagnetic dampers are presented in the following sections together with the system simplifications, followed by examples that illustrate these methods.

6.3 Low Frequency Steady-State Solution

When the electromagnetic damper is subjected to a steady-state sinusoidal velocity excitation, its constitutive force-velocity relationship is reduced to a scalar equation relating the magnitudes of the damper force and velocity, and a phase shift or time delay between the force and damper velocity. This relationship can be expressed as

$$\begin{aligned} |F_d| &= c_d|v| \\ \angle F_d &= \angle v + \phi_d \end{aligned} \tag{6.7}$$

where the operators $|\ |$ and $\angle$ are the magnitude and angle, respectively. The damping coefficient c_d and phase shift ϕ_d in the above equation are given by

$$c_d = \frac{K_t^2}{\sqrt{(R_{circ})^2 + (\omega L_{coil})^2}} \tag{6.8}$$

$$\phi_d = \tan^{-1}\left(-\frac{\omega L_{coil}}{R_{circ}}\right) \tag{6.9}$$

Equations (6.8) and (6.9) are the frequency response of the damper, and they represent the behavior of the damper as the frequency of the excitation varies.

Figure 6.3 shows the normalized frequency response of the electromagnetic damper. The frequency axis is expressed in terms of the damper cut-off frequency $\omega_c = 1/\tau_d = R_{circ}/L_{coil}$, while the magnitude response is normalized to the maximum damping coefficient, $c_{d,\max} = K_t^2/R_{circ}$.

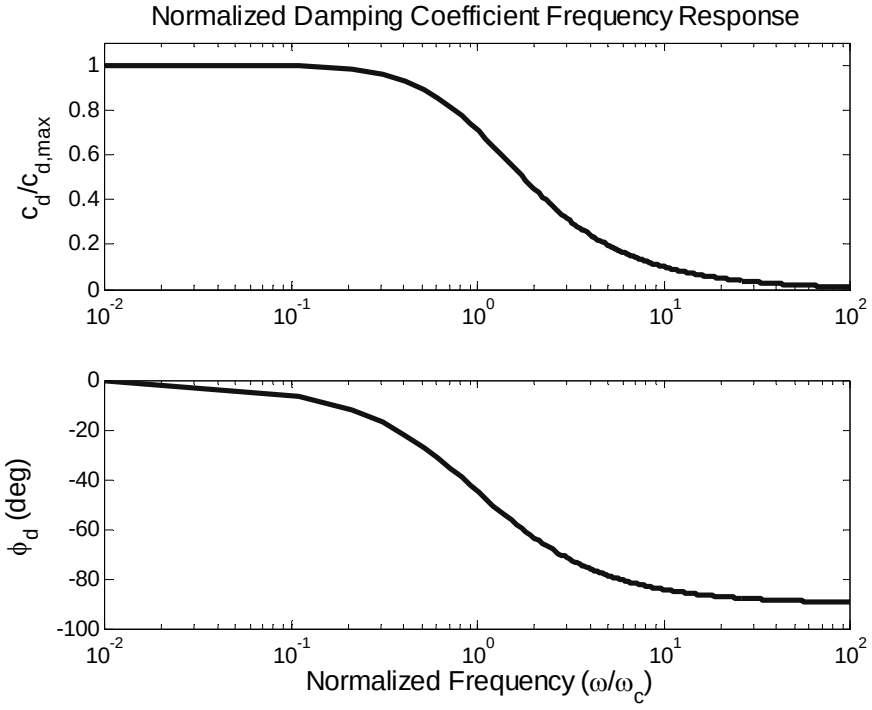

Figure 6.3 Electromagnetic Damper Normalized Frequency Response.

The frequency response of the damper corresponds to that of a low-pass filter. It can be seen from the figure that at low frequencies satisfying $\omega \leq 0.1\omega_c$, that is frequencies less than or equal to approximately one tenth the cut-off frequency, the damper response approximates that of an ideal damper with a damping coefficient $c_{d,\max}$, and a negligible phase shift.

Under the assumption of low frequency excitation, a valid assumption given the nature of the

disturbances normally affecting building, the system model reverts to *n* second-order differential equations (6.3) with frequency dependent damping coefficients given by

$$\hat{c}_i = c_i + \frac{K_{t,i}^2}{\sqrt{R_{circ,i}^2 + (\omega L_{coil})^2}} \approx c_i + \frac{K_{t,i}^2}{R_{circ,i}} \tag{6.10}$$

The *n* equations of motion can be arranged into matrix form as

$$\mathbf{M}\ddot{\mathbf{x}} + \hat{\mathbf{C}}\dot{\mathbf{x}} + \mathbf{K}\mathbf{x} = \mathbf{P} \tag{6.11}$$

where the matrices $\mathbf{M}$, $\hat{\mathbf{C}}$ and $\mathbf{K}$ are known as the mass, the damping and the stiffness matrices, respectively of an *n*-degree-of-freedom (*n*-dof) system. The mass, damping and stiffness matrices are presented below for the case of a system with electromagnetic dampers between floors under low-frequency sinusoidal excitation.

$$\mathbf{M} = \begin{bmatrix} m_1 & & 0 \\ & \ddots & \\ 0 & & m_n \end{bmatrix} \tag{6.12}$$

$$\hat{\mathbf{C}} = \begin{bmatrix} \hat{c}_1 + \hat{c}_2 & -\hat{c}_2 & 0 & \cdots & 0 & 0 & 0 \\ -\hat{c}_2 & \hat{c}_2 + \hat{c}_3 & -\hat{c}_3 & \cdots & 0 & 0 & 0 \\ & \ddots & \ddots & \ddots & & & \\ \vdots & & -\hat{c}_i & \hat{c}_i + \hat{c}_{i+1} & -\hat{c}_{i+1} & & \vdots \\ & & & \ddots & \ddots & \ddots & \\ 0 & 0 & 0 & \cdots & -\hat{c}_{n-1} & \hat{c}_{n-1} + \hat{c}_n & -\hat{c}_n \\ 0 & 0 & 0 & \cdots & 0 & -\hat{c}_n & \hat{c}_n \end{bmatrix} \tag{6.13}$$

$$\mathbf{K} = \begin{bmatrix} k_1 + k_2 & -k_2 & 0 & \cdots & 0 & 0 & 0 \\ -k_2 & k_2 + k_3 & -k_3 & \cdots & 0 & 0 & 0 \\ & \ddots & \ddots & \ddots & & & \\ \vdots & & -k_i & k_i + k_{i+1} & -k_{i+1} & & \vdots \\ & & & \ddots & \ddots & \ddots & \\ 0 & 0 & 0 & \cdots & -k_{n-1} & k_{n-1} + k_n & -k_n \\ 0 & 0 & 0 & \cdots & 0 & -k_n & k_n \end{bmatrix} \tag{6.14}$$

where the damping coefficients $\hat{c}_i$ are given by equation (6.10).

The solution to the matrix equation (6.11) under a sinusoidal excitation $\mathbf{P}$ can then be found using modal analysis. Modal analysis is presented extensively in the structural dynamics literature, such as Beards (1996), Buchholdt (1997) or Cheng (2001), and a brief review is presented in Appendix B.

6.4 Transient Analysis and State-Space Solution

The sinusoidal approximation of the previous section is useful when the excitation signal can be represented using a series of sinusoidal signals or as a power or frequency spectra, such as in the case of wind and earthquakes. However, the solution is given in terms of maximum displacement amplitudes at steady-state, and no transient information is provided in the solution.

A common way to model dynamic systems that facilitates the derivation of transient information is by means of state-space systems equations. In a state-space representation, the system under study is modeled by a set of first order differential equations in the form

$$\dot{\mathbf{z}} = \mathbf{A}\mathbf{z} + \mathbf{B}\mathbf{u} \tag{6.15}$$

where $\mathbf{z} = \begin{bmatrix} z_1 & z_2 & \cdots & z_k \end{bmatrix}^T$ is the system state vector, $\mathbf{u} = \begin{bmatrix} u_1 & u_2 & \cdots & u_m \end{bmatrix}^T$ is the input vector, and the matrices $\mathbf{A}$ and $\mathbf{B}$ are constant matrices of dimension $k \times k$ and $k \times m$, respectively. This mathematical model can then be solved using numerical or analytical methods in the time domain; or using Fourier or Laplace transform methods in the frequency domain. A basic review of time-domain state-space methods is presented in appendix B.

Using a state-space description to represent the building system depicted in Figure 6.2 simplifies its analysis by solving a set of first-order equations like (6.15) instead of fourth- or third-order equations like (6.6).

To express the system in state-space form, the governing equilibrium (6.4) and damper equations (6.5) for each mass are rearranged such that highest derivative term on each function is expressed as a function of the lower order terms,

$$\begin{aligned}\ddot{x}_i &= \frac{k_i}{m_i}x_{i-1} - \frac{k_i + k_{i+1}}{m_i}x_i + \frac{k_{i+1}}{m_i}x_{i+1} + \frac{c_i}{m_i}\dot{x}_{i-1} - \frac{c_i + c_{i+1}}{m_i}\dot{x}_i + \frac{c_{i+1}}{m_i}\dot{x}_{i+1} - \frac{F_{d,i}}{m_i} + \frac{F_{d,i+1}}{m_i} + \frac{p_i}{m_i} - \ddot{x}_g \\ \dot{F}_{d,i} &= -\frac{K_{t,i}^2}{L_{coil.i}}x_{i-1} + \frac{K_{t,i}^2}{L_{coil,i}}\dot{x}_i - \frac{R_{circ,i}}{L_{coil,i}}F_{d,i}\end{aligned} \tag{6.16}$$

If we choose the state variables to be the position, velocity and electromagnetic damper force at each mass

$$\begin{aligned} z_i &= x_i \\ z_{i+n} &= \dot{x}_i \\ z_{i+2n} &= F_{d,i} \end{aligned} \tag{6.17}$$

the corresponding state equations are given by

$$\begin{aligned}\dot{z}_i &= z_{i+n} \\ \dot{z}_{i+n} &= \frac{k_i}{m_i}z_{i-1} - \frac{k_i + k_{i+1}}{m_i}z_i + \frac{k_{i+1}}{m_i}z_{i+1} + \frac{c_i}{m_i}z_{i+n-1} - \frac{c_i + c_{i+1}}{m_i}z_{i+n} \cdots \\ &\quad + \frac{c_{i+1}}{m_i}z_{i+n+1} - \frac{z_{i+2n}}{m_i} + \frac{z_{i+2n-1}}{m_i} + \frac{p_i}{m_i} - \ddot{x}_g \\ \dot{z}_{i+2n} &= -\frac{K_t^2}{L_{coil}}z_{i+n-1} + \frac{K_t^2}{L_{coil}}z_{i+n} - \frac{R_{circ}}{L_{coil}}z_{i+2n}\end{aligned} \tag{6.18}$$

Grouping the n sets of state equations defined by (6.18) into matrix form and back substituting the state variable definitions (6.17) the system state space model for an n-degree-of-freedom structure with inter-story electromagnetic dampers

$$\begin{bmatrix} \dot{\mathbf{x}} \\ \ddot{\mathbf{x}} \\ \dot{\mathbf{F}}_\mathbf{d} \end{bmatrix} = \begin{bmatrix} \mathbf{0} & \mathbf{I} & \mathbf{0} \\ -\mathbf{M}^{-1}\mathbf{K} & -\mathbf{M}^{-1}\mathbf{C} & \mathbf{M}^{-1}\mathbf{J}^T \\ \mathbf{0} & -\mathbf{L}^{-1}\mathbf{K_T}^T\mathbf{K_T}\mathbf{J} & -\mathbf{L}^{-1}\mathbf{R} \end{bmatrix} \begin{bmatrix} \mathbf{x} \\ \dot{\mathbf{x}} \\ \mathbf{F}_\mathbf{d} \end{bmatrix} + \begin{bmatrix} \mathbf{0} & \mathbf{0} \\ \mathbf{M}^{-1} & -\mathbf{1} \\ \mathbf{0} & \mathbf{0} \end{bmatrix} \begin{bmatrix} \mathbf{P} \\ \ddot{x}_g \end{bmatrix} \tag{6.19}$$

The state matrix $\mathbf{A}$ in the above equation is of size $3n \times 3n$ and is made up of the structure's matrices $\mathbf{M}$, $\mathbf{C}$ and $\mathbf{K}$; the damper's matrices $\mathbf{L}$, $\mathbf{R}$ and $\mathbf{K_T}$; and the *Jordan* matrix $\mathbf{J}$. The size of the input matrix $\mathbf{B}$ is $3n \times (n+1)$ and is composed of the inverse of the mass matrix affecting the driving force vector $\mathbf{P}$ and a vector of zeros and ones affecting ground acceleration signal $\ddot{x}_g$.

The mass, damping and stiffness matrices were defined previously in equations (6.12) to (6.14). The damper matrices, corresponding to the last subsystem row in equation (6.19), are the inductance, resistance and damper machine constant matrices, respectively. All are diagonal matrices containing the parameters of the electromagnetic dampers between each floor, and are given below,

$$\mathbf{L} = \begin{bmatrix} L_{coil,1} & & 0 \\ & \ddots & \\ 0 & & L_{coil,n} \end{bmatrix} \tag{6.20}$$

$$\mathbf{R} = \begin{bmatrix} R_{circ,1} & & 0 \\ & \ddots & \\ 0 & & R_{circ,n} \end{bmatrix} \tag{6.21}$$

$$\mathbf{K_T} = \begin{bmatrix} K_{t,1} & & 0 \\ & \ddots & \\ 0 & & K_{t,n} \end{bmatrix} \tag{6.22}$$

The *Jordan* matrix defined as

$$\mathbf{J} = \begin{bmatrix} -1 & 0 & & 0 \\ 1 & -1 & \ddots & \\ & \ddots & \ddots & 0 \\ 0 & & 1 & -1 \end{bmatrix} \tag{6.23}$$

The matrix equation (6.19) defines the state-space model of an *n*-degree-of-freedom structure where the damping is provided using electromagnetic and linear dampers connected between floors. The linear dampers model the inherent damping in the structure while the electromagnetic dampers provide manufactured energy dissipation.

6.5 Summary

This chapter introduced the mathematical framework that allows the dynamic response analysis of buildings with electromagnetic damping. Two methods were developed, one based on a sinu-

soidal steady-state model (6.11) of the building and electromagnetic damper and another one based on a state-space system model representation (6.19).

The first approach applies when the driving forces can be represented by a sum of sinusoidal terms or power spectra, and only the steady-state response of the system is of interest. Given the low frequency and the sinusoidal nature of the disturbances of interest in structural analysis, a linear damper with frequency dependent coefficient approximates the electromagnetic damper in this model. The response of the system is then obtained using nodal analysis methods.

The second model developed combines the equations of motion of the structure with the electrical equations of the electromagnetic dampers into a state-space system representation. This model can be used when the transient response of the system to time-varying disturbances or to non-zero initial conditions is investigated. The solution in the time domain of the system equation is normally obtained with numerical methods and requires a time-description of the disturbance, rather than the frequency description used with the sinusoidal model.

This analysis framework, together with the design method presented in Chapter 5, is part of the tools that would allow designers to incorporate this new type of structural dampers into their building designs. The following chapter presents the experimental validations of the models and methods developed up to this point in this thesis.

Chapter 7
Experimental Characterization of the Electro-magnetic Damper

7.1 Introduction

Two experiments were devised to characterize a scale prototype electromagnetic damper, and to validate the theory developed in the previous chapters.

In the first experiment (§7.3), a constant force is applied to the damper and its rate of displacement measured and compared to the displacements computed using the mathematical model of the set-up; in the second experiment (§7.4), a prescribed oscillatory displacement is applied to the device and its reaction force measured to obtain the experimental force-velocity curves.

The following section (§7.2) describes the prototype damper and compares it to the model of the theoretical machine with the same dimensions and materials. Subsequent sections then present the experimental set-ups and their mathematical models, together with a discussion of the simulation and experimental results.

7.2 Scale Prototype Description

A tubular non-commutated moving magnet DC linear motor from Baldor Motors and Drives™, model number LMNM2-1F5-1F1, was purchased to perform as the electromagnetic damper in these work's experiments. The motor datasheets supplied by the manufacturer are presented in Appendix C. The device quoted specifications, in SI units, are summarized for convenience in Table 7.1.

A picture of the prototype damper is shown in Figure 7.1, and a dimensioned drawing (as built) in Figure 7.2. The dimensions in the drawing are in millimeters, and the drawing shows a view of the machine where only the stator and end supports are sectioned for clarity.

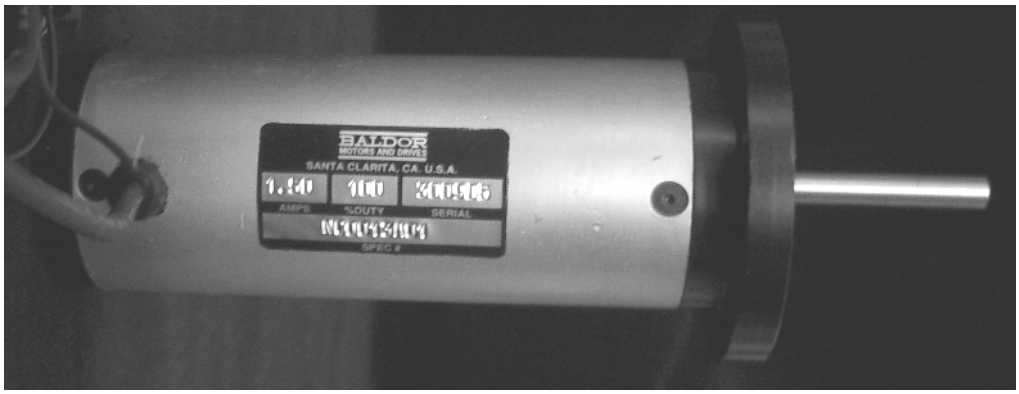

Figure 7.1 Linear Motor from Baldor Motors and Drives, Model LMNM2-1F5-1F1.

Table 7.1 Baldor™ Linear Motor Parameters.

Parameter	Symbol	Value
Back EMF Constant	$K_{t(e)}$	7.874 Vs/m
Force Constant	$K_{t(f)}$	7.918 N/A
Coil Resistance	R_{coil}	3.89 □
Coil Inductance	L_{coil}	2.03 mH
Number of Poles	p	2
Motor Length	$2h_w$	108 mm
Motor Diameter	$2r_e$	38 mm
Stroke Length	τ_m	25.4 mm
Mover Mass	m_m	230 g

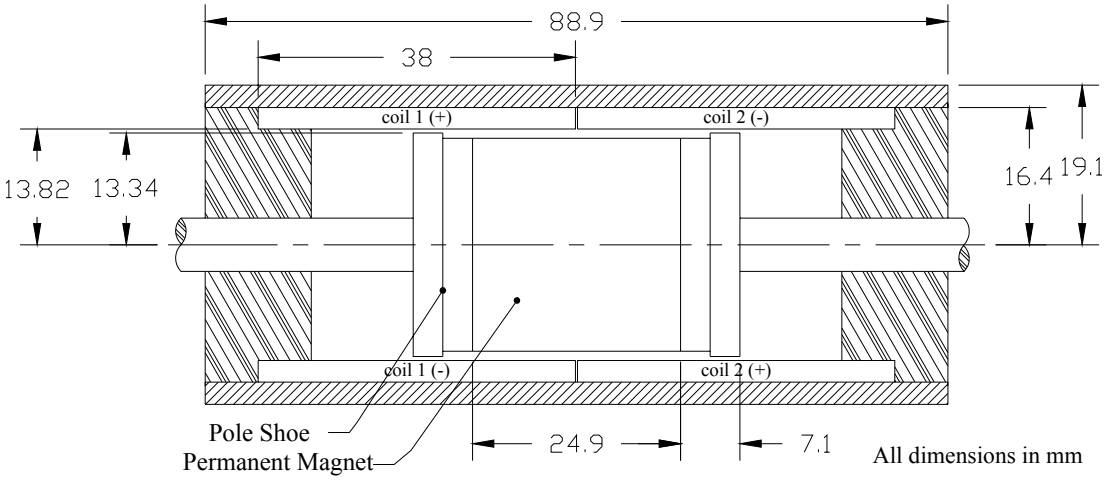

Figure 7.2 Baldor™ Linear Motor Dimensioned Drawing.

When the experimental damper machine is compared to the theoretical electromagnetic damper described previously in this thesis, the following is observed:

- The coils extend beyond the allowed travel of the mover. A linear inductance independent of mover position results from this arrangement.
- The pole shoes are composed of two cylinders of equal width but slightly different diameter, approximately 1.3 mm. The mathematical model uses the diameter of the largest shoe and the combined thickness of both cylinders as the dimensions for the pole shoes.
- The diameter of the permanent magnet equals the diameter of the smaller pole shoes cylinder. In the theoretical model the magnet diameter is equal to the larger cylinder diameter.

The dimensions obtained from the prototype device were used to compute the theoretical electromagnetic damper parameters using the model equations from Chapter 3. Given that the coil was not disassembled due to practical reasons, the number of turns per coil and the wire diameter were assumed as 270 and 24AWG, respectively. Table 7.2 presents the numerical comparison between the actual damper values and the theoretical model damper values of machine constant, coil resistance and coil inductance.

Table 7.2 Mathematical Model and Prototype Electromagnetic Damper Comparison.

Parameters	Symbol (Units)	Mathematical	Prototype	Difference
Machine Constant	K_t (N/A)	7.582	7.896	-3.98%
Coil Resistance	R_{coi}l (Ω)	4.43	3.9	13.6%
Coil Inductance	L_{coi}l (mH)	1.72	2.03	-15.3%

The values in the above table verify that the mathematical model derived in Chapter 3 is a good representation of the damper machine, as the theoretical values are within 15% of the measured values.

The mathematical models of the experiments described in the following sections are obtained following the analytical methods presented in the previous chapter. These methods are based on differential force-velocity relationship of the electromagnetic damper (3.27), which is repeated here for convenience,

$$L_{coil}\frac{dF_d}{dt} + (R_{coil} + R_{load})F_d = K_t^2 v \tag{3.27}$$

This equation will be used with the machine values provided by the manufacturer while simulating the experimental systems responses.

7.3 Constant Force Response

7.3.1 Experiment Description

This experiment studies the electromagnetic damper displacement when a constant force is applied to it. The constant force is provided by a mass under gravity. The mass is attached to the moving element of the damper and released from a constant height. As the mass drops, the damper develops a force opposing the fall.

The experimental setup, as shown in Figure 7.3, consists of a weight support attached to the damper shaft, a base to keep the damper vertical and a latch-and-release mechanism.

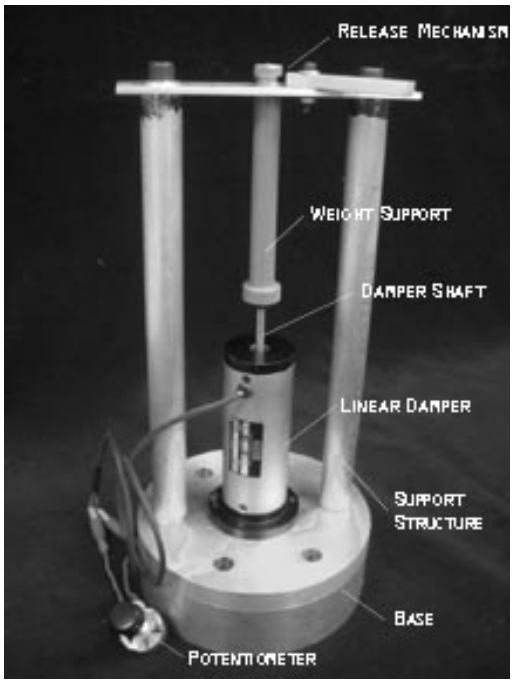

Figure 7.3 Damped Mass Drop Experimental Setup.

The mass drops from a height of 24.5mm. The force applied to the damper is varied by adding weights (3/8" nuts) to the weight support. A potentiometer is connected to the leads of the damper to vary electric circuit resistance, and therefore the damping coefficient of the device.

Drops from the specified height are performed for each one of the circuit resistance values presented in Table 7.3 using all four mover-masses shown. The table also shows the expected damping coefficient and applied force corresponding to the circuit resistances and weights.

Table 7.3 Damped Mass Drop Experimental Parameters.

Total Resistance R_{circ} (Ω)		Damper Coefficient (N-s/m)	Total Mover Mass (g)		Applied Force (N)
R_0	Open Circuit	0	m_0	272.5	2.67
R_1	14.2	4.39	m_1	336.3	3.30
R_2	9.5	6.57	m_2	400.1	3.92
R_3	4.4	14.20	m_3	463.9	4.55

A high-speed digital video camera with a macro lens records the drop of the mover after the weight support is released from the latch mechanism. The video is recorded at a rate of 500 frames per second with a resolution of 320x280 pixels and a field view of 37x32mm. Figure 7.4 shows a sequence of three frame shots extracted from one of the videos created. The video frames are then analyzed using the software provided with the camera system to extract time and position data.

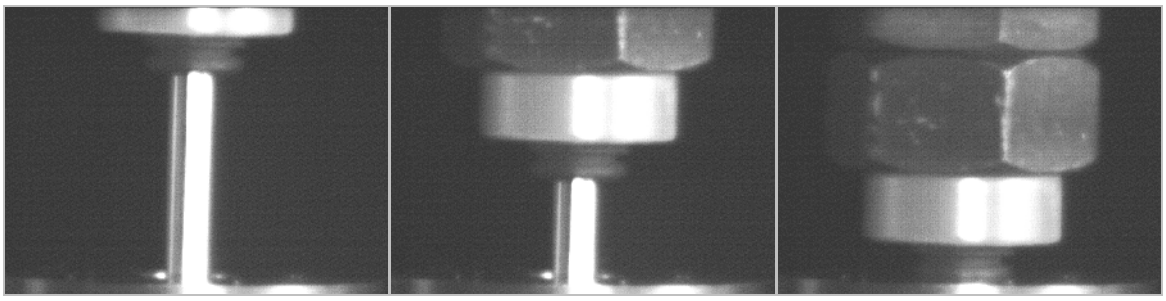

Figure 7.4 Sample Picture Frames extracted from High Speed Digital Video.

The experimental displacement profiles are presented in the following sub-sections and compared to the theoretical displacement profiles obtained from the system model derived in the subsequent paragraphs.

7.3.2 System Model

The experimental setup is a single degree of freedom mass-spring-damper system under constant force. Figure 7.5 shows the body diagram of the experimental system. In the diagram, the two-port device represents the electromagnetic damper while an ideal damper (c_f) represents mechanical losses, such as friction, in the system. A spring ($k_s=0$) is shown in the diagram for the sake of generality, even though there are no actual springs in the experimental setup (with the possible exception of rubber grommets in the damper shaft that are used as displacement stops).

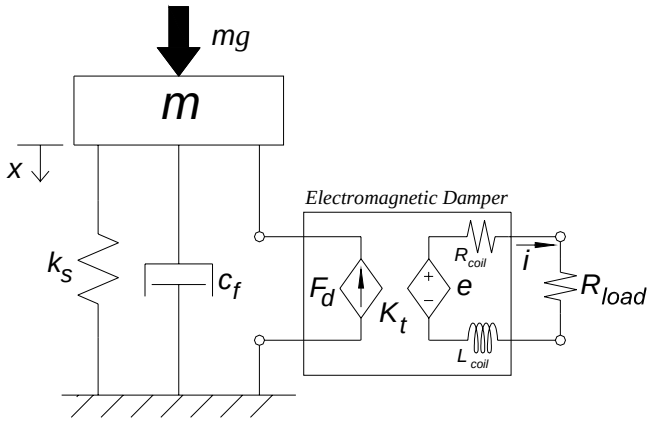

Figure 7.5 Damped Mass Drop Experiment Body Diagram

From the diagram in Figure 7.5 the governing equation of the system is derived as,

$$m\ddot{x} = -c_f \dot{x} - k_s x - F_d + mg \tag{7.1}$$

where $\dot{x} = v$, and the damper force F_d is governed by equation (7.1). Rearranging the system into a state-space system following the methodology introduced in §6.4, using the electromagnetic damper force (F_d), position (x) and velocity ($\dot{x}$) as the state variables and the gravity g as the input to the system, gives

$$\begin{bmatrix} \dot{x} \\ \ddot{x} \\ \dot{F}_d \end{bmatrix} = \begin{bmatrix} 0 & 1 & 0 \\ -\frac{k_s}{m} & -\frac{c_f}{m} & -\frac{1}{m} \\ 0 & \frac{K_t^2}{L_{coil}} & -\frac{R_{circ}}{L_{coil}} \end{bmatrix} \begin{bmatrix} x \\ \dot{x} \\ F_d \end{bmatrix} + \begin{bmatrix} 0 \\ 1 \\ 0 \end{bmatrix} g \tag{7.2}$$

In the above equation, $R_{circ}=R_{coil}+R_{load}$, and $k_s=0$.

7.3.3 Simulation Results

The system described by equation (7.2) is simulated using Matlab® for the different values of circuit resistance and masses presented in Table 7.3. The simulations are run until the displacement equals the prescribed drop height of 24.5mm. Appendix E presents the simulation scripts.

The value of the parasitic damping coefficient used during the simulations is $c_f=8.2Ns/m$. This

value was estimated from the experimental data following the method described in Appendix D. Since the experimental device produces both the parasitic damping and the electromagnetic damping, the actual damper force acting on the mass is

$$F_{damper} = F_d + c_f v \tag{7.3}$$

This force is used to compute the effective damping coefficient of the device.

In the simulation, when the weight reaches the end of its displacement, its movement stops abruptly, however, during the actual experiment the mass oscillates before resting at the end of its displacement run because of the spring effect provided by the rubber stops. These oscillations are ignored during the Matlab® simulation, but are visible on the experimental data.

The time needed for the weight to reach the end of its displacement is shown in Table 7.4 for the various combinations of mass and circuit resistance used in the simulations. The simulated displacement profiles for the smallest mover mass and the four circuit resistances tested are shown in Figure 7.6. The maximum velocities developed, which occurred at the end of its displacement, by the different masses under the different resistance values are presented in Table 7.5 while sample velocity profiles are shown in Figure 7.7.

Table 7.4 Simulated Time (s) to End of Travel.

		Circuit Resistance			
		R_0	**R_1**	**R_2**	**R_3**
Drop Mass	**m_0**	0.106	0.136	0.152	0.216
	m_1	0.096	0.118	0.130	0.180
	m_2	0.092	0.108	0.118	0.156
	m_3	0.088	0.102	0.108	0.140

Table 7.5 Simulated Maximum Velocity (m/s).

		Circuit Resistance			
		R_0	**R_1**	**R_2**	**R_3**
Drop Mass	**m_0**	0.31	0.21	0.18	0.12
	m_1	0.36	0.26	0.22	0.15
	m_2	0.40	0.30	0.26	0.18
	m_3	0.44	0.34	0.30	0.20

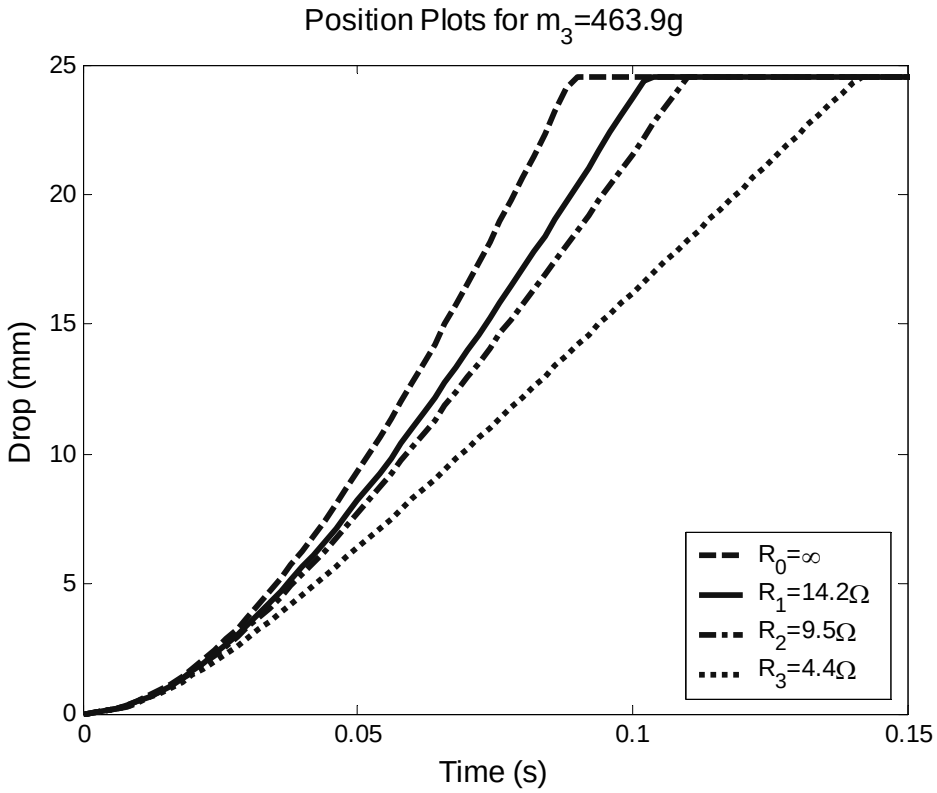

Figure 7.6 Sample Position Curves for Various Circuit Resistance Values.

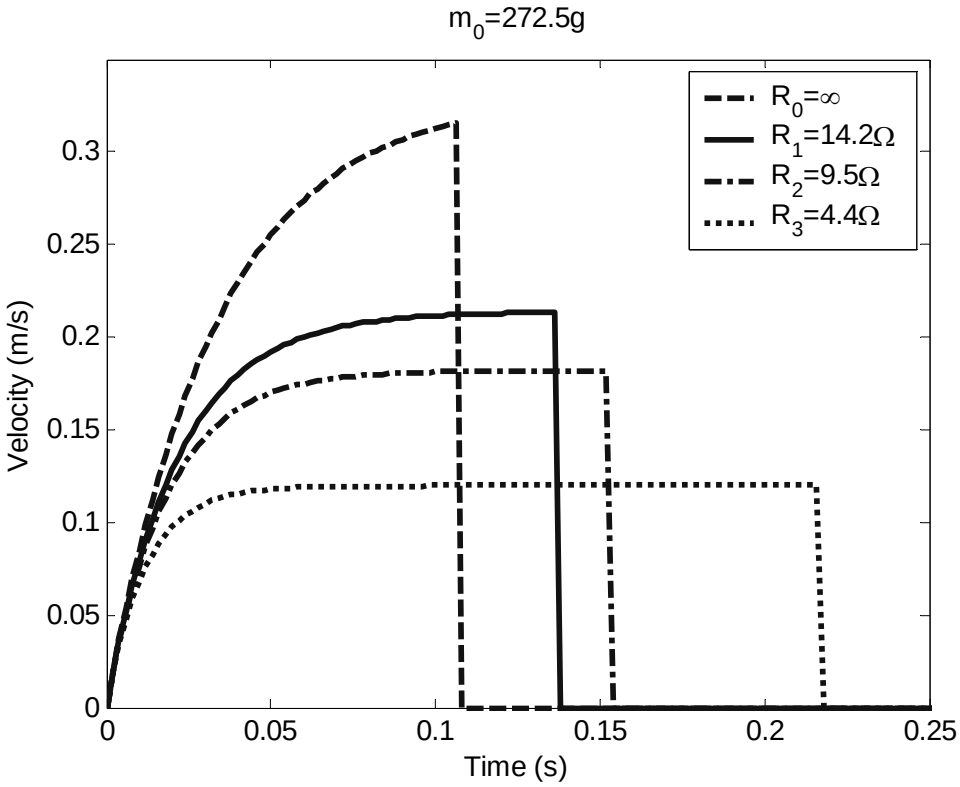

Figure 7.7 Sample Velocity Profiles for Various Circuit Resistance Values.

7.3.4 Experimental Results

The position data extracted from the video frames was differentiated numerically to obtain the velocity and acceleration profiles. This process amplified the noise present in the position data, therefore the position data was smoothed and fitted with a function of the form

$$v = Ae^{-t/\tau_1} + Be^{-t/\tau_2} + Ct + D \tag{7.4}$$

using the curve-fitting toolbox in Matlab®. This function was differentiated to obtain the velocity and force estimates of the damper device.

Sample position and velocity profile curves are shown in Figure 7.8 and Figure 7.9, respectively. Both plots show the mass displacement as a positive value so that the end of the displacement is at the top of the graph. Notice the oscillations of the mass described previously at the end of its displacement. These oscillations are discarded during the curve fitting process and the comparison with the simulation results in the following sub-section.

Table 7.6 and Table 7.7 summarize the experimental results. The first table shows the fall time measured from the position data, while the second table shows the terminal velocities reached by the falling mass.

Table 7.6 Experimental Time (s) to End of Travel.

		Circuit Resistance			
		R_0	**R_1**	**R_2**	**R_3**
Drop Mass	**m_0**	0.102	0.133	0.154	0.238
	m_1	0.091	0.111	0.125	0.181
	m_2	0.087	0.101	0.108	0.148
	m_3	0.083	0.095	0.099	0.130

Table 7.7 Experimental Maximum Velocity (m/s).

		Circuit Resistance			
		R_0	**R_1**	**R_2**	**R_3**
Drop Mass	**m_0**	0.38	0.22	0.18	0.11
	m_1	0.43	0.30	0.25	0.15
	m_2	0.46	0.35	0.29	0.18
	m_3	0.47	0.39	0.34	0.22

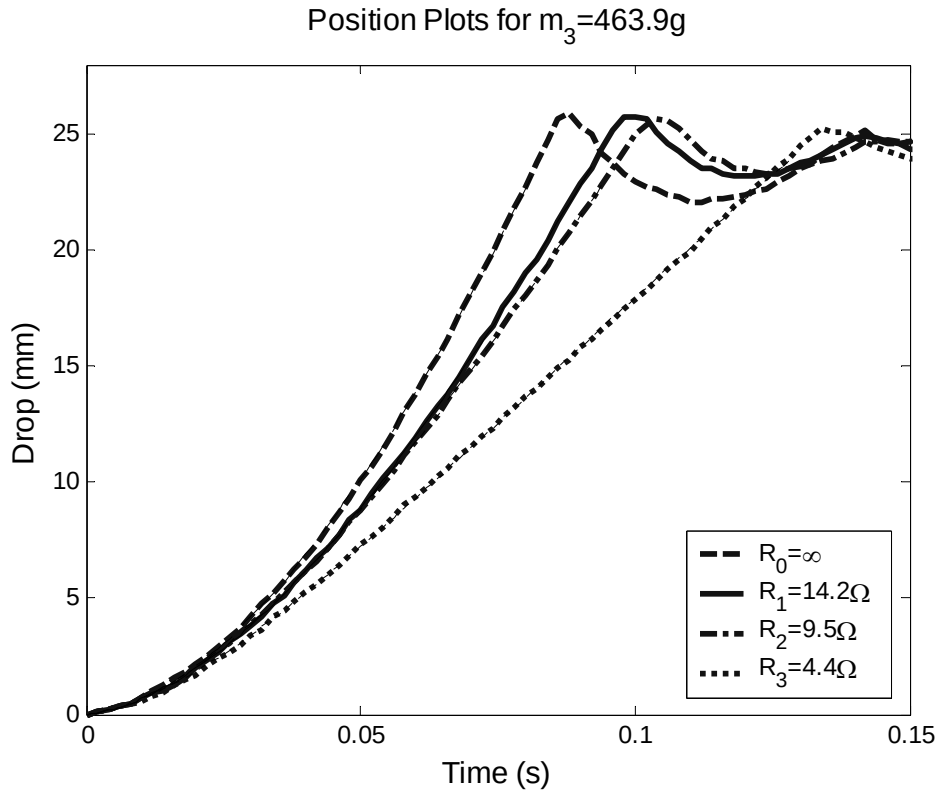

Figure 7.8 Sample Experimental Position Curves for Various Circuit Resistance Values.

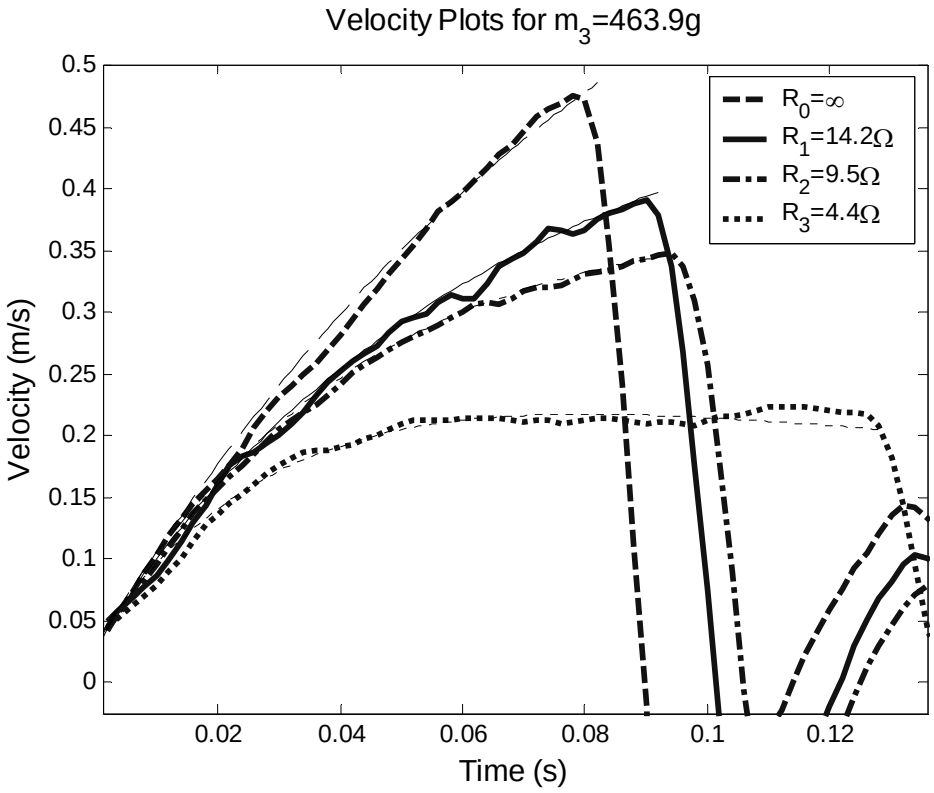

Figure 7.9 Sample Experimental Velocity Curves for Various Circuit Resistance Values.

7.3.5 Discussion

A sample graphical comparison between the experimental and simulated position profiles generated using the biggest mass for all four resistances is shown in Figure 7.10. Table 7.8 shows the numeric comparison between the simulated and experimental results as a percentage difference.

Table 7.8 Time (ms) to End Comparison Between Simulated and Experimental Results.

	R_0			R_1			R_2			R_3		
	Sim.	**Exp.**	**Diff.**	**Sim.**	**Exp.**	**Diff.**	**Sim.**	**Exp.**	**Diff.**	**Sim**	**Exp.**	**Diff.**
$\mathbf{m_0}$	106	102	-4%	136	133	-2%	152	154	1%	216	238	10%
$\mathbf{m_1}$	96	91	-5%	118	111	-6%	130	125	-4%	180	181	1%
$\mathbf{m_2}$	92	87	-5%	108	101	-6%	118	108	-8%	156	148	-5%
$\mathbf{m_3}$	88	83	-6%	102	95	-7%	108	99	-8%	140	130	-7%

Experimental and simulated data agree within 10% for the measured time. The table shows that for a given mass, the time to the end of travel decreases as the damping decreases, that is as the circuit resistance increases. Also, higher masses (forces) resulted in shorter times.

Table 7.9 offers a similar comparison to the one presented for the position, while Figure 7.11 shows graphically the comparison for the experimental and simulated velocities.

Table 7.9 Final Velocity (m/s) Comparison Between Simulated and Experimental Results.

	R_0			R_1			R_2			R_3		
	Sim.	**Exp.**	**Diff.**	**Sim**	**Exp.**	**Diff.**	**Sim.**	**Exp.**	**Diff.**	**Sim.**	**Exp.**	**Diff.**
$\mathbf{m_0}$	0.31	0.38	23%	0.21	0.22	5%	0.18	0.18	0%	0.12	0.11	-8%
$\mathbf{m_1}$	0.36	0.43	19%	0.26	0.30	15%	0.22	0.25	14%	0.15	0.15	0%
$\mathbf{m_2}$	0.40	0.46	15%	0.30	0.35	17%	0.26	0.29	12%	0.18	0.18	0%
$\mathbf{m_3}$	0.44	0.47	7%	0.34	0.39	15%	0.30	0.34	13%	0.20	0.22	10%

Experimental agree within 25% of the simulation data. Higher damping results in lower velocities, and higher forces applied result in lower velocities developed. Figure 7.11 also shows that at higher damping conditions (lower circuit resistance) the velocity of the mass reaches the terminal velocity of the system. That is, the velocity when the force of the damper equals the weight of the mass.

In general, the discrepancy between experimental and simulation data increases as the mover mass increases, and decreases as the damping increases.

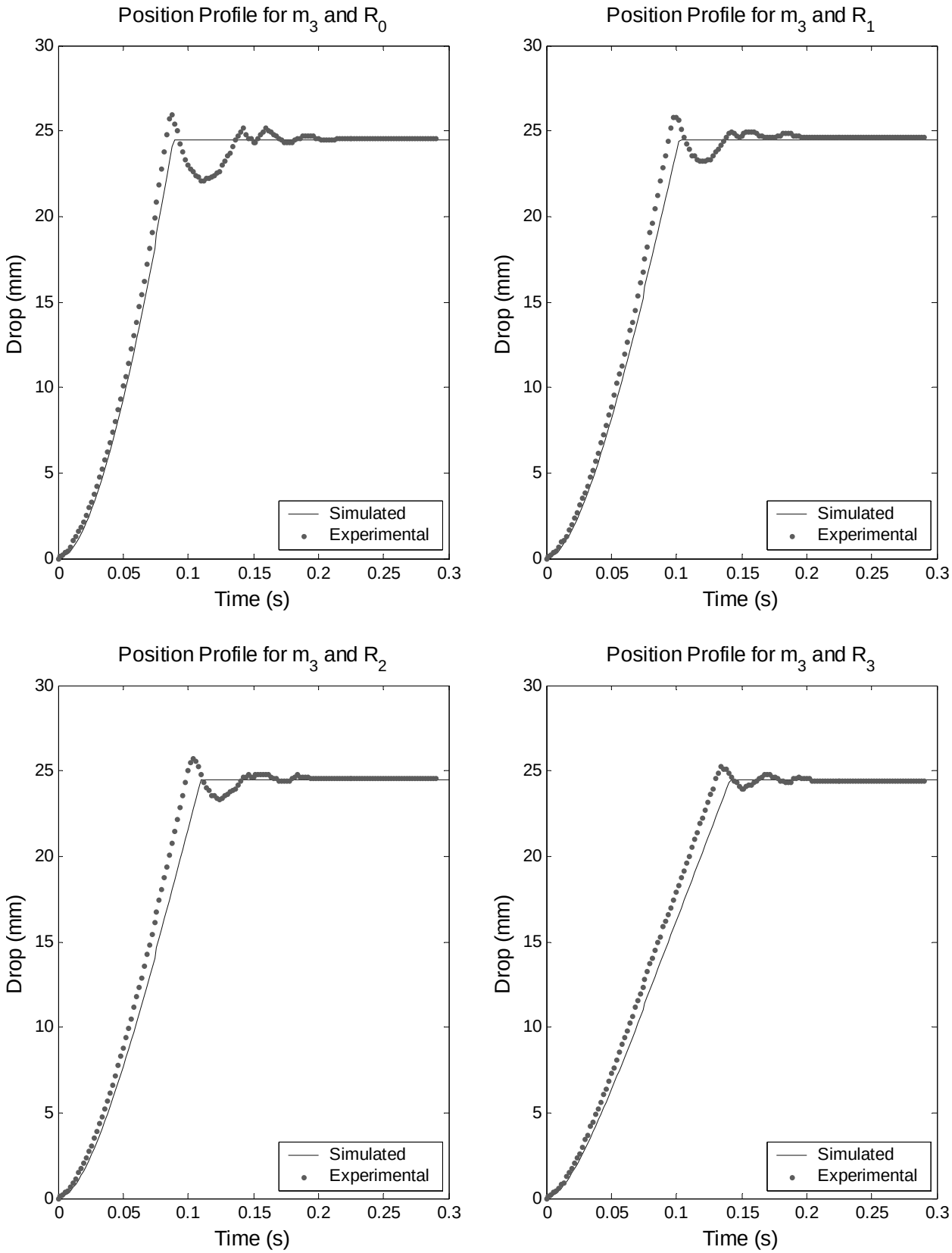

Figure 7.10 Position Profile Comparison for Experimental and Simulation Data (m_3=463.9g)

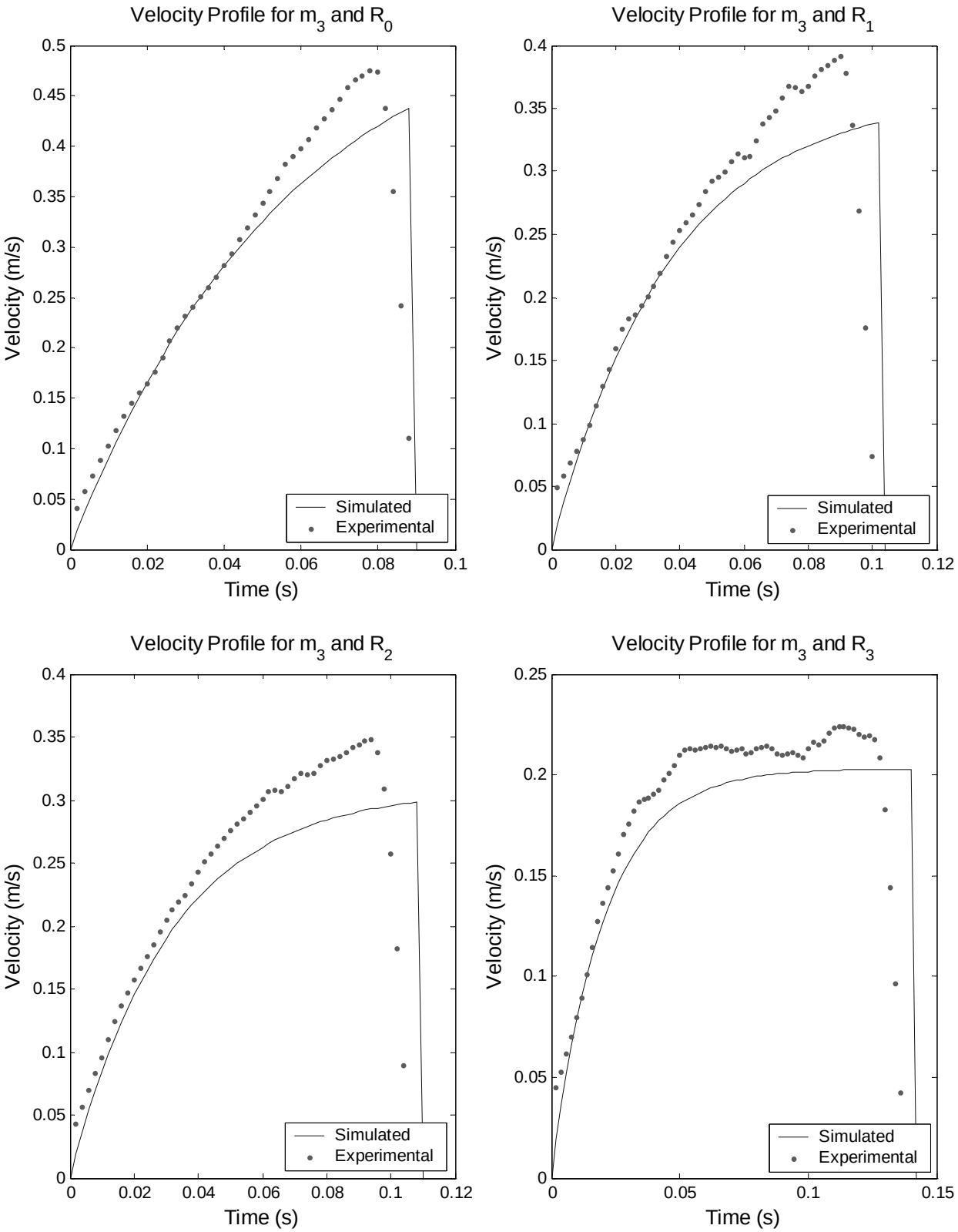

Figure 7.11 Velocity Profile Comparison for Experimental and Simulation Data (m_3=463.9g).

Table 7.10 Damping Coefficient Values as function of Circuit Resistance.

Circuit Resistance R_{circ}	Damping Coefficient c_d (N-s/m)		
	Theoretical	**Simulated**	**Experimental**
$R_0=\infty$	0	8.2	3.4
R_1=14.2 Ω	4.39	12.7	8.2
R_2=9.5 Ω	6.57	14.8	11.2
R_3=4.4 Ω	14.2	22.5	23.3

Table 7.10 compares the effective damping coefficients obtained experimentally and from the simulation with the theoretical values for the electromagnetic damper. The experimental and simulation coefficients include the effects of the parasitic and the electromagnetic damping, whether the theoretical value only includes the electromagnetic damping.

The table shows a relatively big discrepancy between the theoretical and both the simulated and experimental values. This was expected as the theoretical calculations neglected the damping produced by mechanism other than the electromagnetic effects. The difference between the theoretical and simulated is constant and corresponds to the non-electromagnetic damping modeled as linear damping in the simulation. The difference between the theoretical and experimental coefficients increases as the damping increases.

The differences between the simulated and experimental data, also vary with the circuit resistance value. However, this variation is different than with the theoretical damping. As the damping increases, the difference between the coefficients decreases. With no electric load connected to the machine, the difference is 4.8N-s/m while at the lowest circuit resistance tested the difference reduces to just 0.8N-s/m. This is because at smaller circuit resistances, the electromagnetic force increases overcoming the forces from other mechanisms, such as friction, therefore the better agreement between the simulation and the experimental results.

7.4 Oscillatory Velocity Response

7.4.1 Experiment Description

This experiment measures the force produced by damper and its effective damping coefficient, when the device is excited using cyclic velocity profiles. The experimental set up is depicted in Figure 7.12. It consists of a brushless rotational dc motor attached to the electromagnetic damper through a rotational-to-linear linkage. A load cell is located in the linkage between the motor and the damper.

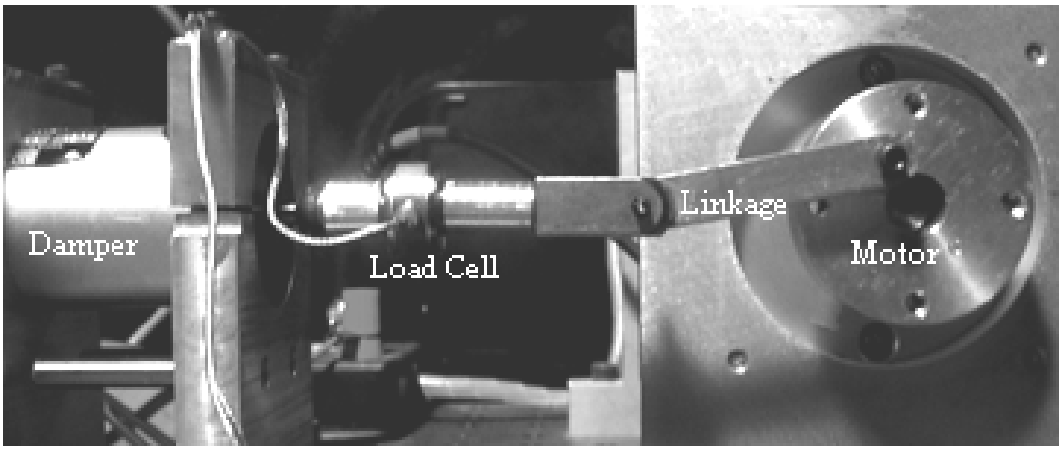

Figure 7.12 Cyclic Velocity Experimental Setup.

A closed-loop control system is used to regulate the angular velocity of the motor, which through the geometry of the linkage, prescribes the linear velocity of the damper. A proportional-integral controller is implemented as the regulator using operational amplifier circuits. The regulator is designed to minimize the effects of the damper reaction torque on the angular velocity.

The load cell is a tension-compression load cell manufactured by Honeywell, model 31. A regulated 5V power supply powers the sensor, and an instrumentation amplifier magnifies the output signal. The circuit diagrams and parameters of the force measurement system, as well as that of the control system, are presented in Appendix C.

The velocity is measured by a tachometer connected to the motor shaft, while the damper reaction force is measured by the load cell in the system. The angular position is read by a potentiometer also on the motor shaft.

The measurements are recorded and processed on a personal computer equipped with analog-to-digital conversion card and data acquisition software. Table 7.11 shows the conversion factors for the sensors monitored in the system.

Table 7.11 System Sensors Constant Values.

Sensor	Signal	Gain
Tachometer	Ang. Velocity	0.0286 V-s/rad
Potentiometer	Ang. Position	0.25 V/rad
Load Cell	Force	0.231 V/N

The experiment is repeated for each of the values of angular velocity shown in Table 7.12 and, to facilitate the comparison of the data produced by the various experiments, the resistance values shown in Table 7.3 previously.

Table 7.12 Prescribed Velocity Experiment Parameters.

Motor Velocity (rad/s)	Control Voltage (V)	Max. Damper Velocity (m/s)
4.19	0.12	0.05
8.38	0.24	0.10
20.4	0.59	0.25
40.8	1.18	0.50

7.4.2 System Model

Geometric Relationships

Since the purpose of this experiment is to determine the damper force given its displacement rate, in this section we determine the relationships between the damper velocity and the system measurements of angular position and velocity of the driving motor.

The geometry of the linkage mechanism between the rotational motor and the linear electromagnetic damper determines the linear velocity profile applied to the damper given the angular movement of the motor. Figure 7.13 shows the geometric description of the system shown in the picture of Figure 7.12. The circle centered at O with radius r represents the motor, while the electromagnetic damper moves in the direction of segment CD. The linkage connects to the motor at point A and to the damper at point B, and has a length l. The location x and speed v

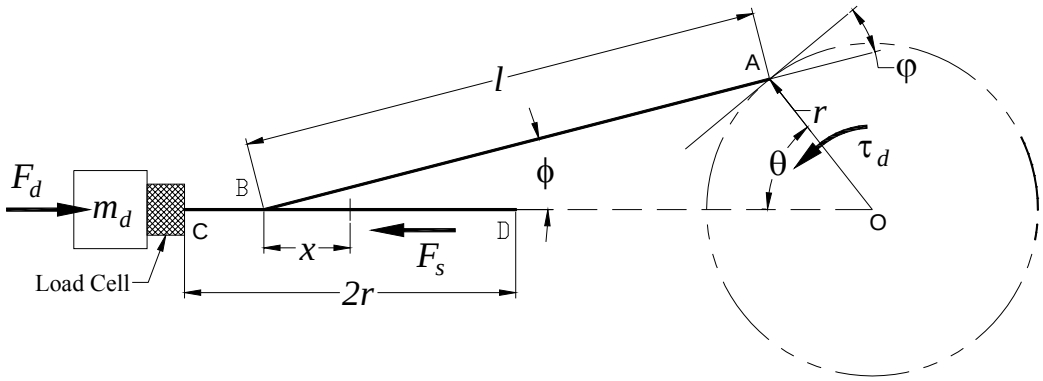

Figure 7.13 Geometric and Force Diagram of Linkage System.

of point B are a function of the angle θ and the constant angular velocity ω_m of point A as it rotates counter-clockwise on the circumference O.

Applying trigonometry to the triangle ABO in Figure 7.13 we have:

$$\begin{cases} r\sin\theta = l\sin\phi \\ -r\cos\theta + l\cos\phi = l + x \end{cases} \tag{7.5}$$

Solving this set of equations in terms of θ, we find the following expression for the position *x*

$$x = -r\cos\theta + l - \sqrt{l^2 - r^2\sin^2\theta} \tag{7.6}$$

Since ω_m is constant, we can substitute $\theta = \omega_m t$ and take the time derivatives of the position to find the expression for the velocity *v* and acceleration *a* of the damper shaft

$$v = r\omega_m \sin(\omega_m t)\left(1 + \frac{r\cos(\omega_m t)}{\sqrt{l^2 - r^2\sin^2(\omega_m t)}}\right) \tag{7.7}$$

$$a = \omega_m^2\left(r\cos(\omega_m t) + \frac{r^2\left(\cos^2(\omega_m t) - \sin^2(\omega_m t)\right)}{\sqrt{l^2 - r^2\sin^2(\omega_m t)}} + \frac{r^4\cos^2(\omega_m t)\sin^2(\omega_m t)}{\left(l^2 - r^2\sin^2(\omega_m t)\right)^{3/2}}\right) \tag{7.8}$$

Notice that as the length *l* of the linkage increases relative to the radius *r* of the driving circle, the velocity and acceleration profiles approximate that of a pure sinusoidal displacement profile. Figure 7.14 shows the normalized graphs of equations (7.6) through (7.8) together with the corresponding sinusoidal displacements for one cycle period.

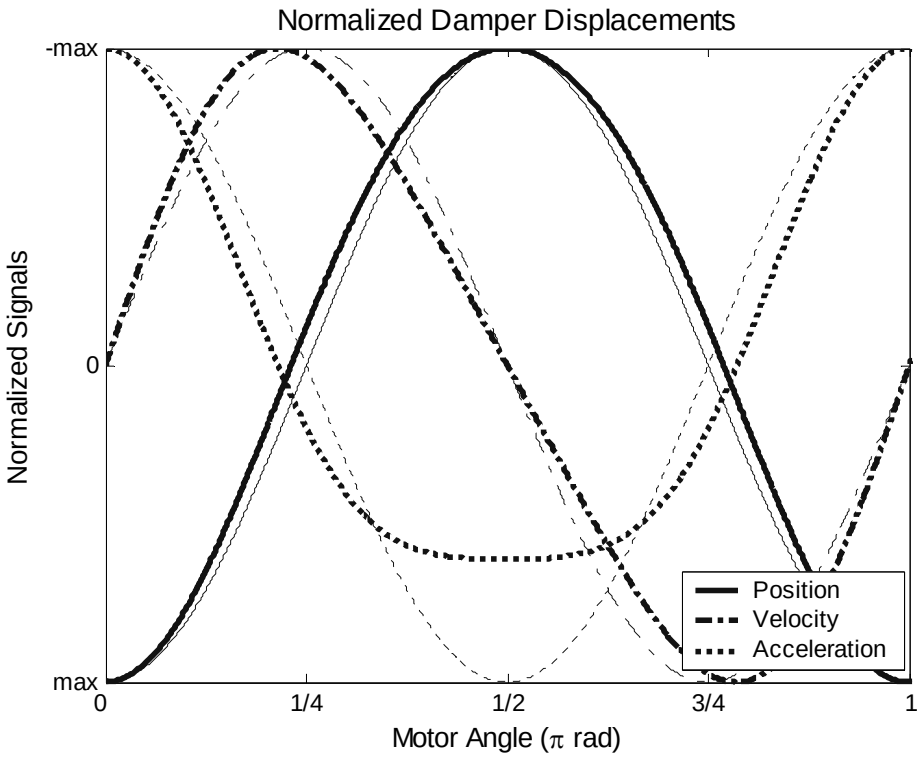

Figure 7.14 Normalized Damper Displacement Profiles and Ideal Sinusoidal Profiles.

Force Measurement

Given that the velocity is a function of the angular position and velocity, we can estimate the damper reaction force F_d using the constitutive relationship (3.27) with the value v from the above equation,

$$L_{coil}\frac{dF_d}{dt}+(R_{coil}+R_{load})F_d=-K_t^2 r\sin(\omega_m t)\left(1+\frac{r\cos(\omega_m t)}{\sqrt{l^2-(r\sin(\omega_m t))^2}}\right)\omega_m \tag{7.9}$$

The load cell is located between the damper and the motor linkage (Figure 7.12), therefore it measures the damper force together with the force due to the moving mass m_d of the damper. Applying the force equilibrium equations to the sensor and mover mass shown in the left of the body diagram in Figure 7.13 we find the sensor force measurement

$$F_s = F_d + m_d a \tag{7.10}$$

Appendix E shows the Matlab® scripts used to obtain the theoretical reaction force of the damper and the expected load cell measurements for the various angular velocities of Table 7.12.

7.4.3 Simulation Results

Table 7.13 below summarizes the simulation force results with and without considering the parasitic damping in the machine. The parasitic damping used is the same as used previously, c_f=*8.2N-s.m.*

Table 7.13 Simulated Maximum Measured Damper Force.

Motor Velocity (rad/s)	Max. Damper Velocity (m/s)	Max. Damper Force (N)							
		R_0		R_1		R_2		R_3	
4.19	0.052	0.025	0.45	0.23	0.66	0.34	0.77	.735	1.16
8.38	0.103	0.05	0.89	0.46	1.30	0.68	1.52	1.47	2.31
20.4	0.252	0.12	2.19	1.11	3.18	1.66	3.73	3.58	5.65
40.8	0.504	0.24	4.37	2.22	6.35	3.31	7.44	7.15	11.3

Figure 7.15 and Figure 7.16 show the top sections of the simulated force profiles for the damper and sensor for the lowest and highest velocity tested experimentally at both a high and a low damping settings. These plots show that the actual and measured damper forces are close enough that for experimental purposes their difference is negligible.

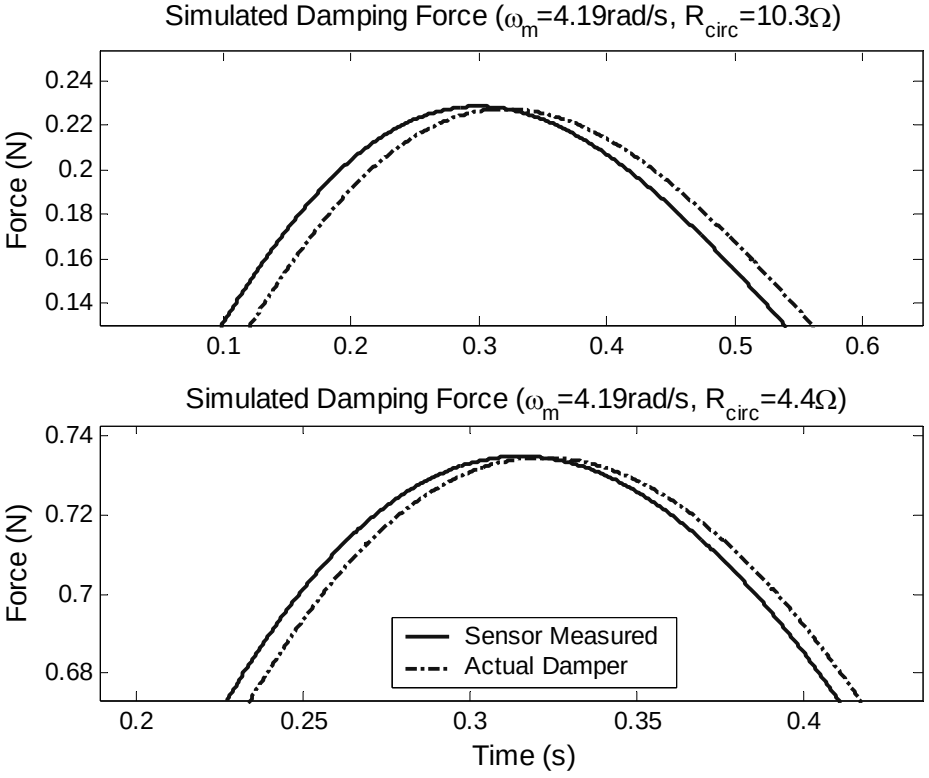

Figure 7.15 Simulated Force Profiles at Low Velocity.

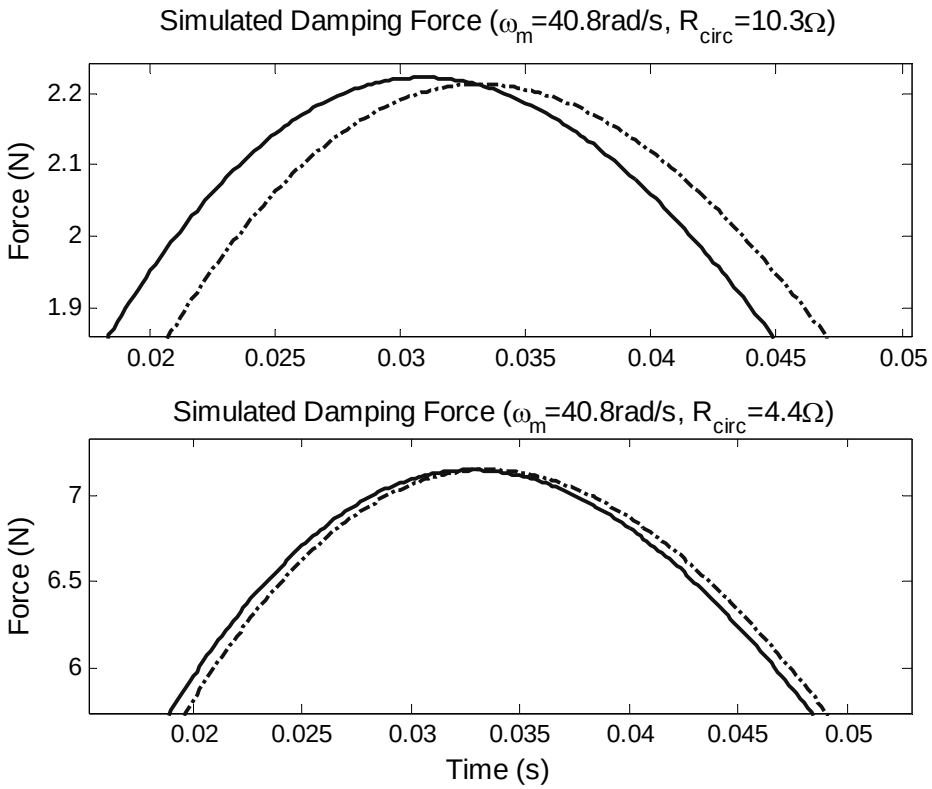

Figure 7.16 Simulated Force Profiles at High Velocity.

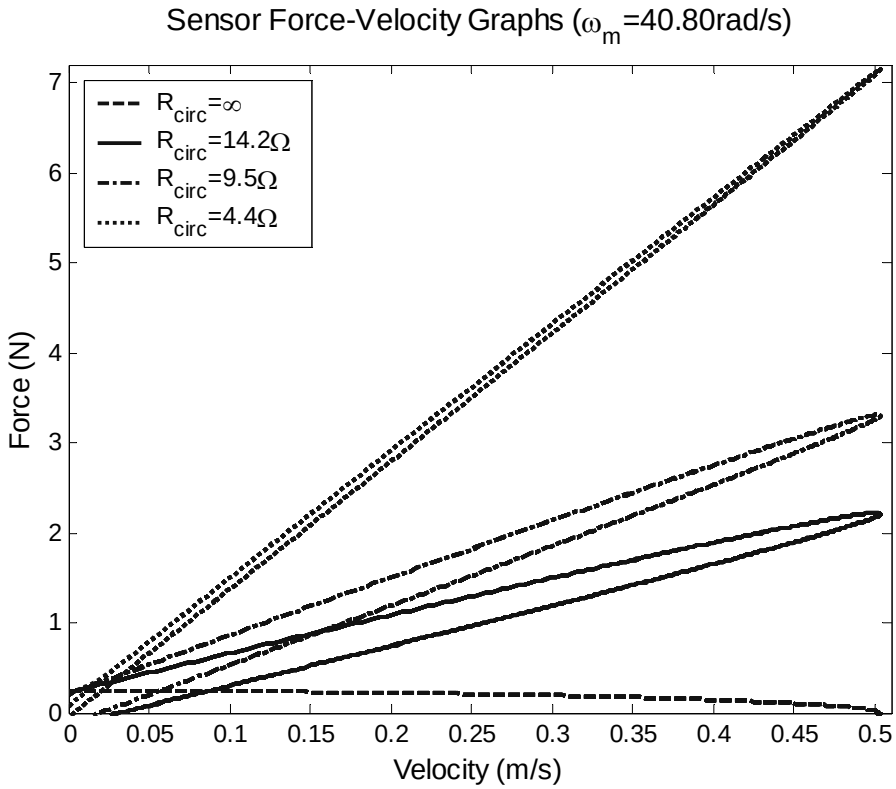

Figure 7.17 Simulated Measured Force-Velocity Plot at High Velocity

7.4.4 Experimental Results

Table 7.14 summarizes the maximum measured for the different system velocities and damping settings (load resistance values). Sample time-domain force plots for the maximum damping setting are shown in Figure 7.18 and Figure 7.19. The first plot shows the force profile at a low velocity, while the second figure shows the profile at the highest velocity tested.

Table 7.14 Experimental Maximum Measured Damper Force.

Motor Velocity (rad/s)	Max. Damper Velocity (m/s)	Max. Damper Force (N)			
		R_0	R_1	R_2	R_3
4.19	0.044	0.52	0.69	0.77	1.08
8.38	0.096	0.76	1.03	1.22	1.81
20.4	0.249	1.58	2.19	2.63	4.02
40.8	0.51	4.08	4.85	5.71	8.31

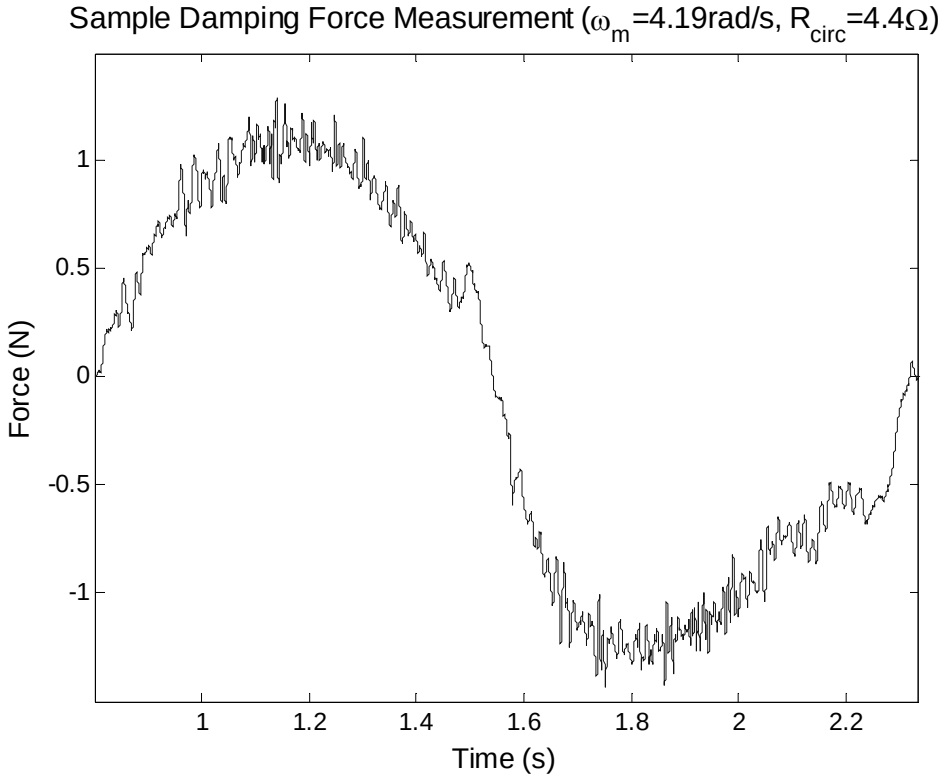

Figure 7.18 Sample Force Measurement Signal at Low Velocity and Highest Damping Setting.

Figure 7.19 exhibits oscillations in the force measurement curve that are not present in Figure 7.18. These oscillations result from the dynamic response of the force sensor, and they become more severe as the speed of the damper mover increases.

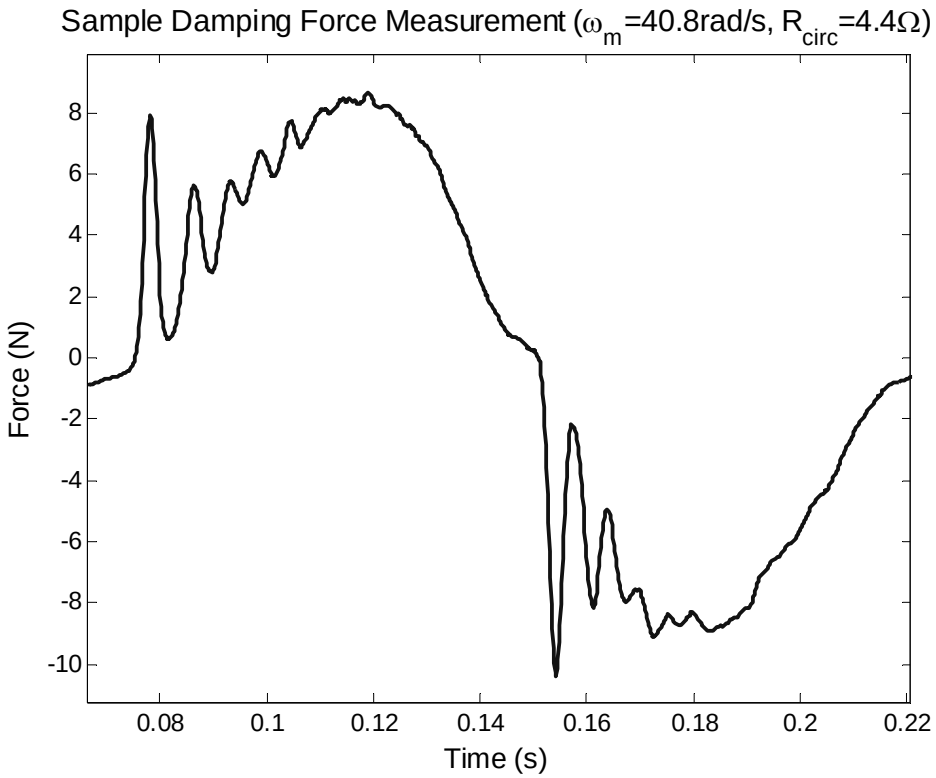

Figure 7.19 Sample Force Measurement Signal at High Velocity.

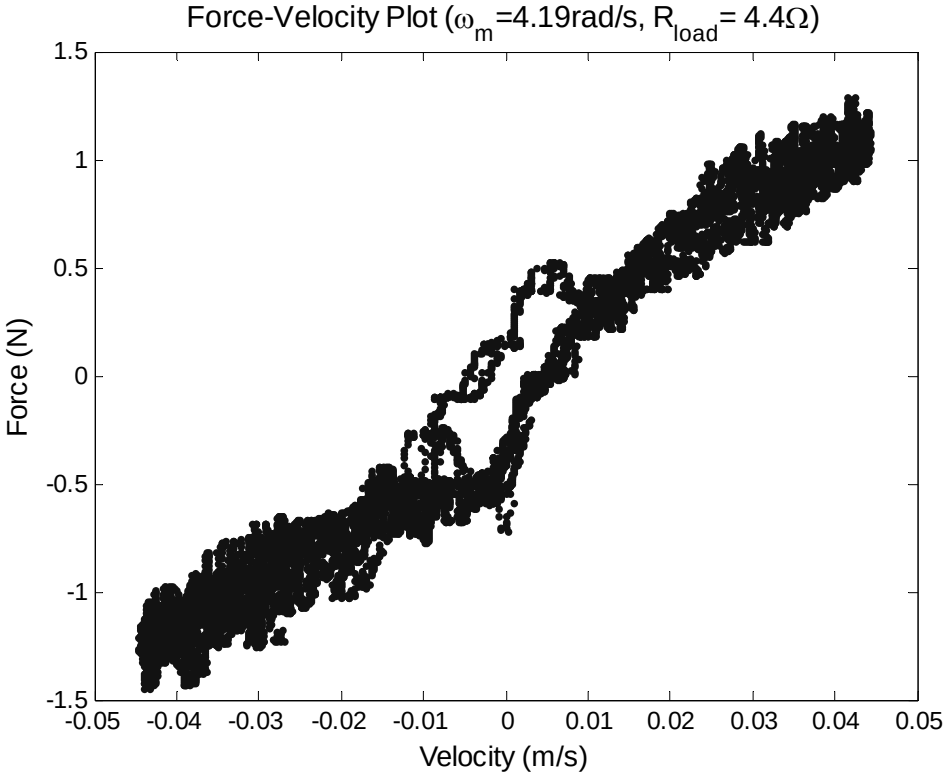

Figure 7.20 Sample Measured Force-Velocity Plot at Low Velocity.

Figure 7.20 above shows a sample force-velocity plot obtained from the data collected. This plot shows that the general profile of the force-velocity relationship of the electromagnetic damper approximates that of a linear damper.

7.4.5 Discussion

Table 7.15 shows the numerical comparison between the simulated force amplitude and the force measured experimentally. The data show better agreement at lower damper velocities than it does at higher velocities. The sensor dynamic behavior tainted the accuracy of the measurements at higher velocities by causing artificial oscillations in its output.

Table 7.15 Comparison Between Simulated and Experimental Maximum Damper Force.(N).

Damper Velocity (m/s)	$R_0=\infty$			$R_1=14.2\ \Omega$			$R_2=9.5\ \Omega$			$R_3=4.4\ \Omega$		
	Sim	Exp	% Diff	Sim	Exp	% Diff	Sim	Exp	% Diff	Sim	Exp	% Diff
0.044	0.45	0.52	15.6	0.66	0.69	4.5	0.77	0.77	0.0	1.16	1.08	-6.9
0.096	0.89	0.76	-14.6	1.30	1.03	-20.8	1.52	1.22	-19.7	2.31	1.81	-21.6
0.249	2.19	1.58	-27.9	3.18	2.19	-31.1	3.73	2.63	-29.5	5.65	4.02	-28.8
0.51	4.37	4.08	-6.6	6.35	4.85	-23.6	7.44	5.71	-23.3	11.3	8.31	-26.5

Table 7.16 Damping Coefficient Values as a Function of Circuit Resistance.

Circuit Resistance R_{circ}	Damping Coefficient c_d (N-s/m)		
	Theoretical	Simulated	Experimental
$R_0=\infty$	0	8.65	8.12
$R_1=14.2\ \Omega$	4.39	12.7	10.6
$R_2=9.5\ \Omega$	6.57	14.8	12.4
$R_3=4.4\ \Omega$	14.20	22.4	18.1

Table 7.16 presents the effective damping coefficients obtained from the simulation and experimental data. The theoretical values of damping coefficient are smaller than both simulated and experimental values. This is due to the presence of damping mechanisms in the system that were not accounted in the mathematical model. In addition, the simulated coefficients are larger than the experimental ones because uncertainties on the parasitic damping estimation and the nonlinear behavior of these damping mechanisms, like friction, which are not accounted for during the simulations of the damper model.

7.5 Summary

We performed two experiments to examine the behavior of the electromagnetic damper and validate the derived mathematical models of the device. In the first experiment, a constant force was applied to the device and its displacement measured to estimate the damper force. In the second experiment, the machine was driven with a prescribed displacement and the reaction force of the damper measured. The characterization of the device was performed by computing the effective damping coefficients from the collected data and comparing it to the coefficients computed using the mathematical models of the experimental systems.

The results obtained from the two experiments verified that a linear permanent magnet machine behaves as a damper when a resistive load is connected across its terminals. The general shape of the force-velocity curve of the electromagnetic damper approximated that of a linear damper with the damping coefficient increasing with lower load resistances.

Table 7.17 Summary of Experimental Damping Coefficients (N-s/m).

Circuit Resistance (Ω)	Simulated	Constant Force		Oscillatory Velocity	
Open Circuit	8.65	3.4	60.7%	8.12	6.13%
14.2	12.7	8.2	35.4%	10.6	16.5%
9.5	14.8	11.2	24.3%	12.4	16.2%
4.4	22.4	23.3	4.02%	18.1	19.2%

Numerically, however, the experimental values of damping coefficient (Table 7.17) were smaller than the values obtained from the simulations in both experiments. The oscillatory velocity experiments results were within 20% of the simulation results. This agreement was better than the constant force experiment, with the exception of the highest damping case (smallest resistance) in which the experimental damping coefficient was only 4% greater than the simulated value, versus 19% for the oscillatory response. Discrepancies between the simulation and experimental values can be attributed in part to the inaccuracies in the data acquisition systems and uncertainties in the model of the non-electromagnetic damping.

Chapter 8
Conclusions and Recommendations

8.1 Conclusions

The research presented in this thesis developed a new kind of passive structural damper based on electromagnetic effects. This electromagnetic damper converts the kinetic energy imparted to a building by a disturbance, like wind or an earthquake, into electric energy rather than just heat or material deformation as do current structural damping devices.

The immediate contributions of this thesis are the following:

- The development of the structural electromagnetic damper as a passive device and its mathematical description;
- A feasibility study of the electromagnetic damper applied to full-scale buildings;
- The methodology to design an electromagnetic damper given a desired damping performance and;
- The introduction of the mathematical model for the dynamic response analysis of building with electromagnetic dampers.

This research introduces not only a new application for electric machines and a new type of damping device, but also the design and analysis tools to use this new device. These are described and summarized in the following sections.

8.1.1 Damper Modeling

This research started by proposing and analyzing a tubular linear permanent magnet machine as a structural damper. A mathematical model of the device was derived from quasi-static electromagnetic principles, demonstrating that the force-velocity relationship of the tubular electromagnetic damper is similar to that of an ideal damper. The mathematical analysis of the electromagnetic is different than previous analyses of electric machines in that it describes the

behavior of the machine operating as a damper, rather than as a motor or a generator.

The damper behavior is described by a first order differential equation relating the damper velocity to the damper reaction force. Under sinusoidal excitation, the damper force-velocity relationship can be expressed in terms of an effective damping coefficient and a time delay (or phase shift) that depend on the machine constant and impedance on the electric side of the machine. The geometric, magnetic and electric parameters of the device determine the damper constants and circuit impedances. The mathematical model was validated via experimental work using a scale prototype electromagnetic damper.

8.1.2 Damper Feasibility

Once the mathematical model describing the force-velocity behavior of the electromagnetic damper was developed, a feasibility study of the device applied to full-scale building structures was conducted. Two performance measures, damping density and damping cost, were used to evaluate and compare the electromagnetic damper with other damping devices, in particular viscous fluid dampers.

To obtain the same damping capacity as a lower-end fluid damper, the electromagnetic damper uses at least one-and-a-half times the volume of the fluid damper. However, as the magnet technology progresses creating magnets with higher energy products, the damping density will certainly increase.

With the state of current magnet prices and technology, electromagnetic dampers have a cost that is at least five times bigger than that of fluid dampers. However, the price should drop following two conditions: the expiration of the permanent magnet patents currently held by two companies and the economies of scale obtained with mass production of the device.

Although the performance of the electromagnetic damper using current technology and materials is lower than the performance of viscous fluid dampers, the electromagnetic damper has flexibility not available with other damping devices provided by using electricity as its dissipative mechanism. For example the electromagnetic damper can operate as an actuator or as semi-active damper without any physical changes to the device, but this thesis only addresses passive operation of the damper.

8.1.3 Damper Design and Building Response Analysis

Two tools were developed that facilitate the application of electromagnetic damper to buildings and structures. The first one is a basic design methodology for the electromagnetic dampers, while the second is an analysis methodology for buildings with electromagnetic dampers.

The design methodology follows a hybrid graphical and analytical approach to find the damper parameters that meet a specified damping criteria and space constraints. The design criteria for the geometric parameters of the device are chosen sequentially based on the performance measures introduced during the feasibility study. The methods takes advantage of the modularity inherent to electric machines and reduces the design process to an hypothetical single pole machine which is then scaled by a scalar multiplication of the pole unit to meet the specified damping.

The analysis methodology follows two different approaches to the modeling of lumped-parameter buildings with electromagnetic dampers. The first approach is based on modal analysis, or frequency domain, methods and characterizes the dampers as idealized dampers whose damping coefficients depend, in addition to the machine properties, on the frequency of excitation. The second approach is based on a time-domain state-space representation of lumped-parameter building and the electromagnetic dampers. The space of the system is augmented to incorporate the dampers relationships with their dynamic characteristics.

The former approach is used when investigating the steady-state sinusoidal response of the system or when the disturbance signals can be represented by means of power or amplitude spectra. The latter approach applies to transient response analysis of the system and requires a time description of the disturbance signal.

The design and analysis methodologies described in this section provide basic tools for incorporating electromagnetic dampers in buildings or civil structures. The design tool is applied to find the electromagnetic damper device the meets the damping requirement of the building. The analysis tool is used to verify the dynamic building response when the designed electromagnetic damper is used in the building.

8.2 Areas of Future Research

The current work opens a new area of research in the field of structural motion control devices, and as such it introduced the basic concepts and model of the electromagnetic damper. In order to bring the electromagnetic damper to a practical implementation, research is needed in the following areas:

- Modeling and analysis: for example, higher order effects, such as self-heating and temperature, should be considered in the model of the device. Also, the effects of changes of polarity in the coil caused by the translator moving more than a magnet length distance should be investigated.
- Manufacturing: an actual implementation of electromagnetic damper in buildings depends greatly on the fabrication of the device. Practical consideration such as material handling, permanent magnets assemblies and magnetization, supporting hardware, connections details, to name a few, are of great importance.
- Materials: the performance of electromagnetic dampers significantly depends on the physical properties of the materials used in the device construction.
- Design optimization: algorithms should be developed in order to optimize the design of the electromagnetic damper to increase their performance or reduce their cost.
- Device operation: one of the advantages the electromagnetic damper has is the flexibility it offers. Power electronic circuits and control algorithms should be developed to take advantage of this flexibility by allowing the operation of the device in the different modes (active, passive, hybrid or regenerative) or by adjusting its force-velocity relationship.

References

Amara, Y., et al. (2004). Stator iron loss of tubular permanent magnet machines. Industry Applications Conference, 2004. 39th IAS Annual Meeting. Conference Record of the 2004 IEEE.

Arshad, W. M., et al. (2002). "Integrated Free-Piston Generators: An Overview." IEEE Transactions on Magnetics.

Barmada, S., et al. (2000). "Field analysis in axisymmetric actuators." Magnetics, IEEE Transactions on **36**(4): 1906-1909.

Beard, A. M. (1993). Regenerative Isolation as an Alternative to Active Vibration Control. Mechanical Engineering. Davis, California, University of California, Davis**:** 240.

Beards, C. F. (1996). Structural vibration : analysis and damping. London, Arnold-Halsted Press.

Beaty, H. W. and J. L. Kirtley (1998). Electric Motor Handbook. New York, NY, McGraw-Hill.

Bianchi, N., et al. (2003). "Tubular Linear Permanent Magnet Motors: An Overall Comparison." IEEE Transactions on Industry Applcations **39**(2): 466-475.

Bianchi, N., et al. (2001). Design criteria of a tubular linear IPM motor. Electric Machines and Drives Conference, 2001. IEMDC 2001. IEEE International.

Boldea, I. and S. A. Nasar (1987). "Permanent-Magnet Linear Alternators--Part I: Fundamental Equations." IEEE Transactions on Aerospace Electronic Systems **23**(1): 73-78.

Boldea, I. and S. A. Nasar (1987). "Permanent-Magnet Linear Alternators--Part II: Design Guidelines." IEEE Transactions on Aerospace Electronic Systems **23**(1): 79-82.

Boldea, I. and S. A. Nasar (1997). Linear Electric Generators. Linear Electric Actuators and Generators. New York, Cambridge Universtiy Press**:** 201-234.

Buchholdt, H. A. (1997). Structural Dynamics for Engineers. London, Great Britain, Thomas Telford Publications.

Canova, A., et al. (2001). Synthesis of Linear Actuators. Compel. Bradford. **20:** 713-723.

Cheng, F. Y. (2001). Matrix analysis of structural dynamics : applications and earthquake engineering. New York, Marcel Dekker.

Connor, J. J. (2003). Introduction to Structural Motion Control. New Jersey, Prentice Hall.

Coutel, C., et al. (1999). Constrained optimisation of a linear actuator: comparison of two methods to deal with implicit parameters in the analytical model. Electric Machines and Drives, 1999. International Conference IEMD '99.

DelToro, V. (1990). Basic Electric Machines. Englewood Cliffs, NJ, Prentice-Hall, Inc.

Deng, Z., et al. (1987). "Forces and parameters of permanent magnet linear synchronous machines." Magnetics, IEEE Transactions on **23**(1): 305-309.

Eastham, J. F., et al. (1990). "Optimum design of brushless tubular linear machines." Magnetics, IEEE Transactions on **26**(5): 2547-2549.

El-Hawary, M. E. (2002). Principles of Electric Machines with Power Electronic Applications. New York, NY, Wiley-Interscience.

Fodor, M. G. and R. C. Redfield (1992). The Variable Linear Transmission for Regenerative Damping in Vehicle Suspension Control. American Control Conference, Chicago, IL, American Automatic Control Council.

Friedland, B. (1986). Control System Design: An Introduction to State-Space Methods. Boston, Massachusets, McGraw-Hill.

Graves, K. E., et al. (2000). "Electromagnetic Regenerative Damping in Vehicle Suspension Systems." International Journal of Vehicle Design **24**(2/3): 182-197.

Haus, H. A. and J. R. Melcher (1989). Electromagnetic Fields and Energy. Englewood Cliffs, New Jersey, Prentice Hall.

Henry, A. and M. Abdullah (2002). Structural Magnetic Induction Damper. Tallahassee, Florida, Florida A&M University**:** 21.

Housner, G. W., et al. (1997). "Structural Control: Past, Present, and Future." ASCE Journal of Engineering Mechanics **123**(9): 897-971.

Jalili, N. (2002). "A Comparative Study and Analysis of Semi-Active Vibration-Control Systems." ASME Journal of Vibration and Acoustics **124**(4): 593-605.

Jang, S.-M., et al. (2002). Design, analysis, and manufacture of large linear motor damper for structural vibration control system. Magnetics Conference, 2002. INTERMAG Europe 2002. Digest of Technical Papers. 2002 IEEE International.

Jang, S.-M. and S.-H. Lee (2003). "Comparison of three types of permanent magnet linear eddy-current brakes according to magnetization pattern." Magnetics, IEEE Transactions on **39**(5): 3004-3006.

Jolly, M. R. (1993). Passive and Regenerative Solutions for Vibration Control. Mechanical Engineering. Davis, California, University of California, Davis.

Jolly, M. R. and D. L. Margolis (1997). "Assessing the Potential for Energy Regeneration in Dynamic Subsystems." ASME Journal of Dynamic Systems, Measurement, and Control **119**(2): 265-270.

Jolly, M. R. and D. L. Margolis (1997). "Regenerative Systems for Vibration Control." ASME Journal of Vibration and Acoustics **119**(2): 208-215.

Kim, S.-S. and Y. Okada (2002). "Variable Resistance Type Energy Regenerative Damper Us-

ing Pulse Width Modulated Step-up Chopper." ASME Journal of Vibration and Acoustics **124**(1): 110-115.

Kim, W.-J., et al. (1996). Analysis and implementation of a tubular motor with Halbach magnet array. Industry Applications Conference, 1996. Thirty-First IAS Annual Meeting, IAS '96., Conference Record of the 1996 IEEE.

Linear-Motors (2005). Motion Products Catalog. Forth Smith, Arkansas, Baldor Electric Company**:** H-39.

Makris, N. (1998). "Viscous Heating of Fluid Dampers. I: Small-Amplitude Motions." ASCE Journal of Engineering Mechanics **124**(11): 1210-1216.

Nagem, R. J., et al. (1995). An Electromechanical Vibration Absorber. 1995 Design Engineering Technical Conference, Boston, Massachusetts, ASME Design Enginnering.

Nakano, K., et al. (2000). "Self-Powered Active Vibration Control Using Continuous Control Input." JSME International Journal, Series C **43**(3): 726-731.

Nakano, K., et al. (1999). "Self-Powered Active Control Applied to a Truck Cab Suspension." JSAE Review **20**(4): 511-516.

Nerves, A. C. (1996). Regenerative Electric Actuators for Active Control of Civil Structures. Electrical Engineering. Blacksburg, Virginia, Virginia Polytechnic Institute and State University**:** 240.

Nerves, A. C. and R. Krishnan (1996). A Strategy for Active Control of Tall Civil Structures using Regenerative Electrical Actuators. 11th ASCE Engineering Mechanics Conference, Fort Lauderdale, Florida, American Society of Civil Engineers.

Nise, N. (2002). Control Systems Engineering.

Okada, Y. and H. Harada (1995). Active and Regenerative Control of Electrodynamic Vibration Damper. 1995 Design Engineering Technical Conference, Boston, Massachusetts, ASME Design Engineering.

Okada, Y. and H. Harada (1996). Regenerative Control of Active Vibration Damper and Suspension Systems. 35th Conference on Decision and Control, Kobe, Japan, IEEE.

Okada, Y., et al. (1996). Active and Regenerative Control of Linear DC Motor Type Damper. Third International Conference on Motion and Vibration Control, Chiba, Japan.

Okada, Y., et al. (1998). Regenerative Control of Moving Mass Type Vibration Damper. The Fourth International Conference on Motion and Vibration Control, ETH Zurich, Switzerland.

Podrzaj, P., et al. (2005). "An enhanced mechanical system for studying the basics of control system dynamics." IEEE Transactions on Education **48**(1): 23-28.

Rasmussen, E. (1997). "Dampers Hold Sway." ASCE Civil Engineering Magazine **67**(3): 40-43.

Scruggs, J. (1999). Active, Regenerative Control of Civil Structures. Electrical and Computer Engineering. Blacksburg, Virginia, Virginia Polytechnic Institute and State University**:** 99.

Sodano, H. A. and J.-S. Bae (2004). "Eddy Current Damping in Structures." The Shock and Vibration Digest **36**(6): 469-478.

Soong, T. T. (1996). Basic Concepts and Applications of Structural Control. 11th ASCE Engineering Mechanics Conference, Fort Laudardale, Florida, American Society of Civil Engineers.

Soong, T. T. and G. F. Dargush (1997). Passive Energy Dissipation Systems in Structural Engineering. New York, John Wiley & Sons.

Spencer, B. F. J., et al. (1996). Magnetorheological Dampers: a New Approach for Seismic Protection of Structures. 35th Conference on Decision and Control, Kobe, Japan, IEEE Decision and Control.

Suda, Y., et al. (1998). Study on The Self-Powered Active Vibration Control. The Fourth International Conference on Motion and Vibration Control, ETH Zurich, Switzerland.

Taylor, D. P. (2003). History, Design, and Applications of Fluid Dampers in Structural Engineering, Taylor Devices Inc, `http://www.taylordevices.com/papers/history/design.htm`.

van Zyl, A. W., et al. (1999). Comparison of force to weight ratios between a single-sided linear synchronous motor and a tubular linear synchronous motor. Electric Machines and Drives, 1999. International Conference IEMD '99.

Vujic, N. (2002). Power Regeneration in Actively Controlled Structures. Mechanical Engineering. Blacksburg, Virgina, Virginia Polytechnic Institute and State University**:** 97.

Wang, J. and D. Howe (2004). "Analysis of axially magnetised, iron-cored, tubular permanent magnet machines." Electric Power Applications, IEE Proceedings- **151**(2): 144-150.

Wang, J., et al. (1999). "A General Framework for the Analysis and Design of Tubular Linear Permanent Magnet Machines." IEEE Transactions on Magnetics **35**(3): 1986-2000.

Wang, J., et al. (2001). "Design optimisation and comparison of tubular permanent magnet machine topologies." IEE Proceedings on Electric Power Applications **148**(5): 456-464.

Webmaster (2005). InfoComm. Market Information in the Commodities Area, `http://r0.unctad.org/infocomm/anglais/indexen.htm`.

Webmaster (2005). Magnetic Component Engineering Home Page, `http://www.mceproducts.com/`.

Woodson, H. H. and J. R. Melcher (1968). Electromechanical Dynamics, Part 1: Discrete Systems. New York, NY, John Wiley & Sons, Inc.

Zagirnyak, M. and S. Nasar (1985). "Fields and permeances of flat rectangular and cylindrical dc electromagnetic structures." Magnetics, IEEE Transactions on **21**(2): 1193-1197.

Appendix A Tubular Electromagnetic Damper Inductance

The self-inductance of a two pole tubular machine is derived using magnetic circuits or reluctance networks. Mutual inductance between the coils in the machine is neglected, as well as flux leakages. Also, the magnetic flux in the machine due to the current in the coil is assumed to be axial while the magnetic flux due to the permanent magnet is neglected. The total inductance of the device is computed by finding the inductance of each coil and adding them up, since the coils are connected in series.

The inductance L is defined as

$$L = \frac{\partial \Lambda}{\partial i} \tag{A.1}$$

where Λ is the flux linkage. For a tightly wound coil, the flux linkage is defined as

$$\Lambda = N\Phi \tag{A.2}$$

where Φ is the flux through each of the N coils. The magnetic flux relates to the magnetomotive force of the coil through the total reluctance seen by the coil as

$$R_{tot}\Phi = Ni \tag{A.3}$$

Substituting equations (A.3) and (A.2) into (A.1) gives the inductance of the coil in terms of the total reluctance,

$$L = \frac{N^2}{R_{tot}} \tag{A.4}$$

Figure A.1 shows a schematic diagram of the two-pole electromagnetic damper. This figure depicts the relevant dimensions for computing the system reluctances and the relative position of the stator and mover, while Figure A.2 shows the equivalent reluctance networks seen by each coil in the damper. The reluctance of a component is computed using

$$R = \int_C \frac{dl}{\mu A} \tag{A.5}$$

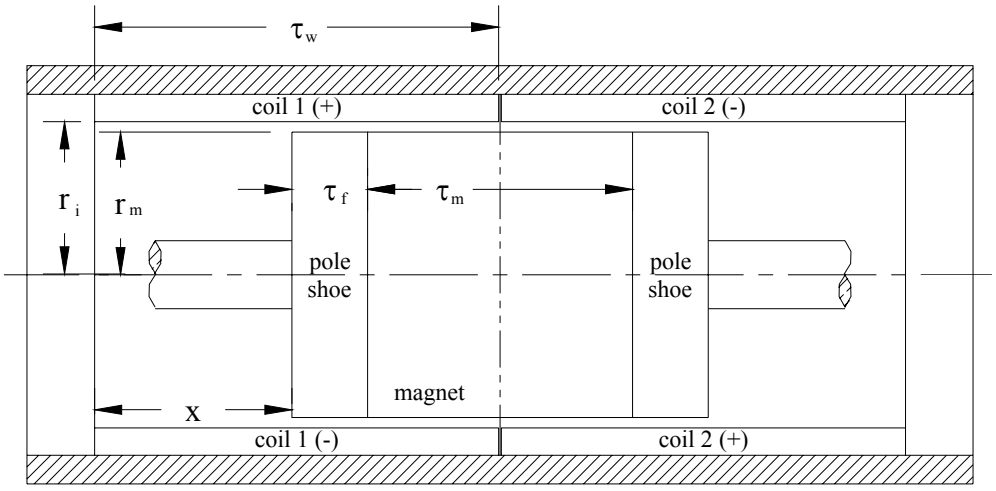

Figure A.1 Electromagnetic Damper Schematic Diagram.

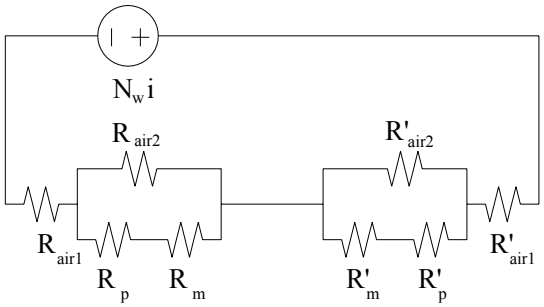

Figure A.2 Electromagnetic Damper Coil Reluctance Network

The above equation is applied to the four elements surrounded by the coils and depicted in the reluctance network, giving the following reluctances

$$R_{air1} = \frac{x}{\mu_0 \pi r_i^2} \qquad R'_{air1} = \frac{\tau_w - x}{\mu_0 \pi r_i^2} \tag{A.6}$$

$$R_{air2} = \frac{\tau_w - x}{\mu_0 \pi (r_i^2 - r_m^2)} \qquad R'_{air2} = \frac{x}{\mu_0 \pi (r_i^2 - r_m^2)} \tag{A.7}$$

$$R_p = \begin{cases} \dfrac{2\tau_f - x}{\mu_0 \mu_{Fe} \pi r_m^2}, & 0 \le x \le \tau_f \\ \dfrac{\tau_f}{\mu_0 \mu_{Fe} \pi r_m^2}, & \tau_f < x \le \tau_w - \tau_f \\ \dfrac{\tau_w - x}{\mu_0 \mu_{Fe} \pi r_m^2}, & \tau_w - \tau_f < x \le \tau_w \end{cases} \quad R'_p = \begin{cases} \dfrac{x}{\mu_0 \mu_{Fe} \pi r_m^2}, & 0 \le x \le \tau_f \\ \dfrac{\tau_f}{\mu_0 \mu_{Fe} \pi r_m^2}, & \tau_f < x \le \tau_w - \tau_f \\ \dfrac{x - \tau_m}{\mu_0 \mu_{Fe} \pi r_m^2}, & \tau_w - \tau_f < x \le \tau_w \end{cases} \tag{A.8}$$

$$R_m = \begin{cases} \dfrac{\tau_m}{\mu_0 \mu_m \pi r_m^2}, & 0 \le x \le \tau_f \\ \dfrac{\tau_w - \tau_f - x}{\mu_0 \mu_m \pi r_m^2}, & \tau_f < x \le \tau_w - \tau_f \\ 0, & \tau_w - \tau_f < x \le \tau_w \end{cases} \quad R'_m = \begin{cases} 0, & 0 \le x \le \tau_f \\ \dfrac{x - \tau_f}{\mu_0 \mu_m \pi r_m^2}, & \tau_f < x \le \tau_w - \tau_f \\ \dfrac{\tau_m}{\mu_0 \mu_m \pi r_m^2}, & \tau_w - \tau_f < x \le \tau_w \end{cases} \tag{A.9}$$

The equivalent reluctance seen by each source (coil) is computed using

$$R_{tot} = R_{equ} + R'_{equ} = R_{air1} + \left(\frac{1}{R_{air2}} + \frac{1}{R_p + R_m} \right)^{-1} + R'_{air1} + \left(\frac{1}{R'_{air2}} + \frac{1}{R'_p + R'_m} \right)^{-1} \tag{A.10}$$

which give the following equivalent reluctances

$$R_{Equ} = \begin{cases} \dfrac{x}{\mu_0 \pi r_i^2} + \dfrac{\tau_w - x}{\mu_0 \pi} \left(\dfrac{\left(\dfrac{\tau_m}{\mu_m} + \dfrac{2\tau_f - x}{\mu_{Fe}} \right)}{(\tau_w - x) r_m^2 + (r_i^2 - r_m^2) \left(\dfrac{\tau_m}{\mu_m} + \dfrac{2\tau_f - x}{\mu_{Fe}} \right)} \right), & 0 \le x \le \tau_f \\ \dfrac{x}{\mu_0 \pi r_i^2} + \dfrac{\tau_w - x}{\mu_0 \pi} \left(\dfrac{\left(\dfrac{\tau_w - \tau_f - x}{\mu_m} + \dfrac{\tau_f}{\mu_{Fe}} \right)}{(\tau_w - x) r_m^2 + (r_i^2 - r_m^2) \left(\dfrac{\tau_w - \tau_f - x}{\mu_m} + \dfrac{\tau_f}{\mu_{Fe}} \right)} \right), & \tau_f < x \le \tau_w - \tau_f \\ \dfrac{x}{\mu_0 \pi r_i^2} + \dfrac{\tau_w - x}{\mu_0 \pi} \left(\dfrac{1}{\mu_{Fe} r_m^2 + r_i^2 - r_m^2} \right), & \tau_w - \tau_f < x \le \tau_w \end{cases} \tag{A.11}$$

$$R'_{Equ}=\begin{cases}\dfrac{\tau_w-x}{\mu_0\pi\, r_i^2}+\dfrac{x}{\mu_0\pi}\left(\dfrac{1}{\mu_{Fe}r_m^2+(r_i^2-r_m^2)}\right), & 0\le x\le \tau_f \\ \dfrac{\tau_w-x}{\mu_0\pi\, r_i^2}+\dfrac{x}{\mu_0\pi}\left(\dfrac{\left(\dfrac{x-\tau_f}{\mu_m}+\dfrac{\tau_f}{\mu_{Fe}}\right)}{xr_m^2+(r_i^2-r_m^2)\left(\dfrac{x-\tau_f}{\mu_m}+\dfrac{\tau_f}{\mu_{Fe}}\right)}\right), & \tau_f < x\le \tau_w-\tau_f \\ \dfrac{\tau_w-x}{\mu_0\pi\, r_i^2}+\dfrac{x}{\mu_0\pi}\left(\dfrac{\left(\dfrac{\tau_m}{\mu_m}+\dfrac{x-\tau_m}{\mu_{Fe}}\right)}{xr_m^2+\left(r_i^2-r_m^2\right)\left(\dfrac{\tau_m}{\mu_m}+\dfrac{x-\tau_m}{\mu_{Fe}}\right)}\right), & \tau_w-\tau_f < x\le \tau_w\end{cases} \tag{A.12}$$

The above equivalent reluctances are simplified using the approximations $r_i \approx r_m$ and $\mu_m \approx 1$ which results in the total reluctance for each coil

$$R_{tot}=\frac{2\tau_w-2\tau_f+\dfrac{2\tau_f}{\mu_{Fe}}}{\mu_0\pi\, r_i^2} \tag{A.13}$$

thus the total inductance of the device is the sum of the inductance of each coil since they are connected in series

$$L_{tot}=\frac{2N^2}{R_{tot}}=\frac{p}{2}\frac{\mu_0\mu_{Fe}\pi r_i^2N^2}{\tau_f+\mu_{Fe}\left(\tau_w-\tau_f\right)} \tag{A.14}$$

Appendix B Review of Structural Dynamic Response Analysis

The dynamic response of a structure with the system equation described by

$$\mathbf{M}\ddot{\mathbf{x}} + \mathbf{C}\dot{\mathbf{x}} + \mathbf{K}\mathbf{x} = \mathbf{P} \tag{B.1}$$

to a given excitation profile $\mathbf{P}$ can be predicted by solving the given matrix differential equation. The non-homogeneous solution of this equation will depend on the form of the excitation signal. Two general approaches are used to solve the dynamic equation: frequency domain methods and time domain methods. In the following sections, modal analysis, a frequency method, and time-domain state-space analysis are reviewed in this section from the analysis point of view. We are only concerned with the dynamic response of the structure, and it is assumed that the parameters of the structure were established previously. The reader is directed to the literature (for example (Connor 2003)) for information regarding the determination of the structural parameters from the desired structural response.

B.1 Modal Analysis

Modal analysis is a frequency method of analysis the response of a structure. The dynamic response of a structure is characterized in terms of the maximum values attained by the variables of interest due a particular excitation (Buchholdt 1997).

B.1.1 Natural Frequencies and Mode Shapes

Each degree of freedom in a structure has an associated natural frequency and a characteristic mode shape, or vibration mode. The determination of these quantities is done by finding the eigenvalues and eigenvectors associated with system of equations that define its un-damped motion. The square roots of the eigenvalues λ_i give the natural angular frequencies ω_i of the structure, while the eigenvectors represent the mode-shapes Φ_i associated with each natural frequency. For an *n*-dof structure, the *n* eigenvalues of the system are found by solving the characteristic equation

$$\det\left(\mathbf{K} - \lambda\mathbf{M}\right) = 0 \tag{B.2}$$

where $\mathbf{M}$ is the mass matrix and $\mathbf{K}$ is the stiffness matrix of the structure. The damping matrix $\mathbf{C}$ is neglected because it has no effect on the natural frequencies of the structure.

The eigenvectors are defined by the following equation

$$\lambda_o \Phi_i = \mathbf{M}^{-1}\mathbf{K}\Phi_i \tag{B.3}$$

The determination of the eigenvectors is not a trivial task, especially for higher order system. Various analytical and numerical procedures for determining the eigenvectors (mode shapes) are covered in detail in the dynamics and control literature, for example (Beards 1996; Buchholdt 1997; Cheng 2001). In the discussion the follows, it is presumed that the mode shapes and corresponding modal frequencies are known.

B.1.2 Steady-State Harmonic Solution

Once the natural frequencies and corresponding mode shapes are determined, the response of the system is found by solving uncoupled differential equations of motion, one for each mode. The total response of the structure is obtained by superposition of these solutions or modal responses to the driving signal, hence the term modal analysis.

The coupled differential equations of motion for an *n*-dof system are uncoupled by means of a space transformation from $\mathbf{x}$ to $\mathbf{q}$ defined by

$$\mathbf{x} = \mathbf{\Phi q},\ \dot{\mathbf{x}} = \mathbf{\Phi}\dot{\mathbf{q}},\ \ddot{\mathbf{x}} = \mathbf{\Phi}\ddot{\mathbf{q}} \tag{B.4}$$

where $\mathbf{\Phi} = \left[\mathbf{\Phi}_1 \mid \mathbf{\Phi}_2 \mid \cdots \mid \mathbf{\Phi}_n\right]$ is the mode shape matrix. Substituting equation (B.4) into (B.1) and pre-multiplying by $\mathbf{\Phi}^T$ gives the uncoupled set of equations of motion in terms of the modal displacements $\mathbf{q}$

$$\widetilde{\mathbf{M}}\ddot{\mathbf{q}} + \widetilde{\mathbf{C}}\dot{\mathbf{q}} + \widetilde{\mathbf{K}}\mathbf{q} = \mathbf{\Phi}^T\mathbf{P} \tag{B.5}$$

where the terms $\widetilde{\mathbf{M}} = \mathbf{\Phi}^{\mathbf{T}}\mathbf{M}\mathbf{\Phi}$, $\widetilde{\mathbf{K}} = \mathbf{\Phi}^{\mathbf{T}}\mathbf{K}\mathbf{\Phi}$, and $\widetilde{\mathbf{C}} = \mathbf{\Phi}^{\mathbf{T}}\mathbf{C}\mathbf{\Phi}$ are referred to as the modal mass, modal stiffness, and modal damping matrices, respectively. Since the mode shape matrix is composed of the eigenvectors that are orthogonal to each other, the modal matrices are diagonal matrices.

The problem now reduces to solving *n* second order differential equations independently and then obtaining the complete response by applying equation (B.4) to the resulting modal position vector $\mathbf{q}$. Each modal equation is of the form

$$\widetilde{m}_i \ddot{q}_i + \widetilde{c}_i \dot{q}_i + \widetilde{k}_i q_i = \mathbf{\Phi}_i^T \mathbf{P} \tag{B.6}$$

If we divide by the modal mass we can express the each equation in terms of the natural frequency ω_i and the damping coefficient ξ_i of the i^{th} mode

$$\ddot{q}_i + 2\xi_i \omega_i \dot{q}_i + \omega_i^2 q_i = \mathbf{Z}_i^T \mathbf{P} = f_i \tag{B.7}$$

which is the canonical form a the second order equation, where $\omega_i^2 = \widetilde{k}_i / \widetilde{m}_i$ and $2\xi_i \omega_i = \widetilde{c}_i / \widetilde{m}_i$.

The solution to (B.7) is composed of a homogeneous or transient component which depends on the initial conditions, and a particular or forced response component which depends on the driving force f_i.

When the forcing term is sinusoidal in form, that is $f_i = \vec{f} \sin(\omega t)$ then the solution is

$$q_i = e^{-\xi_i \omega_i t}\left(F_1 e^{j\omega_i \sqrt{1-\xi_i^2}\, t} + F_2 e^{-j\omega_i \sqrt{1-\xi_i^2}\, t} \right) + h_i(\omega) f_i \sin\left(\omega t + \alpha_i(\omega)\right) \tag{B.8}$$

The first term is the transient component where the constants F_1 and F_2 depend on initial conditions ($j = \sqrt{-1}$). The second term is the forced component. Neglecting the transient term, the response of the mode is given by

$$q_i = h_i(\omega) f_i \sin\left(\omega t + \alpha_i(\omega)\right) \tag{B.9}$$

where the functions $h_i(\omega)$ and $\alpha_i(\omega)$ are given by

$$h_i(\omega) = \frac{1}{\omega_i^2 \sqrt{\left(1 - (\omega/\omega_i)^2\right)^2 + \left(2\xi_i \omega/\omega_i\right)^2}} \tag{B.10}$$

$$\alpha_i(\omega) = \tan^{-1}\left(\frac{2\xi_i \omega/\omega_i}{1 - (\omega/\omega_i)^2} \right) \tag{B.11}$$

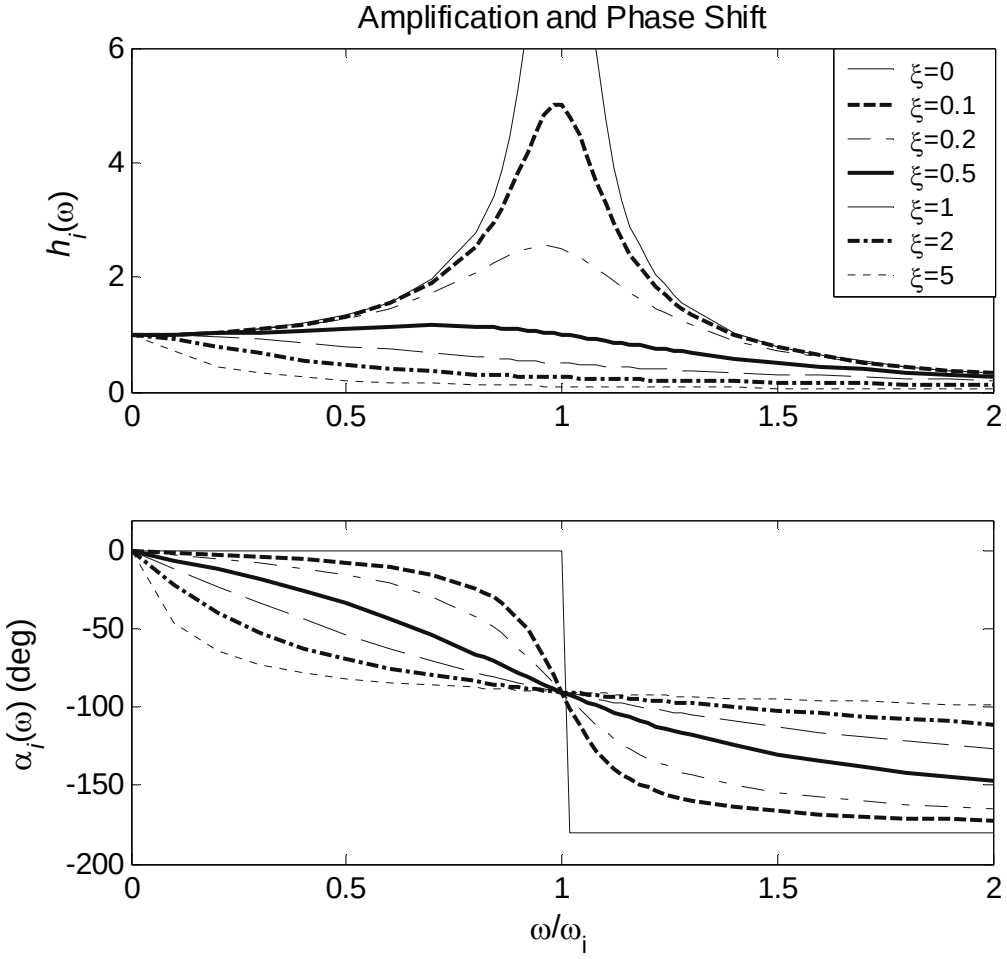

Figure B.1 Modal Sinusoidal Steady-State Response vs. Frequency and Damping Coefficient.

Another interpretation of the functions $h_i(\omega)$ and $\alpha_i(\omega)$ is as the magnitude and phase, respectively, of the i^{th} mode transfer function. Their variation with respect of the normalized frequency ω/ω_i and the nodal damping coefficient is shown in Figure B.1.

The steady-state response of a structure to an input to which the spectra is known can therefore be calculated by computing the value of the transfer function ($h_i(\omega)$ and $\alpha_i(\omega)$) at the spectra frequencies for each of the modes and obtaining the corresponding modal displacement using equation (B.9). The actual structure displacements are then computed with equation (B.4).

B.2 Time-Domain State Space Analysis

B.2.1 State-Space Definition

A common way to model dynamic systems is by using state-space equations. In this approach, the mathematical representation of the process or system under study is by a set of first order differential equations (Friedland 1986). When the system of interest is a linear system, these equations can be written in matrix form as

$$\begin{aligned} \dot{\mathbf{x}} &= \mathbf{A}\mathbf{x} + \mathbf{B}\mathbf{u} \\ \mathbf{y} &= \mathbf{C}\mathbf{x} + \mathbf{D}\mathbf{u} \end{aligned} \tag{B.12}$$

where $\mathbf{x} = \begin{bmatrix} x_1 & x_2 & \cdots & x_n \end{bmatrix}^T$ is the system state vector, $\mathbf{u} = \begin{bmatrix} u_1 & u_2 & \cdots & u_m \end{bmatrix}^T$ is the input vector, and $\mathbf{y} = \begin{bmatrix} y_1 & y_2 & \cdots & y_k \end{bmatrix}^T$ the output vector. For the case of time-invariant systems, the matrices $\mathbf{A}$, $\mathbf{B}$, $\mathbf{C}$ and $\mathbf{D}$ are constant matrices of dimension $n \times n$, $n \times m$, $k \times n$, and $k \times m$, respectively. The plant and input matrices, $\mathbf{A}$ and $\mathbf{B}$ respectively, are the ones that determine the dynamic response of the system. The matrix $\mathbf{C}$ represents the effect of the state on the outputs and is called the observation matrix, while the matrix $\mathbf{D}$ quantifies the direct connection between the inputs and the outputs. Both $\mathbf{C}$ and $\mathbf{D}$ have no effect on the dynamic response of the system and thus it will be neglected in the discussion that follows.

The state vector $\mathbf{x}$ is a set of physical quantities that, in the absence of external excitation, completely determines the behavior of the system over time from an initial condition. The number of state variables in a given system is fixed, and is know as the order of the system; their choice is not unique and is normally determined by the quantities that are of interest in the system under examination.

B.2.2 State Space Time-Domain Solution

The state $\mathbf{x}$ of the system represented by equation (B.12) at some time t is determined by the initial state $\mathbf{x}_0$ at some time τ and the input $\mathbf{u}(t)$. The solution of $\mathbf{x}(t)$ is a function of the state-transition matrix $S(t,\tau)$. When the system is linear-time-invariant (a reasonable assumption for structural systems), $S(t,\tau) = e^{\mathbf{A}(t-\tau)}$, and the state solution is

$$\mathbf{x}(t) = e^{\mathbf{A}(t-\tau)}\mathbf{x}_0 + \int_\tau^t e^{\mathbf{A}(t-\lambda)}\mathbf{B}\mathbf{u}(\lambda)d\lambda \tag{B.13}$$

where $e^{\mathbf{A}t}$ is the matrix exponential function defined as $e^{\mathbf{A}t} = \sum_{k=0}^{\infty} \mathbf{A}^k \frac{t^k}{k!}$.

The reader is directed to the literature (Friedland 1986) or (Nise 2002) for a detailed derivation of the above result, and for a description of methods available to evaluate the solution of the state-space system.

B.3 Structural Representation in State-Space Form

For an *n*-dof structural system, a convenient choice of state variables are the position and the velocity of each of the lumped masses, which results in a system of order 2*n*. This choice of variables provides a straight forward conversion of the equations of motion into state-space form.

If we consider the equation of motion for the i^{th} mass,

$$m_i\ddot{x}_i + (c_i + c_{i+1})\dot{x}_i - c_i\dot{x}_{i-1} - c_{i+1}\dot{x}_{i+1} + (k_i + k_{i+1})x_i - k_i x_{i-1} - k_{i+1}x_{i+1} = p_i \tag{B.14}$$

the first "obvious" choice of state variables are $x_{2i-1} = x_i$ and $x_{2i} = \dot{x}_i$. With this choice, the state equations are

$$\begin{cases} \dot{x}_{2i-1} = x_{2i} \\ \dot{x}_{2i} = \frac{k_i}{m_i}x_{2i-3} + \frac{c_i}{m_i}x_{2i-2} - \frac{(k_i + k_{i+1})}{m_i}x_{2i-1} - \frac{(c_i + c_{i+1})}{m_i}x_{2i} + \frac{k_{i+1}}{m_i}x_{2i+1} + \frac{c_{i+1}}{m_i}x_{2i+2} + p_i \end{cases} \tag{B.15}$$

We see that in the second equation above, the stiffness and damping terms are interleaved when the state variables are arranged sequentially. A more convenient choice of state variables is obtained grouping the position and velocities together such that the stiffness and damping coefficients are clustered together. This choice of state variables are $x_i = x_i$ and $x_{i+n} = \dot{x}_i$, and the state equation for the i^{th} mass are then

$$\begin{cases} \dot{x}_i = x_{i+n} \\ \dot{x}_{i+n} = \dfrac{k_i}{m_i} x_{i-1} - \dfrac{(k_i + k_{i+1})}{m_i} x_i + \dfrac{k_{i+1}}{m_i} x_{i+1} + \dfrac{c_i}{m_i} x_{i+n-1} - \dfrac{(c_i + c_{i+1})}{m_i} x_{i+n} + \dfrac{c_{i+1}}{m_i} x_{i+n+1} + p_i \end{cases} \tag{B.16}$$

Grouping the state equations for the n masses, and taking the force vector $\mathbf{P}$ as the input vector results in the state space representation of the *n*-dof structure:

$$\begin{bmatrix} \dot{\mathbf{x}} \\ \ddot{\mathbf{x}} \end{bmatrix} = \left[\begin{array}{c|c} \mathbf{0} & \mathbf{I} \\ \hline -\mathbf{M}^{-1}\mathbf{K} & -\mathbf{M}^{-1}\mathbf{C} \end{array}\right] \begin{bmatrix} \mathbf{x} \\ \dot{\mathbf{x}} \end{bmatrix} + \begin{bmatrix} \mathbf{0} \\ \hline \mathbf{M}^{-1} \end{bmatrix} \mathbf{P} \tag{B.17}$$

where the state matrix $\mathbf{A}$ is constructed with the matrices $\mathbf{M}$, $\mathbf{C}$ and $\mathbf{K}$. These are the mass, damping and the stiffness matrices used previously in equation (B.1). Notice that if we pre-multiply the second matrix row in the above equation by $\mathbf{M}$ we obtain equation (B.1).

The state of the structure, that is the position and velocities of the floors at any instant t, due to an excitation $\mathbf{P}$ is found by applying equation (B.13) to the state-space system defined by (B.17). Typically, this operation is performed numerically or by frequency transformation methods (such a Laplace and Fourier methods). The reader is directed to the dynamics and control literature, for example (Friedland 1986) or (Nise 2002) for a detailed explanation of these methods.

Appendix C System Parameters and Descriptions

C.1 Baldor Linear Motor Datasheet

BALDOR
MOTORS AND DRIVES
LINEAR MOTION PRODUCTS

NON COMMUTATED DC LINEAR MOTOR TEST DATA SHEET

CUSTOMER: MOTION INDUSTRIES INC DATE: 02/23/05

DCLM P/N: NC0013A01 S/O # : 95417184

HYPOT 250V BETWEEN 2 LEADS AND CASE. Rc = 4.00 OHMS

I (AMPS)	R (OHMS)	F (LBS)	PIN (WATTS)	KM (LBS/ SQRT (WATT))
1.00	3.89	1.76	3.89	0.89

Km = 0.89 LBS/ SQRT(WATT) MOVING MASS = _____ OZ

F/I = 1.78 LBS/AMP STATION. MASS = _____ OZ

E/V = 0.20 VOLTS/I.P.S. Do = N/A

t = 0.51 mSEC Lo = N/A

L = 2.03 mH MISC. = _____

Pth = N / A WATTS _____

NAMEPLATE:

1.5	100	300905
AMPS	% DUTY	SERIAL

NC0013A01
MODEL

TESTED BY: EDDIE DUQUE
ON: 02/23/05

25026 ANZA DRIVE
SANTA CLARITA, CA
U.S.A.

PHONE: .(661)257-0216
FAX: (661)257-2037

:/c20svr/testing department/ncdclm test reports/300905 rev. 1.0 2/23/2005

Figure C.1 Baldor™ Test Data Sheet

Non-Commutated Moving Magnet Technical Data

Parameters	Units	Catalog Number LMNM2-F8-F6	LMNM2-1F3-F2	LMNM2-1F5-F8	LMNM2-1F5-1F1
General:					
Stroke	in [mm]	0.600 [15.2]	0.250 [6.4]	0.750 [19.1]	1.125 [28.6]
Continuous Force	lbs [N]	0.5 [3]	1.9 [9]	2.5 [12]	2.5 [12]
Continuous Current	Amps	0.87	1.02	0.86	1.47
Peak Force® 10% Duty	lbs [N]	1.5 [7]	5.7 [26]	7.5 [34]	7.5 [34]
Peak current @ 10% Duty	Amps	2.6	3.1	2.6	4.4
Continuous Power	Watts	2	10	10	9
Mechanical:					
No. of poles		2	2	2	2
Motor moving weight	lbs [kg]	0.050 [0.030]	0.100 [0.050]	0.313 [0.150]	0.486 [0.230]
Motor total weight	lbs [kg]	0.163 [0.080]	0.800 [0.370]	1.110 [0.510]	1.280 [0.590]
Bearing Type		Jewel Sapphire	Ball Bushing	Ball Bushing	Ball Bushing
Electrical:					
Force Constant Ph to Ph	lbs[N]/amps	0.58 [2.6]	1.87 [8.3]	2.91 [13.0]	1.70 [7.6]
Back EMF Constant Ph to Ph	V/in/s [V/m/s]	0.07 [2.6]	0.21 [8.3]	0.33 [13.0]	0.19 [7.6]
Resistance Ph to Ph at 25°C	Ohms	3.2	9.7	13.6	4
Resistance Ph to Ph at 125°C	Ohms	4.5	13.5	2.7	5.6
Inductance Ph to Ph	mH	0.225	0.9	0.9	1.52
Electrical Time Constant	msec	0.070	0.093	0.066	0.380
Km Motor Constant	lbs[N]/√W	0.32 [1.44]	0.60 [2.67]	0.79 [3.51]	0.85 [3.78]

Parameters	Units	Catalog Number LMNM2-1F5-2	LMNM4-F5-F2	LMNM4-2F8-F5	LMNM9-2F8-F5
General:					
Stroke	in [mm]	2.000 [50.8]	0.150 [3.8]	0.500 [12.7]	0.500 [12.7]
Continuous Force	lbs [N]	2 [9]	0.5 [3]	25 [112]	50 [223]
Continuous Current	Amps	2.28	0.45	2.47	4.62
Peak Force® 10% Duty	lbs [N]	6 [27]	1.5 [7]	75 [334]	150 [668]
Peak current @ 10% Duty	Amps	6.8	1.4	7.4	13.9
Continuous Power	Watts	25	3	54	81
Mechanical:					
No. of poles		2	4	4	9
Motor moving weight	lbs [kg]	0.705 [0.330]	0.022 [0.010]	3.440 [1.570]	5.510 [2.510]
Motor total weight	lbs [kg]	2.275 [1.040]	0.040 [0.020]	10.340 [4.700]	16.540 [7.510]
Bearing Type		Ball Bushing	Jewel Sapphire	Ball Bushing	Ball Bushing
Electrical:					
Force Constant Ph to Ph	lbs[N]/amps	0.88 [3.9]	1.11 [4.9]	10.11 [45.0]	10.81 [48.1]
Back EMF Constant Ph to Ph	V/in/s [V/m/s]	0.10 [3.9]	0.12 [4.9]	1.14 [45.0]	1.22 [48.1]
Resistance Ph to Ph at 25°C	Ohms	4.8	13.6	8.9	3.8
Resistance Ph to Ph at 125°C	Ohms	6.7	18.9	12.4	5.3
Inductance Ph to Ph	mH	2.32	0.9	0.9	2.2
Electrical Time Constant	msec	0.483	0.066	0.101	0.579
Km Motor Constant	lbs[N]/√W	0.40 [1.78]	0.30 [1.33]	3.39 [15.08]	5.55 [24.67]

NOTES: 1. All specifications are for reference only.
2. Motors listed above are only a sample of Baldor extensive array of Non-Commutated DC Linear Motors.
3. Non-Commutated DC linear motors can be customized to meet any specific requirements.

Figure C.2 Linear Motors Baldor Electric Co. Catalog Data Sheet (2005).

C.2 Velocity Excitation Experimental Setup

C.2.1 Velocity Control System Description

The system used to drive the damper under a prescribed velocity is described by Figure C.3. A detailed description from the experiment's point of view was given in section §7.4. The description from the control point of view is given here.

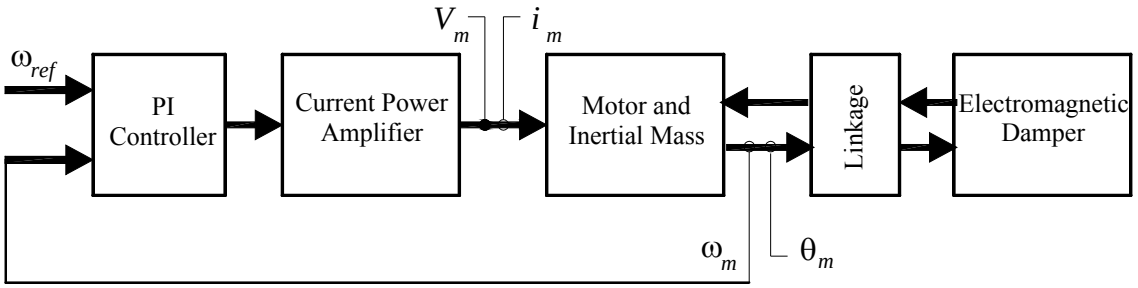

Figure C.3 Experimental Set-up Relational Block Diagram.

To perform the system simulation, the components of the experimental setup are modeled using transfer functions, which are derived from the device time-domain equations (differential equations) using the Laplace Transform (Nise 2002). In a transfer function model, the output of a system is expressed as the multiplication of the input by a function of complex frequency (s). The system is then described using interconnected blocks (Figure C.4), where the input of one block is the output of another (or a linear combination of others).

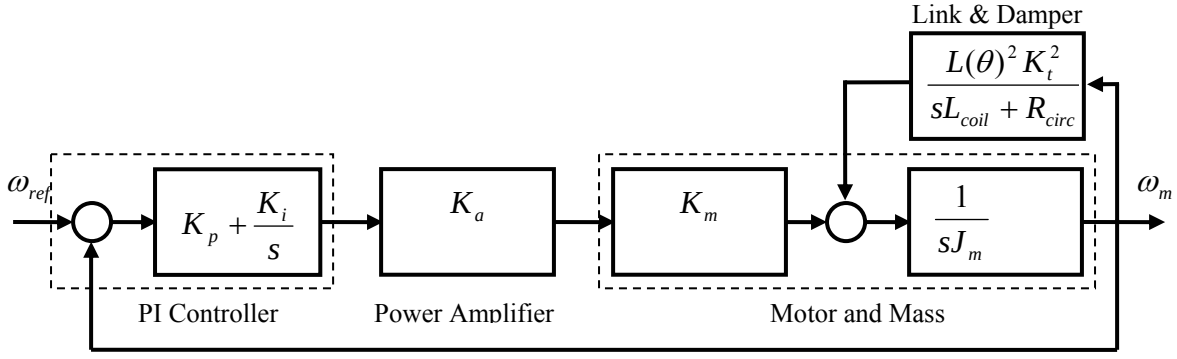

Figure C.4 Experimental Set-up Signal Block Diagram.

The governing differential equations and corresponding transfer functions for the control system components are presented in Table C.1. Since the linkage mechanism is a transformer that inter-

faces the rotational and linear mechanical domains, it is treated as a time varying (dependent on θ) coefficient of the damper equation.

Table C.1 Experimental Setup Components Equations

Component	Input/Output	Constitutive Relation	
		Time Domain Function	Transfer Function
PI Controller	$e = \omega_{ref} - \omega_m$ V_c	$V_c = K_p e + K_i \int_0^t e d\tau$	$\frac{V_c}{E} = K_p + \frac{K_i}{s}$
Power Amplifier	V_c i_m	$i_m = K_a V_c$	$\frac{I_m}{V_c} = K_a$
DC Motor	i_m τ_m	$\tau_m = K_m i_m$	$\frac{\mathrm{T}_m}{I_m} = K_m$
Inertial Mass	$\tau_m - \tau_d$ ω_m	$J_m \dot{\omega}_m = \tau_m - \tau_d$	$\frac{\Omega_m}{\mathrm{T}_m} = \frac{1}{sJ_m}$
EM Damper	$v = -L(\theta)\omega_m$ $\tau_d = -L(\theta)F_d$	$L_{coil}\frac{\dot{\tau}_d}{L(\theta)} + \frac{\tau_d}{L(\theta)}\left(R_{coil} + R_{load}\right) = -L(\theta)K_t^2\omega_m$	$\frac{\tau_d}{\omega_m} = -\frac{L(\theta)^2 K_t^2}{sL_{coil} + R_{coil} + R_{load}}$
Linkage	Coefficient	$L(\theta) = r\sin\theta\left(1 + \frac{r\cos\theta}{\sqrt{l^2 + (r\sin\theta)^2}}\right)$	N/A

Table C.2 Experimental Setup Components Parameter Values.

Subsystem	Constant	Value	Description
PI Controller	K_i	100	Integral Gain
	K_p	10	Proportional Gain
Power Amp. And Motor	K_a	2 A/V	Amplifier Gain
	K_m	0.17 Nm/A	Motor Torque Constant
	J_m	$3.8\text{x}10^{-4}$ Kgm^2	Inertial Mass
Electromagnetic Damper	K_t	7.9 N/A	Force Constant
	L_{coil}	2.03 mH	Coil Inductance
	R_{coil}	3.89 Ω	Coil Resistance
	R_{load}	0 Ω	Load Resistance
Linkage	r	12 mm	Linkage Radius
	l	52 mm	Linkage Length

The system is simulated using Simulink®, a component of Matlab®, for a constant reference angular velocity. The Simulink diagram is shown in Figure C.5, while sample results of the simulation for two sets of controller gains are shown in Figure C.6 and Figure C.7. The values for the system parameters used in the simulation are shown Table C.2.

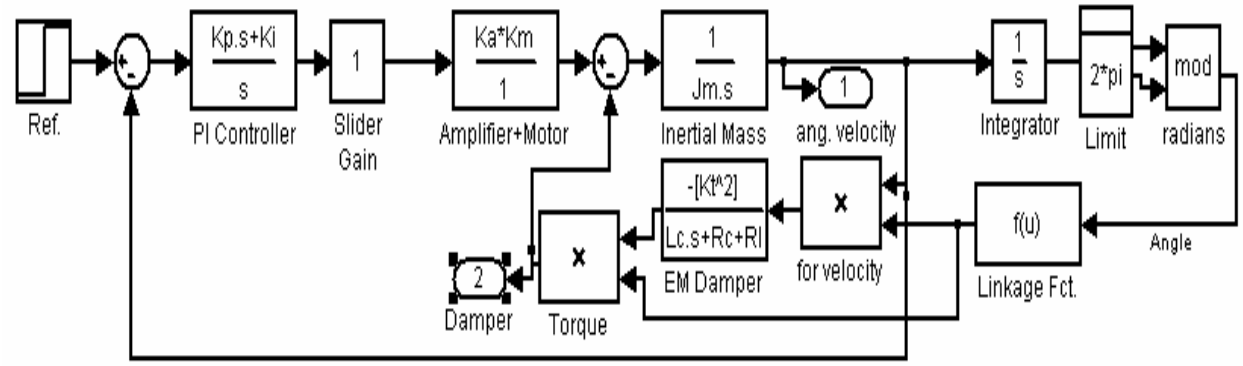

Figure C.5 Simulink® Model Diagram of the Control System.

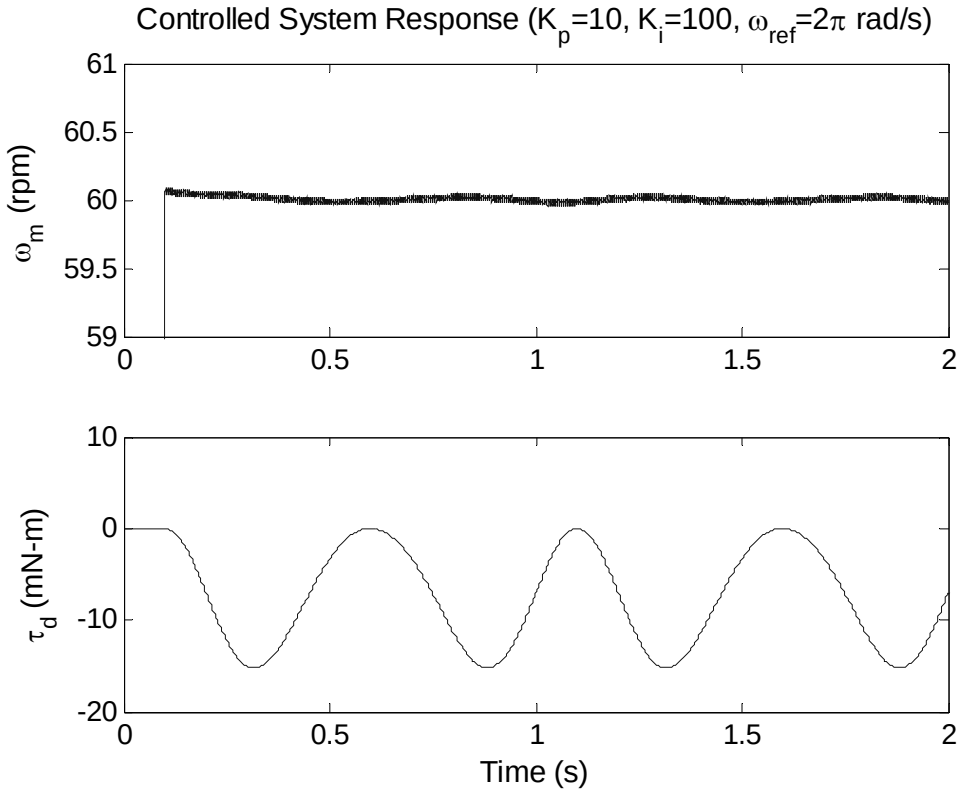

Figure C.6 Velocity and Torque Response for Controlled System (High Gains).

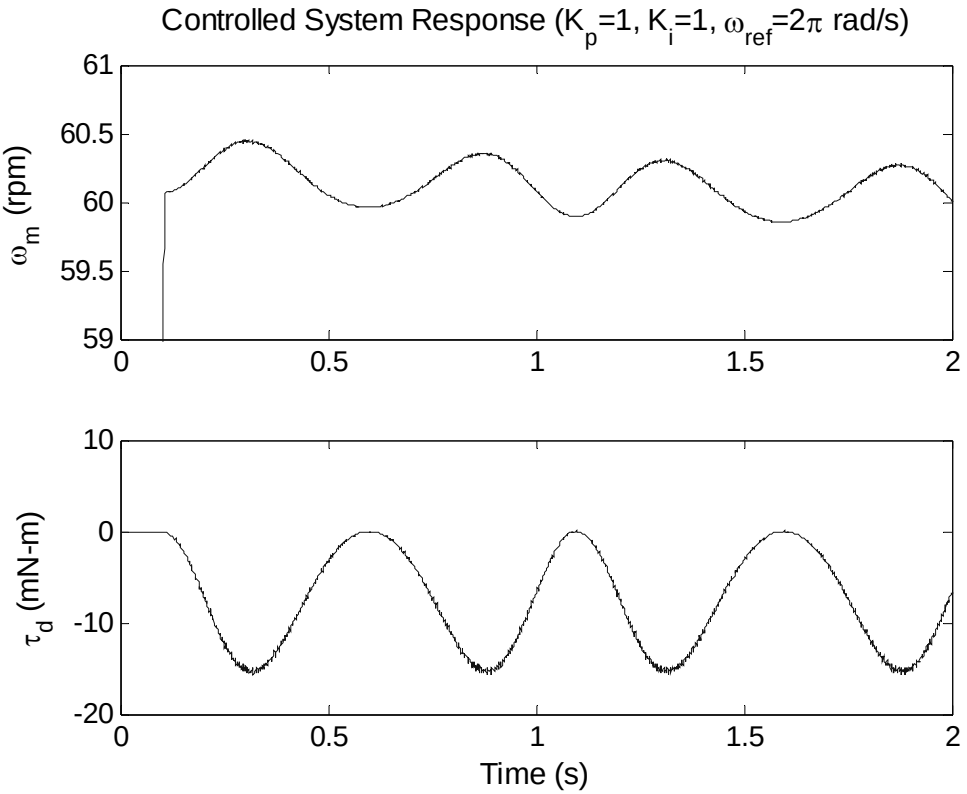

Figure C.7 Velocity and Torque Response for Controlled System (Low Gains)

C.2.2 PI Controller Circuit Diagram

Figure C.8 shows the circuit that implements the PI controller described previously. Table C.3 presents the components values of the circuit below.

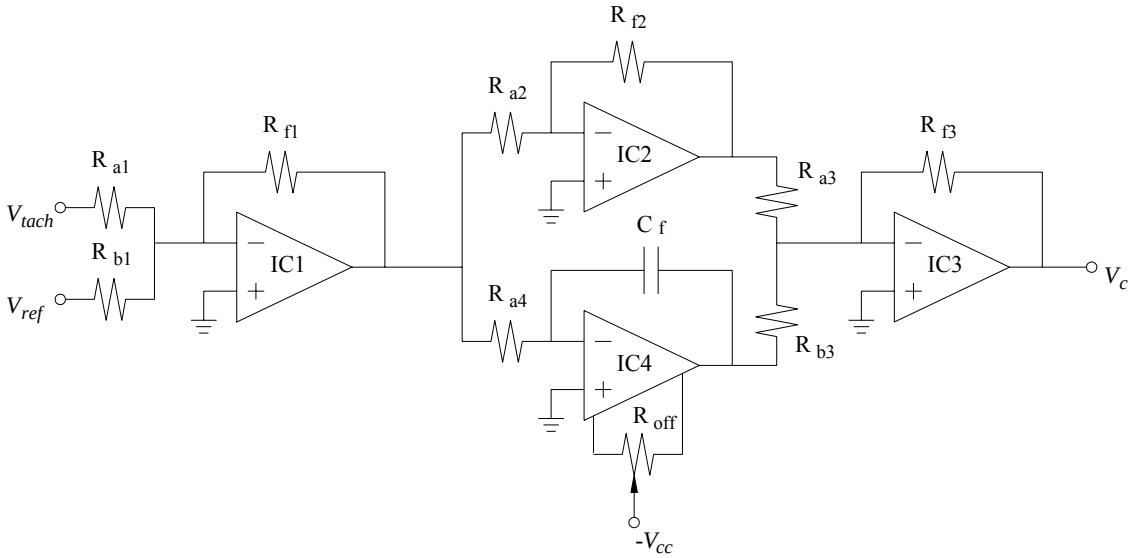

Figure C.8 Controller PI Controller Circuit Diagram.

Table C.3 PI Controller Component Values.

Sub-System	Component	Value
Error Summer	IC1	LM3403 (1/4)
	R_{a1}	10kΩ
	R_{b1}	10kΩ
	R_{f1}	1kΩ
Proportional Gain	IC2	LM3403 (2/4)
	R_{a2}	1kΩ
	R_{f2}	10kΩ
Integral Gain	IC4	LM741
	R_{a4}	10kΩ
	C_f	10□F
	R_{off}	100kΩ Pot
Output Summer	IC3	LM3403 (3/4)
	R_{a3}	10kΩ
	R_{b3}	10kΩ
	R_{f3}	100kΩ

C.2.3 Honeywell Tension/Compression Miniature Load Cell

The calibration values provided by the manufacturer are presented in Table C.4. Figure C.9 shows the diagrams of the 5V supply and signal conditioning circuits. An instrumentation amplifier with a gain of 1000 was used to interface the load cell to the analog-to-digital converter.

Table C.4 Load Cell Calibration Parameters

Parameter	Value
Excitation	5 V
Calibration Factor	2.054 mv/V
FS Range	10 lbs (44.48 N)
Input Resistance	355 Ω
Output Resistance	354 Ω

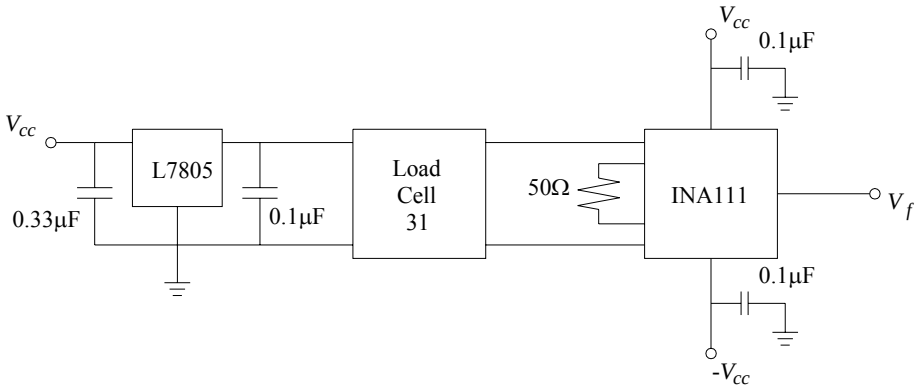

Figure C.9 Load Cell Supply and Signal Conditioning Circuit Diagram.

Appendix D The Parasitic Damping Coefficient

When the load resistance is set to an open circuit, the electromagnetic damper does not contribute to the system damping; therefore the system equation, setting the spring constant to zero, reduces to

$$m\ddot{x} + c_f \dot{x} = mg \tag{D.1}$$

The solution to equation (D.1), given zero initial conditions, is

$$x(t) = g\left(\frac{m}{c_f}\right)^2 e^{-\frac{c_f}{m}t} + g\frac{m}{c_f}t - g\left(\frac{m}{c_f}\right)^2 \tag{D.2}$$

The solution (D.2) and its components are plotted in Figure D.1. It can be seen from the figure that the solution approximates the straight line equation as the exponential component dies off.

The parasitic damping coefficient can thus be estimated from the experimental data by estimating the slope of the curve, after allowing the exponential component to decay. A linear regression fit is performed on the "straight" part of the data curve.

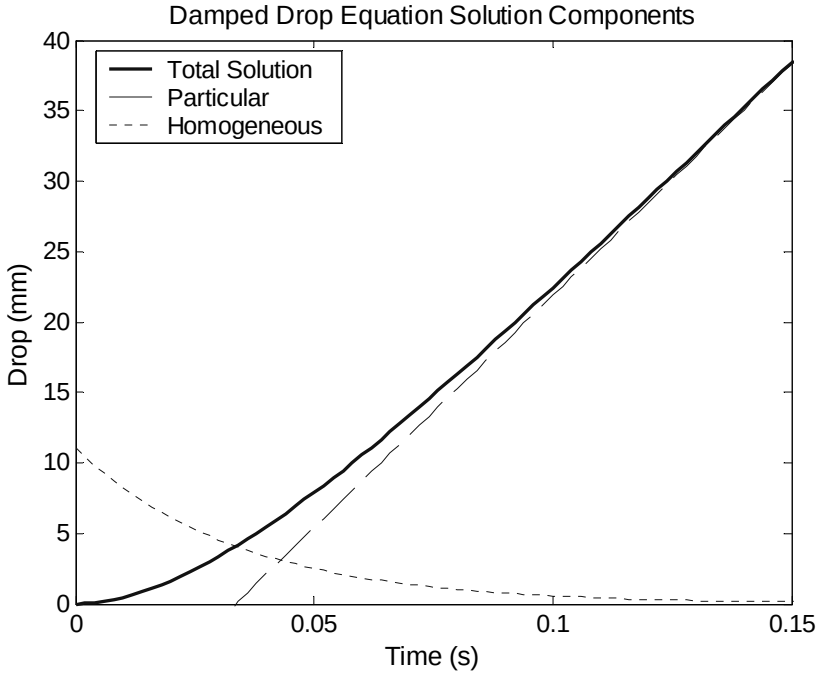

Figure D.1 Components of the Damped Drop Solution without EM Damping.

Appendix E Matlab® Code and Data

E.1 Feasibility Study Code

```
function output=feasibility(Folder)

% Function to generate data to study the feasibility of the electro-
magnetic
% damper.  Files for each of the values of magnet radius, air gap
thickness
% and magnet lenght are gemerated.  Each file contains the damper
desing and
% analysis paramaters for at each value of coil wire diameter and coil
% layers.
%
%
% (c) July 2005 Rogelio Palomera-Arias
output=0;
strokes=.005:.0025:.25;     % Magnet legnths=strokes (m)
gaps=.25e-3:.05e-3:5e-3;    %  Air Gaps {m}
rm=(.2:.1:15)'*1e-2;        % Radius of axial magnet {m}
awg=0:40;                   % AWG wire numbers
Nr=(1:30)';                 % Number of layers in coil
h=waitbar(0,'Processing');
iter=length(strokes)*length(gaps)*length(rm);
for indexs=1:length(strokes)
    for indexg=1:length(gaps)
        for indexr=1:length(rm)
            waitbar(indexs*indexg*indexr/iter,h)
            [DimensionPa-
ram,DampingParam,CostParam,OperationPoint]=AnalyzeMachine(rm(indexr),s
trokes(indexs),gaps(indexg),awg,Nr);

            File-
name=sprintf('h:/%s/FeasibilityR%dG%dS%d',Folder,indexr,indexg,indexs)
;
            save(Filename);
            output=output+1;
        end
    end
end
close(h);

function [DimensionPa-
ram,DampingParam,CostParam,OperationPoint]=AnalyzeMachine(rm,Taum,g,aw
g,Nr)
```

```
% Function to generate the machine design and analysis parameters
given the magnet radius,
% length, air gap, coil wire radius and number of coil layers.
%
% (c) July 2005 Rogelio Palomera-Arias

%%%%%%%%%%%%%%%% Material Properties%%%%%%%%%%%%%%%%
Mu0=pi*4e-7;                % Permeability of free space
% NdFeB Magnet Properties (N35)
Brem=1.2;                   % Remanence {T}
Hc=900e3;                   % Coercivity {A/m}
%Brem=1.5;                   % N55 magnet
%Hc=1050e3;
Murec=Brem/Hc;              % Recoil permeability
magnet=[Brem Hc Murec/Mu0];
PriceMagnet=66;             % Price per weigth {$/kg^3}
DensityMagnet=7.5e3;        % Density (kg/m^3)
% Cu Properties
Rho=1.77e-8;                % Resisitivity {Ohms-m}
PriceCu=3;                  % Price per volume {$/kg}
DensityCu=8.9e3;            % Density (kg/m^3)
% Fe Properties
Mufe=2000;                  % Relative permeability
Bsatfe=2.0;                 % Saturation Magnetic Flux Density
PriceFe=0.5;                % Price per volume {$/kg}
DensityFe=8e3;              % Density (kg/m^3)
%%%%%%%%%%%%%%%%%%%%%%%%%%%%%%%%%%%%%%%%%%%%%%%%%%%%%%%%%%%%
%%%%%%%%%%%%%%%% Machine Design %%%%%%%%%%%%%%%%%%%%%%%%
rw=0.0254*0.46/2*0.890525.^(awg+3); % Wire radii {m}
Ro=Rho./(pi*rw.^2);         % Wire resistance {Ohms/m}
hw=((Nr-1)*sqrt(3)+2)*rw;   % Height of coil {m}
ri=rm+g;        % inside radius of coil
rs=ri+hw;     % inside radius of yoke
Tauf=Murec/Mu0*rm^2/Taum*log(rs/rm); % Width of pole shoe
Bm0=Bm_initial(rm,Taum,rs,Tauf,magnet);
hy=-rs+sqrt(rs.^2+rm^2*Bm0/(0.9*Bsatfe)); % Thickness of yoke
re=rs+hy;                % Outside radius of machine
Bm=Bm_all(rm,Taum,rs,Tauf,magnet,hy,Mufe);
Hm=(Bm-Brem)./Murec;
Bp=Bm*rm./(2*Tauf);
Bs=Bm*rm^2./(hy.*(rs+re));
[Nl,Tauw]=CoilDimension(Tauf,Taum,rw);
Nw=diag(Nr)*Nl;         % Total number of turns per coil
%%%%%%%%%%%%%%%%%%%%%%%%%%%%%%%%%%%%%%%%%%%%%%%%%%%%%%%%%%%%
%%%%%%%%%%%%%%%%%%%% Machine Analysis %%%%%%%%%%%%%%%%%%%%
% Machine constant
Kt=pi*Nw.*Bm*rm^2./Tauw;
% Coil resistance
Rcoil=Nw.*(ri+rs)*diag(Ro);
% Maximum damping coefficient
Cd=Kt.^2./Rcoil;
% Coil inductance
```

```
Lcoil=Mu0*Mufe*pi*ri^2*Nw.^2./(2*Tauf+2*Mufe*(Tauw-Tauf));
% Machine volumes
MachineVolume=pi*re.^2.*Tauw;
MagnetVolume=pi*rm^2*Taum;
PolesVolume=2*pi*rm^2*Tauf;
StatorVolume=pi*(re.^2-rs.^2).*Tauw;
CopperVolume=Rcoil*diag(1./Ro)*pi*diag(rw.^2);
% Machine prices
MagnetPrice=MagnetVolume*PriceMagnet*DensityMagnet;
FePrice=(PolesVolume+StatorVolume)*PriceFe*DensityFe;
CuPrice=CopperVolume*PriceCu*DensityCu;
MachinePrice=(MagnetPrice+FePrice+CuPrice);
% Performance Measures
DampingDensity=Cd./MachineVolume/1000;  % {kN/(m/s)/m^3}
CostDamping=MachinePrice./(Cd/1000);      % {$/(kN/(m/s))}
CostDampingDens=MachinePrice./DampingDensity;
%%%%%%%%%%%%%%%%%%%%%%%%%%%%%%%%%%%%%%%%%%%%%%%%%%%%%%%%%%%%%%%%%%%%%%%
%%%%%%%%%%%%%%%%%%%%   Output Structures %%%%%%%%%%%%%%%%%%%%
% Dimensions Parameters
DimensionParam.Diameter=2*re;
DimensionParam.Length=Tauw;
DimensionParam.Volume=MachineVolume;
DimensionParam.CoilLayers=Nr;
DimensionParam.CoilTurns=Nw;
DimensionParam.CoilWire=rw;
DimensionParam.CoilHeight=hw;
DimensionParam.YokeThickness=hy;
% Damping and Electrical Parameters
DampingParam.Kt=Kt;
DampingParam.Rcoil=Rcoil;
DampingParam.Lcoil=Lcoil;
DampingParam.Cd=Cd;
DampingParam.Density=DampingDensity;
% Cost Parameters
CostParam.Machine=MachinePrice;
CostParam.Cu=CuPrice;
CostParam.Fe=FePrice;
CostParam.Magnet=MagnetPrice;
CostParam.Damping=CostDamping;
CostParam.Density=CostDampingDens;
% Magnet and Iron Operation Point
OperationPoint.Bm=Bm;
OperationPoint.Hm=Hm;
OperationPoint.Poles=Bp;
OperationPoint.Stator=Bs;
```

E.2 Constant Force Experiment

E.2.1 Simulation Programs

```
%%%%%%%%%%%%%%%%%%%%%%%%%%%%%%%%%%%%%%%%%%%%%%%%%%%%%%
%%%  Damped Mass Drop Experiment Simulation
%%%
%%%  (c) Rogelio Palomera-Arias, March 2005
%%%%%%%%%%%%%%%%%%%%%%%%%%%%%%%%%%%%%%%%%%%%%%%%%%%%%%

%%% Linear Damper Parameters
Kte=7.874;      % Back EMF Constant   {Vs/m}
Ktf=7.918;      % Force Constant    {N/A}
Rcoil=3.89;     % Coil Resistance   {Ohms}
Lcoil=2.03e-3;  % Coil Inductance   {H}
Mm=230e-3;      % Mover mass        {Kg}
%%% Testing Parameters
T=0:0.002:0.3;
g=9.81;         % Gravity constant  {m/s^2}
Mass=[42.5 106.3 170.1 233.9]*1e-3;
Rload=[inf 10.3 5.6 0.5];
Rcirc=Rcoil+Rload;
m=Mass+Mm;
%%% Set-up Parameters
Height=24.5e-3; % Drop Height       {m}
ks=0;           % Spring Constant   {N/m}
%cfDetermineC(R0s,Time,m); % Parasitic damping {Ns/m}
cf=8.2;
%%% System Model. State Variables: x, v and Fd
B=[ 0
    g
    0];
C=[ 1 0 0
    0 1 0
    0 0 1];
D=[ 0
    0
    0];
for index1=1:length(Mass)
    for index2=1:length(Rcirc)
        if isinf(Rcirc(index2))
            A=[ 0 1 0
                -ks/m(index1) -cf/m(index1) -1/m(index1)
                0 0 0];
        else
            A=[ 0 1 0
                -ks/m(index1) -cf/m(index1) -1/m(index1)
                0 Kte*Ktf/Lcoil -Rcirc(index2)/Lcoil];
        end
    System=ss(A,B,C,D);
```

```
    Y=step(System,T);
    keep=find(Y(:,1)<=24.5e-3);
    Crossing(index1,index2)=T(keep(end));
    MaxVelocity(index1,index2)=Y(keep(end),2);
    MaxForce(index1,index2)=Y(keep(end),3);
    subs=find(Y(:,1)>24.5e-3);
    SimX{index1,index2}=[Y(keep,1);24.5e-3*ones(size(subs))];
    SimV{index1,index2}=[Y(keep,2);zeros(size(subs))];
    SimF{index1,index2}=[Y(keep,3);zeros(size(subs))]…
           +cf*SimV{index1,index2};
end
end

function cf=DetermineC(Y,T,M)
% Function to estimate the parasitic damping coefficient using
% a linear regression on the straight part of the displacement data.
%
%% cf=DetermineC(Y,M)
%
% Y: displacement profiles in mm when Rload=open circuit
% T: time vector corresponding to displacement matrix
% M: corresponding mass values in kg
%
% (c) April 2005 Rogelio Palomera-Arias
dimension=size(Y);
for index=1:dimension(2)
    rawdata=Y(:,index)/1000;
    remove=find(rawdata>24.5e-3);
    cleandata=rawdata(1:remove(1));
    time=T(1:remove(1));
    remove=find(time<=0.05);
    cleandata=cleandata(remove(end):end);
    cleantime=time(remove(end):end);
    % linear regression fit
    X=[ones(size(cleantime)) cleantime];
    regression=X\cleandata;
    c(index)=M(index)*9.81/regression(2);
end
cf=min(c);
```

E.2.2 Data Manipulation Files and Methods

```
%%%%%%%%%%%%%%%%%%%%%%%%%%%%%%%%%%%%%%%%%%%%%%%%
%% Script to extract velocity from position data
%% then smooth the result using a lowess local
%% regression smoothing.
%%%%%%%%%%%%%%%%%%%%%%%%%%%%%%%%%%%%%%%%%%%%%%%%
for index1=1:4
    for index2=1:4
        % Creating Velocity Cell in m/s
```

```
        ExpV{index1,index2}=diff(ExpX{index1,index2})/.002/1000;
        % Smoothing Things Out
       ExpVS{index1,index2}=…
           SmoothingData(Time(2:end),ExpV{index1,index2});
    end
end


function Ys=SmoothingData(X,Y)
%Smoothing Data Y with respect to X using a
% 11 point  "lowess" local regression algorithm
N=length(X);
dimension=size(Y);
dim=find(N~=dimension);
if dim==1
    Y=Y';
end
for index=1:dimension(dim)
Ys(:,index) = smooth(X,Y(:,index),11,'lowess');
End

%%%%%%%%%%%%%%%%%%%%%%%%%%%%%%%%%%%%%%%%%%%%%%%%%%%%%%%%%%%%%%%%%%%%%%%
% Script to plot experimental and simulation results from
% damped drop mass experiment
%
% Data is in DropDataCells.mat file
%%%%%%%%%%%%%%%%%%%%%%%%%%%%%%%%%%%%%%%%%%%%%%%%%%%%%%%%%%%%%%%%%%%%%%%

% Selection Menus
sel=menu('Chose the provfile to plot','Position','Velocity');
sel2=menu('Chose type of
plot','Experimental','Simulation','Comparison');
% Define  plot type and text arrays
tit={'Position' 'Velocity'};            % Title Type
ylab={'Drop (mm)' 'Velocity (m/s)'};    % Y Axis Type
assign={'Exp=ExpX{indexm,indexr};Sim=1000*SimX{indexm,indexr};T=Time;'
'Exp=ExpVS{indexm,indexr};Sim=SimV{indexm,indexr};Sim=Sim(2:end);T=Tim
ev;'};
% Plotting Instruction based on sel2
exec={'plot(T,Exp,marker{index},''LineWidth'',2.5)'
'plot(T,Sim,marker{index},''LineWidth'',2.5)'
'plot(T,Sim,T,Exp,''.'')'};
% Parameters for plotting and legends
marker={'--' ' ' '-.' ':'};
Resis={'R_0=\infty' 'R_1=14.2\Omega' 'R_2=9.5\Omega' 'R_3=4.4\Omega'};
Mass={'m_0=272.5g' 'm_1=336.3g' 'm_2=400.1g' 'm_3=463.9g'};
% Releasing figures
for indexm=1:4
    figure(indexm)
    figure(indexm+4)
    hold off
    if sel2~=3
```

```
        subplot(111)
    end
end
% Plotting
for indexm=1:4
    figure(indexm)
    for indexr=1:4
        eval(assign{sel});
        switch sel2
            case 3 % Comparison plots
                subplot(220+indexr)
                eval(exec{sel2});
                xlabel('Time (s)')
                ylabel(sprintf('%s',ylab{sel}))
                title(sprintf('%s Profile for m_%d and
R_%d',tit{sel},indexm-1,indexr-1))
                legend('Simulated','Experimental')
            case {1,2}  % Result plots
                figure(indexm) % Constant Mass
                index=indexr;
                eval(exec{sel2});
                title(sprintf('%s Plots for
%s',tit{sel},Mass{indexm}))
                legend(Resis)
                hold on
                figure(indexr+4) % Constant Resistance
                index=indexm;
                eval(exec{sel2});
                title(sprintf('%s Plots for
%s',tit{sel},Resis{indexr}))
                legend(Mass)
                hold on
        end
        xlabel('Time (s)')
        ylabel(sprintf('%s',ylab{sel}))
    end
    orient landscape
end
```

E.2.3 Sample Experimental Position Graphs

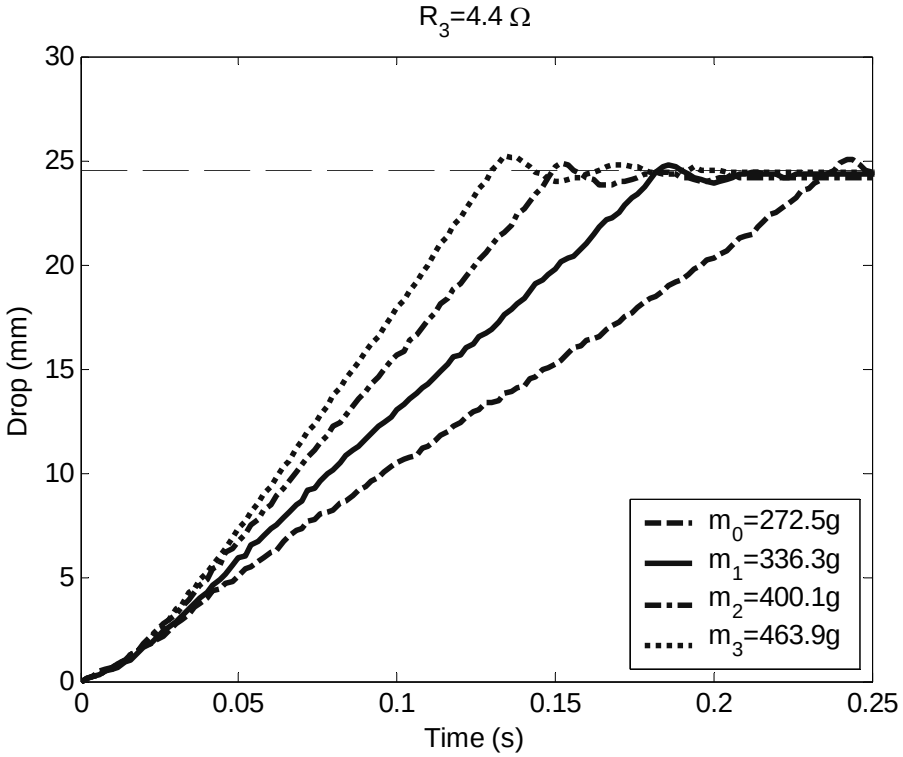

Figure E.1 Experimental Drop Profiles for Various Mover Masses (R=4.4 Ω).

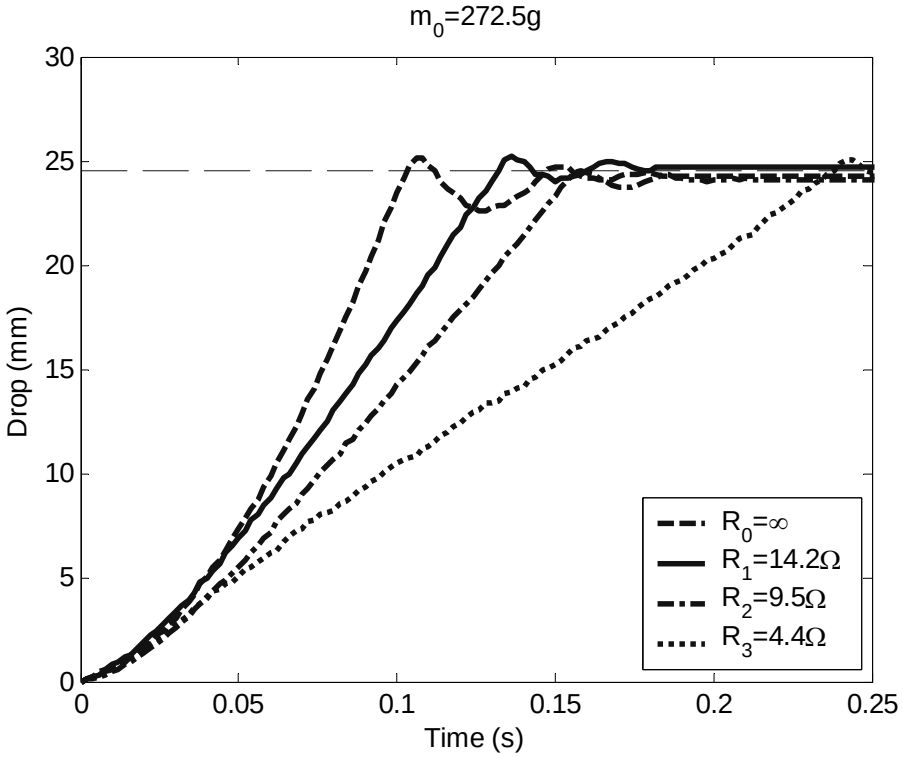

Figure E.2 Experimental Drop Profiles for Various Circuit Resistances (m=272.5g)

E.2.4 Sample Experimental Velocity Graphs

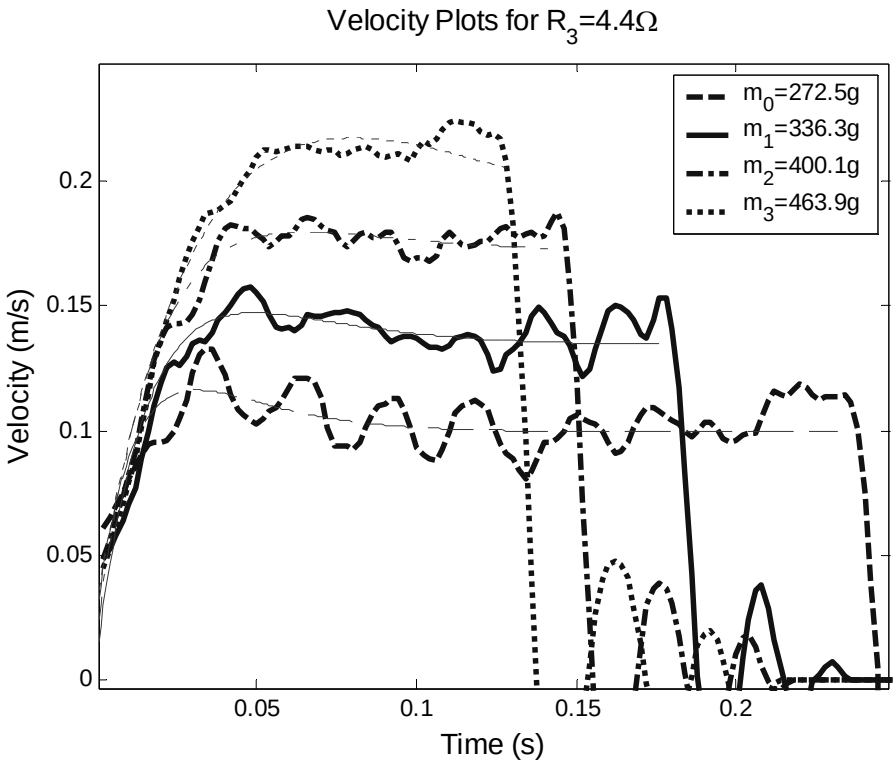

Figure E.3 Experimental Drop Velocity as a Function of Mass (R_{circ}=4.4Ω).

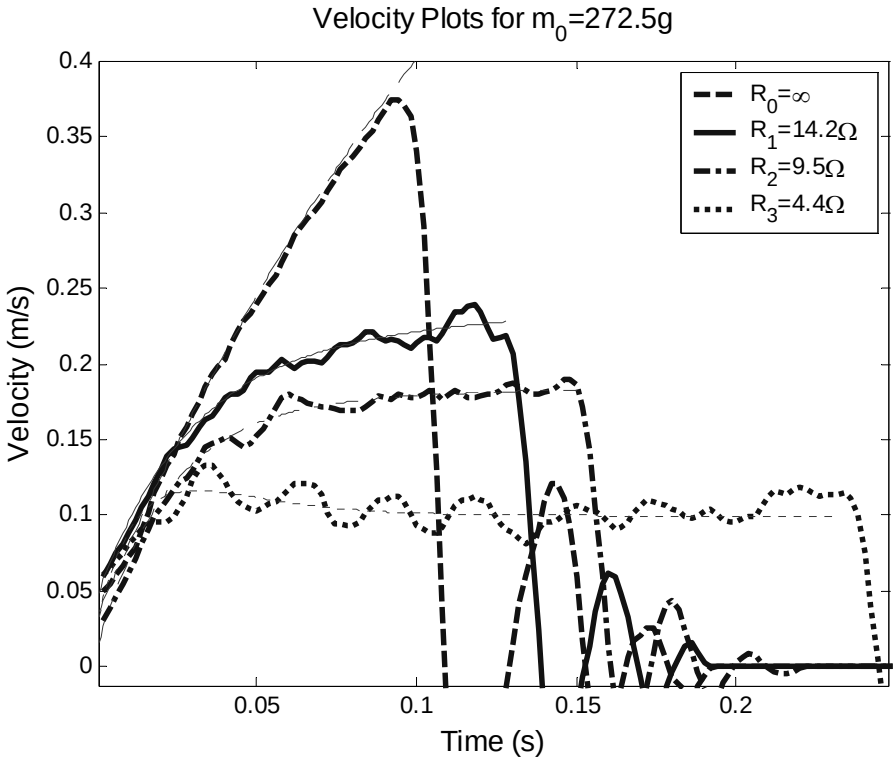

Figure E.4 Experimental Drop Velocity as a Function of Resistance (Mass=272.5g).

E.2.5 Sample Experimental Force Graphs

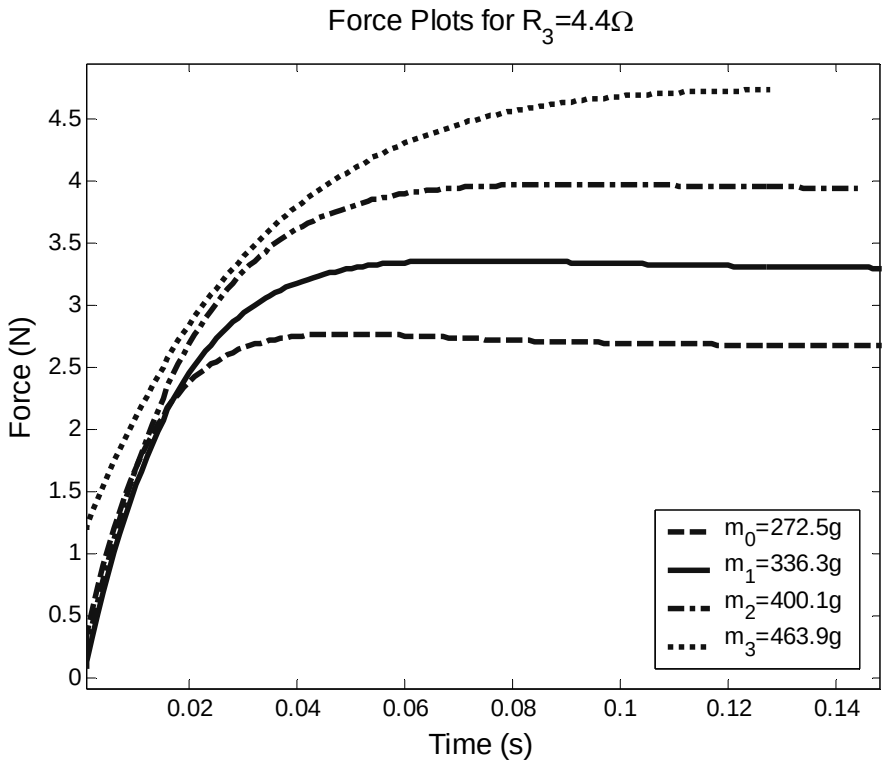

Figure E.5 Experimental Damper Force (fitted) as a Function of Mass (R_{circ}=4.4Ω).

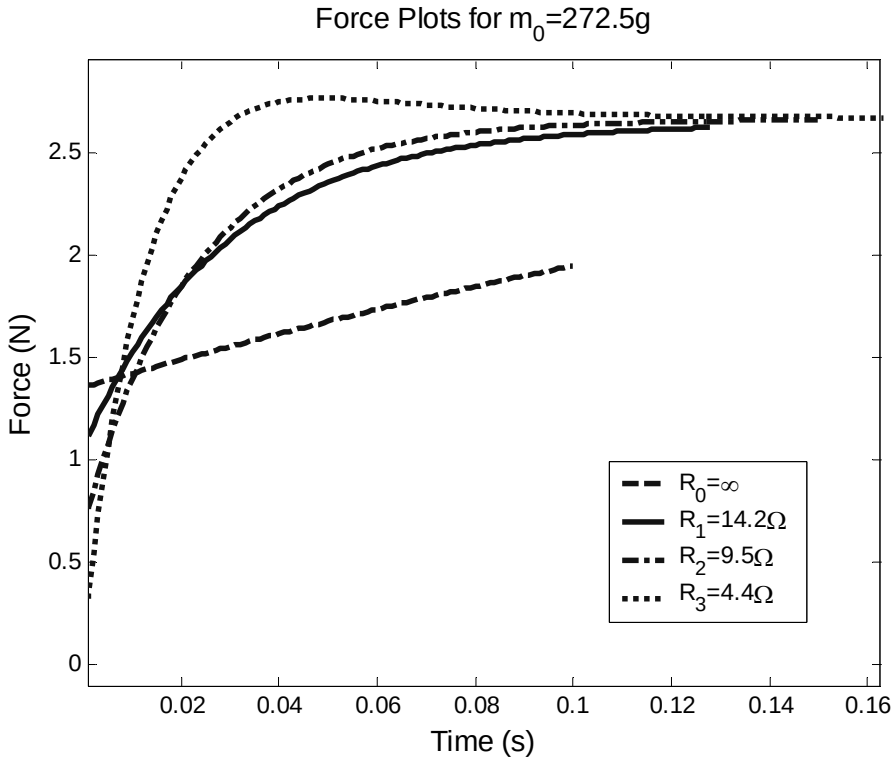

Figure E.6 Experimental Damper Force (fitted) as a Function of Resistance (Mass=272.5g).

E.3 Oscillatory Velocity Experiment

E.3.1 Simulation Program

```
function [F,X]=CyclicDamper(Rload,Omega,t)
% Function to simulate the damper reaction force given a displacement
% imparted through a rotational-linear linkage at constant angular ve-
locity
%
%   [F,X]=CyclicDamper(Rload,Omega,t)
%
%   F=[Fs Fd]
%   X=[x v a]
%
% (c) July 2005 Rogelio Palomera-Arias

%%% Linear Damper
Kte=7.874;      % Back EMF Constant   {Vs/m}
Ktf=7.918;      % Force Constant    {N/A}
Rcoil=3.89;     % Coil Resistance   {Ohms}
Lcoil=2.03e-3;  % Coil Inductance   {H}
Md=200e-3;      % Mover mass        {Kg}
Rcirc=Rload+Rcoil;
num=Kte*Ktf;
den=[Lcoil Rcirc];
damper=tf(num,den);
%%%% Linkage Parameters
r=12e-3;
l=50e-3;
Theta=Omega*t;
CosFact=sqrt(l^2-r^2*sin(Theta).^2);
x=CosFact-l+r*cos(Theta);
v=-r*sin(Theta).*(1+r*cos(Theta)./CosFact).*Omega;
a=-Omega*2*(r*cos(Theta)+r^2*(cos(Theta).^2-
sin(Theta).^2)./CosFact+r^4*cos(Theta).^2.*sin(Theta).^2./(CosFact).^3
);
%%%%% Damper Response
Fd=lsim(damper,v,t);
% If load resistance is open circuit, no damper force
if isinf(Rcirc)
    Fd=zeros(size(Fd));
end
% Sensor Force
Fs=Md*a+Fd;
F=[Fs Fd];
X=[x v a];
```

E.3.2 Data Manipulation Scripts

```
function [Time,Data,DataRaw]=ReadLabViewData(filename)
DataRaw=load(filename);
[N,Chs]=size(DataRaw);
fs=6000;    % Data sampling rate
% Cleaning data to remove 60Hz components
%for index=1:Chs
%DataClean(:,index)=smooth(DataRaw(:,index),101);
%end
n=10;
r=12e-3;
l=50e-3;
% Adjusting Position to zero
DataRaw(:,2)=DataRaw(:,2)-DataRaw(1,2);
DataClean=DataRaw;
Time=(0:1/fs:(N-1)/fs)';
% Moving Time to 0
plot(DataRaw(:,2));
axis([0 300 -.2 .2])
[pos,y]=ginput(1);
pos=ceil(pos);
% Cleaning Data but Position
for index=1:N-1
    if (index+n-1)>N
        DataClean(index,[1 Chs])=mean(DataRaw(index:N,[1 Chs]));
    else
        DataClean(index,[1 Chs])=mean(DataRaw(index+[0:n-1],[1 Chs]));
    end
end
% Defining conversions
%Va=1/.25;
%Ia=1/.5;
W=2000*pi/(3*60);   % Angular Velocity
P=1/.25;            % Angular Position
F=44.48/(2.054*5);
% Converting data
K=[-W 0 0
    0 P 0
    0 0 F ];
Data=DataClean*K;
DataRaw=DataRaw*K;
Time=Time(pos:end);
Time=Time-Time(1);
Theta=Data(pos:end,2);
Omega=Data(pos:end,1);
CosFact=sqrt(l^2-r^2*sin(Theta).^2);
x=-(CosFact-l+r*cos(Theta));
v=r*sin(Theta).*(1+r*cos(Theta)./CosFact).*Omega;
Data=[x v Data(pos:end,3)];
DataRaw=DataRaw(pos:end,:);
```